ANALYSIS OF THE PHYSICAL FACTORS INFLUENCING PORTAL IMAGING EXIT DOSIMETRY USING MONTE CARLO MODELING

by

Collins Yeboah

A Thesis

Submitted to the Faculty of Graduate Studies

in Partial Fulfillment of the Requirements

for the Degree of

MASTER OF SCIENCE

Department of Physics

University of Manitoba

Winnipeg, Manitoba

THE UNIVERSITY OF MANITOBA

FACULTY OF GRADUATE STUDIES

*****

COPYRIGHT PERMISSION PAGE

ANALYSIS OF THE PHYSICAL FACTORS INFLUENCING PORTAL IMAGING EXIT DOSIMETRY USING MONTE CARLO MODELING

BY

COLLINS YEBOAH

A Thesis/Practicum submitted to the Faculty of Graduate Studies of The University of Manitoba in partial fulfillment of the requirements of the degree of

MASTER OF SCIENCE

Abstract

As the use of electronic portal imaging devices (EPIDs) increases, the emphasis which was initially on geometric verification, is shifting to portal exit dosimetry. In this latter concept, a portal dose image obtained during treatment with an EPID is compared with that calculated during treatment planning. The success of this approach will ultimately depend on a proper understanding of the factors that influence the measurement and calculation of dose distributions in the detector plane. The main objective of this work was to identify and analyze such factors using Monte Carlo methods. Firstly, the spectral characteristics of exit photon beams were studied. It was found that the intensity, energy spectrum, mean and effective energies of the beams are significantly affected by variations in the patient/detector geometry. These changes in the spectral characteristics translated into changes in the exit dose to a metal-phosphor detector. Studies performed with different detectors showed that the exit dose is significantly affected by the design and atomic composition of the detector. Existing dose calculation algorithms will need to be improved if they are to be used to predict the exit dose measured by the high atomic number metal phosphor detector. Interestingly, the effects of an increasing air gap and an increasing field size, and vice versa, were found to be roughly complimentary. This suggests the use of equivalent field size techniques to account for intensity and spectral changes arising from air gap variations. Based on Monte Carlo modeling, an equivalent field size technique has been proposed and confirmed experimentally. An advantage of this approach is that it can be integrated with the existing dose calculation algorithms with only minor modifications.

Acknowledgments

I would like to take this opportunity to thank all those people whose support and assistance made it possible to complete this research project.

Firstly, I would like to thank my supervisor and mentor, Dr. Stephen Pistorius, for his patience and guidance. He always had the time to answer my questions and to provide assistance with any problem. I am indebted to him.

I would also like to thank the members of my examining committee, Drs. David Viggars and Samy El Sayed for reading my thesis and providing useful comments.

Many thanks to Ms. Mahta Mirzai and Dr. Satyapal Rathee for their help in the experimental aspect of my work. They were always willing to give assistance, no matter how busy they were.

I would also like to thank Randy Roels for his help on fixing my computer any time there was a problem.

Special thanks to all of the students in the Department of Medical Physics for creating a friendly and stimulating environment to work in.

I would like to acknowledge the financial support from the Manitoba Cancer Treatment and Research Foundation, and the Jacob's Fund Studentship. I would not have been able

to "survive" had it not been the continued financial support provided in the form of a studentship.

Finally, I would like to thank my parents for their encouragement and support.

Table of Contents

Chapter 4: (cont.)

Chapter 1

Rationale for verification of radiotherapy treatments

1.1 Introduction

The goal of radiotherapy is to deliver a sterilizing dose of radiation to the tumour while minimizing the damage to the surrounding normal tissues. To accomplish this goal necessitates a number of steps in the treatment process, each of which needs to be accurately and precisely executed. The first of these is the acquisition of diagnostic information on the tumour (i.e. tumour site and stage), needed to define the tumour and target volumes and for identification of the organs at risk. These data are obtained using a variety of techniques, including endoscopy, surgical exploration, conventional radiographic techniques, computed tomography, nuclear medicine, ultrasound, and magnetic resonance imaging.

Once the target volume has been delineated and localized and the organs at risk determined, the next step in the treatment process is treatment planning, during which the optimal treatment technique is determined. The quality, number, orientation and shape of radiation beams that will be used in the treatment are specified, and a specially designed computer program is used for calculating the expected dose distributions in the patient.

Following the selection of a particular treatment plan, a pre-treatment simulation may be performed. The conventional simulation is performed by setting up the patient on a

simulator machine under conditions that closely resemble the actual treatment. The simulator is equipped with an x-ray tube, which is used for taking x-ray radiographs (simulation films). These radiographs show the prescribed size of the radiation field as well as the projection of the patient's anatomy along the direction of the prescribed beam, and are used for verifying patient set-up during treatment. Alternatively, patient positioning can be verified using digitally reconstructed radiographs (DRRs), which are generated from within the treatment planning system using available 3-dimensional computed tomography data.

The final step in this process is patient treatment, where the prescribed dose of radiation is delivered to the patient in a number of fractions that span a period of several weeks. Each fraction may consist of a few separate irradiations that correspond to different beam orientations and/or different shapes and quality of radiation fields. Preceding each dose delivery process, the patient is set-up to the position that was previously prescribed in the treatment plan or simulated.

1.2 Dependence of biological effects of radiation on dose

The radiation response of tumours and normal tissues as a function of the absorbed dose and its fractionation can generally be represented by sigmoidal curves whose slopes and relative position may differ for different tumours and normal tissues. The dose-response relationships depend on the volume of tissues, their biological characteristics such as oxygenation and proliferation rate, as well as the physical parameters (e.g. absorbed dose

distribution) that may influence the radiation effect.[1] For malignant tissues, the end point is tumour ablation or, in some cases, a reduction in tumour size. For normal tissues, a certain degree of side effects or complications can be expected at a given dose level. These complications may be categorized according to onset and type and percentage incidence.

The most important aspects of the dose-response curves for tumour control and normal tissue complications are the steepness, the relative steepness, and the separation of the two curves in dose. The steepness of the curves generally determines the accuracy required in the delivery of the prescribed dose, and indicates by how much the variation in the delivered dose will affect the tumour control and/or complication probability. The relative steepness of the curves is a measure of the increase (or decrease) in benefit that may result from a change in the absorbed dose level, while the separation of the two curves gives the level of success in tumour control for an acceptable incidence of normal tissue complications.[2] In other words, the greater the separation of the curves, the higher the chances of obtaining local tumour control with lower incidence of injuries to the normal tissues.

For small tumours the most important quantity of the dose response curve with regard to precision requirements on dose delivery is the normalized dose response gradient γ defined by:

$$\gamma = D \cdot dP/dD$$

where D represents dose and P is the tumour control probability. This parameter is dimensionless and describes how large a change in tumour control probability is to be expected for a given relative increase in absorbed dose. The above expression shows that a dose increase of 1 per cent will result in an increase in tumour control probability of precisely γ per cent. Although γ varies with the exact location on the dose response curve, it is fairly close to its maximum value γ_m for tumour control probabilities in the range 20 to 70 per cent.[3] At very low and high control rates γ decreases rapidly and it will be a less important quantity with regard to dosimetric requirements.

For large tumours and at high control rates normal tissue complications will be the most important quantity governing the precision required in dose delivery. This is due to the fact that the tumour control curve for large tumours moves to higher doses than the curve for small tumours. In contrast, the complication curve for normal tissues moves to lower doses because more normal tissues will generally be irradiated when the tumour is large. The probability of achieving complication-free tumour control will therefore decrease considerably as the size of the tumour increases.

Dose-response curves observed clinically and their characteristics have led to the recommendation that the tolerance level on accuracy in dose delivery be 3 per cent relative standard deviation in the delivered patient dose.[4] However, the value chosen at a given centre may depend on the type of cancers typically treated and to some extent also by the equipment and treatment techniques employed. The action level, at which it is essential to improve the accuracy in dose delivery is 5 per cent relative standard deviation.[4]

1.3 Uncertainties in normal clinical practice

The types of uncertainties usually considered are random and systematic uncertainties, both of which can be associated with a given parameter. Random uncertainties are determined from repeated measurements or repeated adjustments of a given parameter under the same conditions, whereas systematic uncertainties are introduced by a poor measurement process, a poor initial adjustment, the deviation with time of a parameter or an incorrect procedure. While random uncertainty is a measure of the precision (or the reproducibility) of a given parameter, systematic uncertainty refers to the accuracy of a parameter (i.e. its deviation from the true value).

It is clear from numerous reports that each and every step in the treatment process including the treatment prescription, preparation, calculation and delivery is subject to a certain degree of uncertainty.[4,6-8] Specifically, there are uncertainties associated with the target volume determination, the set up of the treatment unit parameters, the determination of the absorbed dose at a reference point in a patient, calibration of primary and secondary standards, the measurement of the dose distribution in the patient, the acquisition of patient data, the treatment planning, and the set-up of the patient. The related uncertainty in each section may affect either the absorbed dose delivered to the patient or the internal dose distribution, or possibly both.

A number of studies have shown that errors occur frequently in normal clinical practice. Svensson[9] analyzed the errors in the delivered dose to a specified point in an irradiated

patient. It was shown that, by following the procedure generally used in practice, the uncertainty in the dose distribution determination would be about 4.5%, that in the dose planning procedure about 4.4%, while the uncertainty in the patient irradiation (i.e. set-up of patient and beam/machine parameters) would be about 4%. These led to an overall uncertainty of about 8% in the delivered dose. The results of dose intercomparisons performed on various centres showed that much larger errors actually occur in clinical practice. A similar study, conducted by Mijnheer et al,[4] reported on the uncertainties in the various steps involved in the delivery of the prescribed dose at the specification point in a patient irradiated with two parallel opposed beams of megavoltage x-rays. For each step in the dose delivery process, they estimated both the associated random and systematic uncertainties, and found an overall uncertainty of 4.2% in the delivered dose. The discrepancy between the two studies arises because Mijnheer et al[4] ignored part of the systematic uncertainties (e.g. in the calibration of the ionization chamber), and also did not consider mistakes in the delivery of the prescribed dose to the patient resulting from errors in patient positioning, the set-up of the radiation machine, and the like.

Leunens et al[10] investigated the frequency and the sources of data transfer errors for 464 patients over a period of nine months. Erroneous data transfer was detected in 26% (119/464) of the treatments. A significant number (twenty-five) of these transfer errors led to deviations in dose that exceeded the recommended value of plus or minus 5%. It was also observed that there was no improvement in the error rate with time even though the results were regularly discussed. At first sight, it may appear as though this study disagrees with the work of Calandrino et al,[11] who reported on human error rate in the

calculation of monitor units in normal clinical practice. Out of the 890 checks made over a period of 10 months, Calandrino et al[11] found an overall human daily error rate of 3.7% (33/890), as opposed to 26% in the other study. In addition, Calandrino et al[11] reported that the serious human daily error rate, that lead to deviations of 5% or greater in the delivered dose, was 1.9% (17/890), while Leunens et al[10] found a value of 5.4% (25/464). An explanation for these disagreements lies in the number of different types of transcription errors considered by each study. While Leunens et al[10] included different types of data transfer errors in their analysis, Calandrino et al[11] considered only human errors in monitor unit calculations. As a result, higher error rates are reported in the former than in the latter study. In addition to the human errors discussed in the preceding text, Calandrino et al[11] found that the rate of errors that resulted in dose variations greater than 10% was 0.8% (7/890), with a maximum deviation of 15%. The authors in question also investigated the global dose error rate (i.e. the errors induced on the total reference dose for the complete course of the treatment) for 685 checks over 8 months and found a rate for serious errors of 1.3% (9/685).

Finally, Noel et al[12] reported on the errors detected in the dose delivery process for 7519 patients over a period of five years. Overall, seventy-nine errors were detected out of which seventy-eight (i.e. error rate of 1%) were of human origin. Half of these errors, corresponding to an error rate of 0.5%, could have caused a variation of over 10% in the delivered target dose. The reasons for the differences between this study and those[10,11] discussed previously is unclear.

1.4 Influence of uncertainties on outcome of treatment

A number of studies[1] have shown that, for a variety of tumours, a change in local control probability of between 0.4 and 9.3 per cent could result from an alteration in dose of only 1 per cent. For many normal tissues and organs a variation of 1 per cent in the delivered dose could lead to a change of between 0.6 and 7 per cent in the complication probability. Thus, complete tumour control cannot generally be achieved without severe complications unless the dosimetric uncertainties are very small. Boyer and Schultheiss[13] showed, in their theoretical study, that the gain in tumour control probability could be 2% per 1% improvement of accuracy in dose. Peters and Fletcher[14] analyzed the potential causes of failure in radiation therapy treatments in head and neck and found that localization errors and inadvertent underdosage are some of the major causes of radiotherapy failure.

1.5 The need for treatment verification

It has been shown in the preceding discussion that treatment errors, which lead to large dosimetric uncertainties, occur daily in clinical practice and that these affect the outcome of treatments. In order to ensure that the precisely planned treatment is delivered to the patient, treatment verification needs to be carried out to detect, quantify and correct these errors during the course of treatment. In addition, a number of technical advances have emerged in recent years and are being evaluated and/or introduced in many departments. One of such developments is dynamic conformal radiation therapy, in which radiation field direction, size and shape, and patient position might be dynamically controlled during

treatment in order to achieve a tightly conforming high dose region around the target volume. With the stringent requirements of higher doses to a smaller and more precisely defined target volume, a pressing need arises for effective means of verification of dose delivery.

1.6 Thesis Overview

Electronic portal imaging devices (EPIDs) are currently used in many departments for verifying the accuracy of patient set-up. In addition to this, EPIDs have the potential for use in dosimetric verification.[15-29] In principle, it is possible to use an EPID to measure the exit dose distributions in the detector plane and to compare these measured data with portal dose images calculated during treatment planning. The success of this approach will ultimately depend on a proper understanding of the factors that influence the measurement and calculation of dose distributions in the detector plane. The present study focuses on the identification and analysis of such factors using Monte Carlo Methods.[30]

In chapter 2 of this thesis a review of the current treatment verification techniques is presented. Firstly, the computerized "Record and Verify Systems" used for confirmation of the treatment unit parameters are discussed. A general description of such systems as well as their advantages and disadvantages are presented. Following this, geometric treatment verification with portal films as well as with electronic portal imaging devices is discussed. Finally, the existing dosimetric verification techniques are described. This

includes methods that use the conventional dosimeters (e.g. diodes, TLD, and ionization chambers) as well as the progress made so far in the emerging methodology of portal exit dosimetry.

In chapter 3 an analysis of the spectral characteristics of exit photon beams reaching the plane of the portal imaging detector is carried out. Monte Carlo methods are used to generate the energy spectrum at the entrance to and at the metal/phosphor interface of the detector. In addition, the mean and effective energies of photon beams are calculated as a function of patient/detector geometry and incident beam quality. To understand the influence of the detector, mean/effective energies calculated at the detector surface entrance are compared with those computed at the metal/phosphor interface of detector.

In chapter 4, we investigate how the spectral changes, reported in the preceding chapter, affect the dose to the metal/phosphor detector. Exit dose, calculated using the EGS4 Monte Carlo code system,[30] is scored as a function of patient/detector geometry and incident beam quality. Next, the effect of the high atomic number metal/phosphor detector on exit dose is investigated by comparing doses deposited in phosphor-based detectors with doses to water-based detectors. These made it possible to quantify those factors which affect exit dose including, among other things, the large and variable air gap between the exit surface of patient and detector.

In chapter 5, an equivalent field size concept to model the air gap is introduced. A patient/detector geometry that includes an air gap is referred to as the clinical geometry,

while the corresponding geometry without an air gap (i.e. detector in contact with patient) is designated the reference geometry. An empirical model, which relates the actual field size in a clinical geometry to an equivalent field size in the corresponding reference geometry, is developed and evaluated using Monte Carlo modeling. To validate the Monte Carlo generated model, experimental measurements are presented and discussed.

Finally, a summary of the results is presented in chapter 6, where the relevant conclusions are drawn. We discuss the further work required, disagreement with existing literature, errors, and applications of the concepts developed in this research.

References

1. A. Brahme, "Accuracy requirements and quality assurance of external beam therapy with photons and electrons," Acta Oncol., Suppl. 1 (1988).

2. J. V. Moore et al, "Dose-incidence curves for tumour control and normal tissue injury, in relation to the response of clonogenic cells," Radiother. Oncol. 1, 143-157 (1983).

3. A. Brahme, "Dosimetric precision requirements in radiation therapy," Acta Radiol. Oncology 23, 379 (1984).

4. B. J. Mijnheer, J. J. Battermann and A. Wambersie, "What degree of accuracy is required and can be achieved in photon and neutron therapy?," Radiother. Oncol. 8, 237-252 (1987).

5. International Commission on Radiation units and measurements, "Determination of absorbed dose in a patient irradiated by beams of X- or gamma rays in radiotherapy procedures," I.C.R.U. Report No. 24, ICRU, Bethesda, Maryland, U.S.A. (1976).

6. S. Blanco, M. A. Lopez-Bote and M. Desco, "Quality assurance in radiation therapy: Systematic evaluation of errors during treatment execution," Radiother. Oncol. 8, 256-261 (1987).

7. A. Dutreix, "When and how can we improve precision in radiotherapy?," Radiother. Oncol. 2, 275-292 (1984).

8. G. Leunens, J. Verstraete, A. Dutreix, and E. van der Schueren, "Assessment of dose inhomogeneities at target level by in vivo dosimetry: can the recommended 5% accuracy in the dose delivered to the target volume be fulfilled in daily practice?," Radiother. Oncol. **25**, 242-250 (1992).

9. H. Svensson, "Quality assurance in radiotherapy: Physical aspects," Int. J. Rad. Oncol. Biol. Phys. **10**, Suppl 1, 59-65 (1984).

10. G. Leunens, J. Verstraete, A. Dutreix, and E. van der Schueren, "Human errors in data transfer during the preparation and delivery of radiation treatment affecting the final result: "garbage in, garbage out"," Radiother. Oncol. **23**, 217-222 (1992).

11. R. Calandrino, G. M. Cattaneo, A. D. Vecchio, and P. Signorotto, "Human errors in the calculation of monitor units in clinical radiotherapy practice," Radiother. Oncol. **28**, 86-88 (1993).

12. A. Noel, P. Aletti, P. Bey, and L. Malissard, "Detection of errors in individual patients in radiotherapy by in vivo dosimetry," Radiother. Oncol. **34**, 144-151 (1995).

13. A. L. Boyer and T. Schultheiss, "Effects of dosimetric and clinical uncertainty on complication-free local tumour control," Radiother. Oncol. **11**, 65-71 (1988).

14. L. J. Peters and G. H. Fletcher, "Causes of failure of radiotherapy in head and neck cancer," Radiother. Oncol. **1**, 53-63 (1983).

15. J. Leong, "Use of digital fluoroscopy as an on-line verification device in radiation therapy," Phys. Med. Biol. **31**, 985-992 (1986).

16. J. W. Wong, J. W. Slessinger et al, "Portal Dose Images I: Quantitative Treatment Plan Verification," Int. J. Rad. Oncol. Biol. Phys. **18**, 1455-1463 (1989).

17. X. Ying, L. Y. Geer and J. W. Wong, "Portal Dose Images II: Patient Dose Estimation," Int. J. Rad. Oncol. Biol. Phys. **18**, 1465-1475 (1990).

18. B. J. M. Heijmen, J. S. Stroom, H. Huizenga, and A. G. Visser, "In vivo dose measurements using an electronic portal imaging device: A feasibility study," Radiother. Oncol. **24** Suppl., S25 (1992).

19. B. J. M. Heijmen, J. S. Stroom, H. Huizenga, and A. G. Visser, "Application of a fluoroscopic portal imaging system with a CCD camera for accurate in vivo dosimetry (Abs.)," Med. Phys. **20**, 870 (1993).

20. M. C. Kirby, and P. C. Williams, "The use an electronic portal imaging device for exit dosimetry and quality control measurements (abs)," Int. J. Rad. Oncol. Biol. Phys. **27**, Suppl. 1, 165 (1993).

21. M. C. Kirby, and P. C. Williams, "Measurement possibilities using an electronic portal imaging device," Radiother. Oncol. **29**, 237-243 (1993).

22. V. N. Hansen, P. M. Evans, and W. Swindell, "Transit dosimetry: Computer generated dose images for verification," *in Proceedings of the Xith ICCR (International Congress on the use of Computers in Radiation Therapy)*, edited by A. R. Hounsell, J. M. Wilkinson, and P. C. Williams (Christie Hospital NHS Trust, Manchester, 1993), pp. 166-117.

23. S. Pistorius and C. Yeboah, "Analysis and modeling of electronic portal imaging exit dose measurements," Radiother. Oncol. **37** (Suppl. 1), S21 (1995).

24. C. Yeboah and S. Pistorius, "Investigation of the factors that affect the use of an electronic portal imaging device for quantitative dosimetry (abs)," Med. Phys **23**, 811 (1996).

25. R. Rajapakshe, Optimization of a real-time portal imaging system for quantitative imaging, Ph.D. Thesis, University of Manitoba, Winnipeg, Canada (1995).

26. P. Stucchi, L. Conte, C. Mordacchini et al., "The use of an electronic portal imaging device for exit dosimetry," Radiother. Oncol. **37** (Suppl. 1), S21 (1995).

27. W. Swindell and P. M. Evans, "Scattered radiation in portal images: A Monte Carlo simulation and a simple physical model," Med. Phys. **23,** 1-11 (1996).

28. T. R. McNutt, T. R. Mackie, P. Reckwerdt, N. Papanikolaou, and B. R. Paliwal, "Calculation of portal dose using the convolution/superposition method," Med. Phys. **23,** 527-535 (1996).

29. T. R. McNutt, T. R. Mackie, P. Reckwerdt, and B. R. Paliwal, "Modeling dose distributions from portal dose images using the convolution/superposition method," Med. Phys. 23, 1381-1392 (1996).

30. W. R. Nelson, H. Hirayama and D. W. O. Rogers, "The EGS4 Code System," Stanford Linear Accelerator Centre, Report SLAC-265 UC-32, National technical Information Services, U.S. Dept. of Commerce, 5285 Port Royal Road, Springfield, Virg-22161 (1985).

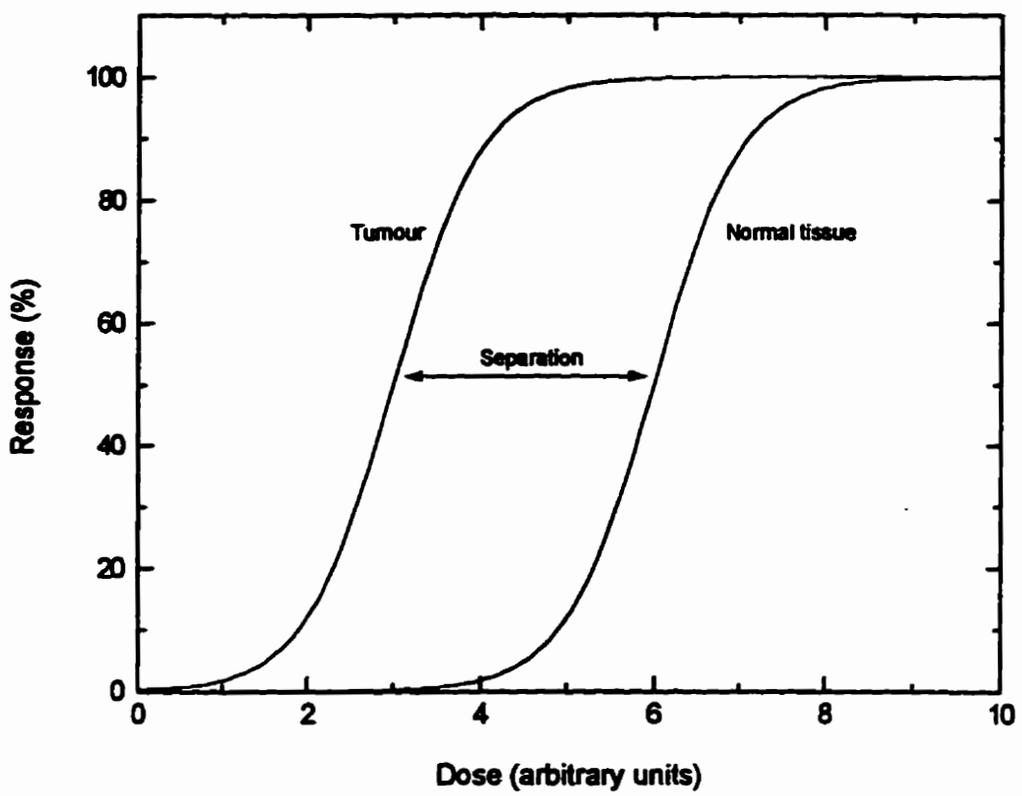

Figure 1-1. Idealized dose-response curves for tumour control and normal tissue complication.

Chapter 2

Methods of Treatment Verification

2.1 Introduction

Treatment verification ensures the accuracy of radiation treatments. It is a major component of the overall quality assurance program and is designed to detect various mistakes, errors, and inaccuracies that can occur during an entire course of treatment. Geometric verification is performed to verify that patient set-up errors are within acceptable tolerances. In this methodology, a transmission image of the patient is acquired just before or during treatment using portal films or on-line portal imaging techniques, and is compared with images taken during treatment simulation. To verify the dosimetric accuracy, the conventional approach is to carry out in vivo dosimetry using diodes, TLD, or ionization chambers. In recent years, however, the focus is shifting to the emerging methodology of portal exit dosimetry, which may provide a faster means of verifying delivered dose distributions.

2.2 Record and verify systems

Treatment errors can arise from incorrect settings of therapy machine parameters, such as the beam energy, gantry angle, collimator angle, radiation field size, couch height and wedge number. In order to be able to detect and correct these errors, many therapy machines are equipped with computerized systems for recording and verifying the field

parameters before each treatment. Such a Record and Verify System[1-3] inhibits the radiation beam if the settings of the treatment machine do not agree with prescribed values within given tolerances. These systems have been shown to dramatically reduce major errors, particularly those involving the presence or orientation of wedges and incorrect dose settings.[1] Podmaniczky et al.[2] reported that the Record and Verify System had detected and prevented significant errors that otherwise would have occurred in about 1 per cent of all fields treated. The Record and Verify Systems, however, cannot check the presence or location of unmounted shielding blocks, or in most cases the position of the treatment couch, or patient set-up Consequently, such systems cannot be viewed as a comprehensive solution of the treatment verification problem.

2.3 Geometric treatment verification

In order to ensure the correctness of the treatment geometries the field size, shape, orientation, patient set-up, and coincidence of treatment and target volumes are verified during patient irradiation. Portal films have been used extensively to accomplish this. Periodically, a film is placed on the beam exit side of the patient and records a two-dimensional projection of the patient's anatomy that lie within the radiation field. This portal film is then compared with those made during treatment planning. Different types of films can be used: A localization film is acquired with a brief exposure of a few monitor units and is then processed and examined before the remainder of the treatment is delivered. A verification film is less sensitive and is exposed over the entire treatment, causing minimal interference with the clinical work. However, errors can only be

corrected on the following treatment, and image quality may be reduced if there is significant patient movement. A portal image can also be obtained with a double-exposure film, in which a short exposure of large unblocked field is followed by a second exposure to the actual treatment field. The advantage of this is that it shows the anatomical features outside the field boundaries, which is often very useful in identifying patient positioning. Frequent use is however limited by the radiation tolerance of the exposed normal tissues. In spite of their usefulness, portal verification films have some deficiencies. Firstly, they require a relatively long time to develop and analyze, and image quality is often poor with poor anatomical details. This verification process is expensive in human and material resources, and it is therefore only feasible to take a limited number of films per week for each patient.

These problems have been addressed in recent years with the introduction of electronic portal imaging devices (EPIDs) in clinical radiotherapy.[4] Although different types of EPIDs are available, video-based electronic portal imaging devices (VEPIDs) are common. VEPIDs basically consist of a metal/phosphor detector, a 45° front surface mirror, a video camera connected to an image processing system, and a monitor which is used for displaying a processed image (see figure 2-1). During patient treatment the x-rays that exit the patient are incident on the metal/phosphor detector, and these are converted by the phosphor screen into light output which is viewed by the video camera through the 45° front surface mirror. The acquired signal is then processed and serves as a near-real time portal image of the patient's anatomy which can be used to verify the reproducibility of patient positioning throughout an entire treatment.[5-12] These verification

techniques, while giving assurance about the geometric correctness of the treatment, do not provide any quantitative information about the accuracy in the delivered dose.

2.4 Dosimetric verification techniques

Dosimetric accuracy verification is concerned with the comparison of measured and intended target doses during patient irradiation to ensure that the accuracy in the dose being delivered to the target volume is within the recommended tolerance limit of ±5%. The most direct way to do this accuracy check is to place a dosimeter in the target volume during treatment. However this is very difficult, if not impossible, to do for many tumour sites. Many centres have therefore resorted to the technique of measuring entrance and/or exit doses during patient irradiation and comparing these measurements with the expected doses. Films, semiconductor (diode) detectors, thermoluminiscent dosimeters (TLD) and ionization chambers have been used for this purpose.[13–22] Although these verification techniques provide some confidence in the correct implementation of a patient's treatment plan, most of the strategies limit the dosimetry to the beam axis while others select a few points in the treatment field. The information obtainable from selected point comparisons is however inadequate in identifying the causes of discrepancies that occur between the delivered and the prescribed doses.[23]

It is generally accepted that the grey (intensity) value distribution in an electronic portal image is related to the absorbed dose distribution in the fluorescent screen.[24-31] Thus, in addition to their primary use for positional verification, EPIDs have the potential for

quantitative dosimetry. The feasibility studies that evaluated the possibility of using EPIDs for real-time dosimetric verification purposes were pioneered by Leong,[32] who investigated the dosimetric characteristics of a portal imaging system. It was found that the portal imaging detector can be configured to act as a large collection of dosemeters, which is capable of providing detailed information, in near real-time, about the exit dose distribution throughout an entire treatment. The comparison of measured exit dose distributions in the detector plane with dose distributions predicted by calculation has been shown to be feasible,[23,33] and may therefore be used as an approach for verifying the dosimetric accuracy of a radiotherapy treatment.

In seeking a relationship between the grey value and the exit dose distributions for an electronic portal imaging device (the Philips SRI-100), Heijmen et al[25] found that the grey value distribution in a portal image can be predicted by convolving the dose distribution in the phosphor screen with a point spread function that they referred to as the "fluorescence kernel". This kernel is the grey value distribution in an image that results from a pencil beam incidence on the portal imaging detector in an open beam geometry. While, according to these authors, the grey value in a particular image pixel is not directly related to the dose at the corresponding point of the phosphor screen, the work of Rajapakshe,[26] on the other hand, shows a direct relationship between the grey values and the corresponding exit doses. The fact that different imaging systems were used in the two studies suggests that the relationship between the grey values and the phosphor screen dose might not be unique but is probably a function of the characteristics of the particular imaging system employed. In Rajapakshe's work,[26] exit doses measured with an ion

chamber in the detector plane were related to grey value distributions in portal images obtained with a CCD camera-based electronic portal imaging system. For an unwedged beam, it was found that the grey values were linearly related to the measured exit doses to within 5% while for a wedged beam the deviations from linearity were up to about 15%. When the detector response was taken into account, however, there was excellent agreement between the grey value distributions and the measured exit doses. In addition, the linearity of the CCD camera in detecting optical photons emitted from the phosphor screen was investigated. The detection process was found to be linear within 3% error and this makes the CCD camera a good candidate for real-time dosimetry.

The progress made so far in the application of electronic portal imaging devices for exit dose measurements is encouraging but more work remains to be done.[23,34] A difficult problem is the estimation of the dose distribution in a patient using the exit dose measurements made with an EPID. An iterative approach for estimating this dose has been proposed by Ying et al.[34] In this technique, the dose distribution in the detector plane (i.e. the portal dose image) is calculated from the 3-dimensional CT data obtained during treatment planning and is compared with the measured portal dose image. The differences are then used to modify the original CT data, and the resulting data is, in turn, used to calculate a new dose image. This procedure is repeated until there is an acceptable agreement between the calculated and measured portal dose images. Finally, the patient dose is estimated using the modified CT data obtained at the end of the iterative process. Although the results of their analysis are promising and show that it may be possible to use measured portal dose images for determining the internal doses of

patients, the iterative technique used is time consuming, requiring about five hours to calculate a single dose image. It is therefore not suitable for real time imagery.

In an alternative method[33,35,36] for estimating the dose distribution in a patient, the scatter fluence (or signal) reaching the detector plane is first determined by calculation. It is then subtracted from the total fluence that is measured with the portal imaging device to obtain the primary fluence. This primary fluence is backprojected through the patient, and finally a convolution of the resulting primary fluence with energy-deposition kernels[37-40] is carried out to estimate the primary dose distribution in the patient. This approach to patient dose estimation led Swindell and Evans[35] to propose a semi-analytic model of the scatter-to-primary signal ratio as seen by a portal imaging system, based on Monte Carlo generated data. This model provides some understanding of the magnitude of the scatter signal relative to the primary signal in a portal imaging detector. It is however applicable only to large exit surface-to-detector distances, and employs idealized detectors (namely, the photon-counting, the photopeak, and the Compton detectors) which are usually not used in practice.

The whole idea of employing EPIDs for quantitative dosimetric verification purposes requires accurate dose calculation techniques for calculating the exit dose distribution in the detector plane. Existing algorithms for calculating photon dose distributions including the convolution techniques, have however been shown to be in error for exit beam dosimetry.[41,42] Woo[41] has analyzed the dose fall-off at the exit surface of a water phantom and has shown that the convolution/superposition method overestimates the exit dose.

This occurs because this dose calculation technique neglects the decrease in multiple backscatter due to the exit surface. In a clinical setting, an air gap thickness of 30 to 40 cm is usually present between the exit surface of a patient and the portal imaging detector. This air gap is considered as an inhomogeneity and the standard techniques for calculating dose in heterogeneous media are assumed to be applicable. One of these inhomogeneity correction techniques is the density scaling method which scales the thickness of the inhomogeneity in proportion to the relative electron density of the inhomogeneity with respect to water. This is the standard technique employed by the convolution/superposition dose calculation method to correct for tissue inhomogeneities,[33,42] and use has been made of the technique by McNutt et al[33] to predict portal dose images in a liquid-filled ionization chamber matrix portal imaging device. However, unlike the liquid-filled ionization chamber matrix, the metal/phosphor detectors have high atomic numbers and are not water equivalent. As a result, the application of the energy deposition kernels, generated in water, in calculating portal doses in these metal/phosphor detectors may be inappropriate.

The validity of the density scaling method employed by the convolution technique for photon and electron beam dose calculations in conditions of large air gaps between homogeneous water slabs has been investigated by Woo and Cunningham.[42] The convolution/superposition method (in conjunction with the density scaling approach) was used to calculate the absorbed dose at varying depths in water below an air gap. Large discrepancies were seen between the density scaling calculations and data obtained with the Monte Carlo method. It was shown that, in general, density scaling is most inaccurate

for the region immediately below an air gap, with the error increasing with larger air gaps and smaller field sizes. The density scaling technique employed by the convolution/superposition methodology may therefore lead to inaccurate dose calculations in metal/phosphor portal imaging detectors,[43] which are generally fairly thin and respond non-linearly to photons,[44] particularly in the energy range below 5-MeV. In order to be able to successfully develop a model to accurately calculate exit doses in metal/phosphor detectors, it is essential that we obtain a sound understanding of the factors that influence this dose. Detailed studies of x-ray scatter in megavoltage imaging conducted by Jaffray et al[44] and the analysis of exit doses by Swindell and Evans[35] have shown that the Monte Carlo method[45] can be used successfully to analyze those factors affecting exit doses.

References

1. R. Muller-Runkel and S. Watkins, "Introducing a computerized record and verify system: Its impact on treatment errors," Med. Dosim. **16**, 19-22 (1991).

2. K. C. Podmaniczky, R. Mohan et al, "Clinical experience with a computerized record and verify system," Int. J. Rad. Oncol. Biol. Phys. **11**, 1529-1537 (1985).

3. R. W. Miller and J. van de Geijn, "The use of a bar code scanner to improve the utility and flexibility of record and verify systems used in radiation therapy," Med. Phys. **15**, 611-613 (1988).

4. A. L. Boyer, L. Antonuk, A. Fenster and M. V. Herk et al, "A review of electronic portal imaging devices," Med. Phys. **19**, 1-16 (1992).

5. D. J. Gladstone, M. van Herk and L. M. chin, "Verification of lung attenuator positioning using an electronic portal imaging device," Int. J. Rad. Oncol. Biol. Phys. **27**, 449-454 (1993).

6. M. C. Kirby, and P. C. Williams, "Portal imaging for the verification of breast treatments," Radiother. Oncol. **22**, 314-316 (1991).

7. A. Ezz, P. Munro, A. T. Porter, J. Battista, D. A. Jaffray, A. Fenster and S. Osborne, "Daily Monitoring and correction of radiation field placement using a video-based

portal imaging system: a pilot study," Int. J. Rad. Oncol. Biol. Phys. **22**, 159-165 (1991).

8. W. De Neve, F. Van Den Heuvel, M. Coghe, D. Verellen et al, "Interactive use of an on-line portal imaging in pelvic radiation," Int. J. Rad. Oncol. Biol. Phys. **25**, 517-524 (1993).

9. C. L. Creutzberg, V. G. M. Althof, H. Huzenga, A. G. Visser, and P. C. Levendag, "Quality assurance using portal imaging: the accuracy of patient positioning in irradiation of breast cancer," Int. J. Rad. Oncol. Biol. Phys. **25**, 529-539 (1993).

10. G. van Tienhoven, J. H. Lanson, D. Crabeels, S. Heukelom and B. J. Mijnheer, "Accuracy in tangential breast treatment set-up: a portal imaging study," Radiother. Oncol. **22**, 317-322 (1991).

11. J. Bijhold, J. V. Lebesque, A. A. M. Hart and R. E. Vijlbrief, "Maximizing setup accuracy using portal images as applied to a conformal boost technique for prostatic cancer," Radiother. Oncol. **24**, 261-271 (1992).

12. S. Shalev, "Progress in the evaluation of electronic portal imaging-taken one step at a time," Int. J. Rad. Oncol. Biol. Phys. **28**, 1043-1045 (1994).

13. A. Noel, P. Aletti, P. Bey, and L. Malissard, "Detection of errors in individual patients in radiotherapy by in vivo dosimetry," Radiother. Oncol. **34**, 144-151 (1995).

14. C. Weltons, J. van Dam , G. Leunens, A. Dutreix, and E. van der Schueren, "Reliability of clinical port films for measuring dose inhomogeneities in radiother. for head and neck tumours," Radiother. oncol. **30**, 167-170 (1994).

15. S. Heukelom, J. H. Lanson and B. J. Mijnheer, "In vivo dosimetry during pelvic treatment," Radiother. Oncol. **25**, 111-120 (1992).

16. J. van Dam, C. Vaerman, N. Blanckaert, G. Leunens, A. Dutreix and E. van der Schueren, "Are port films reliable for in vivo exit dose measurements?," Radiother. Oncol. **25**, 67-72 (1992).

17. S. Heukelom, J. H. Lanson and B. J. Mijnheer, "Comparison of entrance and exit dose measurements using ionization chambers and silicon diodes," Phys. Med. Biol. **36**, 47-59 (1991).

18. G. Leunens, J. van Dam, A. Dutreix, and E. van der Schueren, "Quality assurance in radiotherapy by in vivo dosimetry. 2. Determination of the target absorbed dose," Radiother. Oncol. **19**, 73-87 (1990).

19. G. Leunens, J. van Dam, A. Dutreix, and E. van der Schueren, "Quality assurance in radiotherapy by in vivo dosimetry. 1. Entrance dose measurements, a reliable procedure," Radiother. Oncol. **17**, 141-151 (1990).

20. B. Nilsson, A.-I. Ruden and B. Sorcini, "Characteristics of silicon diodes as patient dosemeters in external radiation therapy," Radiother. Oncol. **11**, 279-288 (1988).

21. C. Mitine, G. Leunens, J. Verstraete, N. Blanckaert, J. van Dam, A Dutreix and E. van der Schueren, "Is it necessary to repeat quality control procedures for head and neck patients?," Radiother. Oncol. **21**, 201-210 (1991).

22. W. J. Graham, D. W. Anderson, D. J. Landry, and C. R. Bogardus, "Accuracy of delivered dose in pelvic irradiation," Int. J. Rad. Oncol. Biol. Phys. **7**, 1117-1119 (1981).

23. J. W. Wong, J. W. Slessinger et al, "Portal Dose Images I: Quantitative Treatment Plan Verification," Int. J. Rad. Oncol. Biol. Phys. **18**, 1455-1463 (1989).

24. M. C. Kirby,and P. C. Williams, "Measurement possibilities using an electronic portal imaging device," Radiother. Oncol. **29**, 237-243 (1993).

25. B. J. M. Heijmen, J. S. Stroom, H. Huizenga, and A. G. Visser, "Application of a fluoroscopic portal imaging system with a CCD camera for accurate in vivo dosimetry(Abst.)," Med. Phys. **20**, 870 (1993).

26. R. Rajapakshe, "Optimization of a real-time portal imaging system for quantitative imaging," Ph.D. Thesis, University of Manitoba, Winnipeg, Canada (1995).

27. B. J. M. Heijmen, J. S. Stroom, H. Huizenga, and A. G. Visser, "In vivo dose measurements using an electronic portal imaging device: A feasibility study," Radiother. Oncol. **24** (Suppl.), S25 (1992).

28. P. Stucchi, L. Conte, C. Mordacchini et al., "The use of an electronic portal imaging device for exit dosimetry," Radiother. Oncol. **37** (Suppl. 1), S21 (1995).

29. M. C. Kirby, and P. C. Williams, "The use an electronic portal imaging device for exit dosimetry and quality control measurements (abs)," Int. J. Rad. Oncol. Biol. Phys. **27** (Suppl. 1), 165 (1993).

30. S. Pistorius and C. Yeboah, "Analysis and modeling of electronic portal imaging exit dose measurements," Radiother. Oncol. **37** (Suppl. 1), S21 (1995).

31. C. Yeboah and S. Pistorius, "Investigation of the factors that affect the use of an electronic portal imaging device for quantitative dosimetry (abs)," Med. Phys **23**, 811 (1996).

32. J. Leong, "Use of digital fluoroscopy as an on-line verification device in radiation therapy," Phys. Med. Biol. **31**, 985-992 (1986).

33. T. R. McNutt, T. R. Mackie, P. Reckwerdt, N. Papanikolaou, and B. R. Paliwal, "Calculation of portal dose using the convolution/superposition method," Med. Phys. **23**, 527-535 (1996).

34. X. Ying, L. Y. Geer and J. W. Wong, "Portal Dose Images II: Patient Dose Estimation," Int. J. Rad. Oncol. Biol. Phys. **18**, 1465-1475 (1990).

35. W. Swindell and P. M. Evans, "Scattered radiation in portal images: A Monte Carlo simulation and a simple physical model," Med. Phys. **23**, 1-11 (1996).

36. V. N. Hansen, P. M. Evans, and W. Swindell, "Transit dosimetry: Computer generated dose images for verification," in Proceedings of the Xith ICCR (International Congress on the use of Computers in Radiation Therapy), edited by A. R. Hounsell, J. M. Wilkinson, and P. C. Williams (Christie Hospital NHS Trust, Manchester, 1993), pp. 166-117.

37. A. Ahnesjō, "Collapsed cone convolution of radiant energy for photon dose calculations in heterogeneous media," Med. Phys. **16**, 577-592 (1989).

38. T. R. Mackie, J. W. Shrimger and J. J. Battista, "A convolution method of calculating dose for 15 MV X-rays," Med. Phys. **12**, 188-196 (1985).

39. R. Mohan and C. Chui, "Differential pencil beam dose computational model for photons," Med. Phys. **13**, 64-73 (1986).

40. A Ahnesjo, P. Andreo, and A. Brahme, "Calculation and application of point spread functions for treatment planning with high energy photon beams," Acta. Oncol. **26**, 49-56 (1987).

41. M. K. Woo, "Analysis of photon beam exit dose using photon point kernels," Phys. Med. Biol. **39**, 687-702 (1994).

42. M. K. Woo and J. R. Cunningham, "The validity of the density scaling method in primary electron transport for photon and electron beams," Med. Phys. **17**, 187-194 (1990).

43. T. Radcliffe, G. Barnea et al, "Monte Carlo optimization of metal/phosphor screens at megavoltage energies," Med. Phys. **20**, 1161-1169 (1993).

44. D. A. Jaffray, J.J. Battista, A. Fenster and P. Munro, "X-ray scatter in megavoltage transmission radiography: Physical characteristics and influence on image quality," Med. Phys. **21**, 45-60 (1994).

45. W. R. Nelson, H. Hirayama and D. W. O. Rogers, "The EGS4 Code System," Stanford Linear Accelerator Centre, Report **SLAC-265 UC-32**, National technical Information Services, U.S. Dept. of Commerce, 5285 Port Royal Road, Springfield, Virg-22161 (1985).

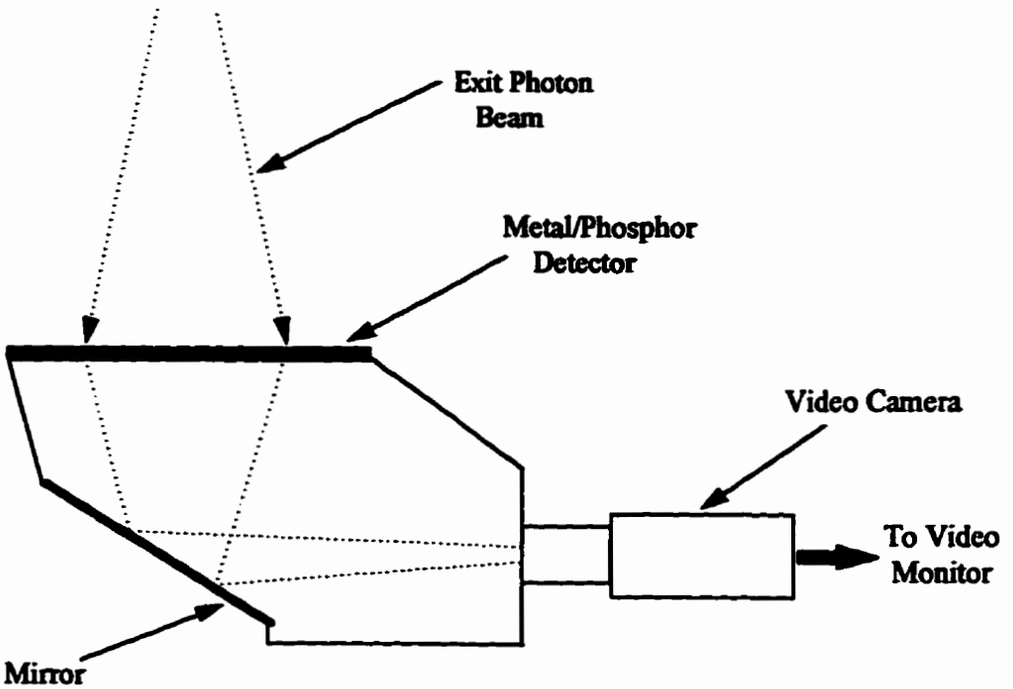

Figure 2-1. Schematic diagram of a video-based electronic portal imaging system.

Chapter 3

Spectral characteristics of exit photon beams

3.1 Introduction

The response of a metal-phosphor portal imaging detector is non-linear[1,2] and depends on the spectral characteristics of the photon beam reaching it. For the polyenergetic beam of photons emerging from a scattering medium and falling on a metal-phosphor detector (i.e., exit photon beams), the spectral characteristics will be influenced by the patient/detector geometry. That is, the thickness of the scattering material, field size, air gap, and detector design will affect the spectral distribution of photons that reach the detector. A proper understanding of such spectral changes and their impact is essential in order to be able to develop accurate models for predicting the dose distribution in the detector. Although a few studies[3,4] on this subject have been conducted in diagnostic radiology, limited information is available at megavoltage energies.[2]

The primary aim of this work has been to analyze and attempt to understand the spectral characteristics of exit photon beams. Monte Carlo methods[5] were used to score the energy spectrum as well as the mean and effective energies of the beam in the detector plane as a function of the patient/detector geometry and incident beam quality. These studies have provided an understanding of the intensity changes and spectral distribution of exit photon beams under various conditions.

3.2 Theoretical considerations

3.2.1 Mean energy

The spectral distribution of a photon beam is characterized by the distribution of fluence or energy fluence with respect to energy. If the fluence (Φ) of photons with energies between 0 and E is denoted by $\Phi(E)$, then the differential distribution (Φ_E) of the fluence with respect to energy is given by

$$\Phi_E = \frac{d\Phi(E)}{dE}$$

It follows that the total fluence (Φ) is given by

$$\Phi = \int_0^{E_{max}} \Phi_E \cdot dE$$

where the product $\Phi_E dE$ is the fluence of photons with energies lying between E and $E + dE$.

The mean energy ($\overline{E}$) of a photon beam can be expressed as:

$$\overline{E} = \frac{\int_0^{E_{max}} \Phi_E \cdot E \cdot dE}{\int_0^{E_{max}} \Phi_E \cdot dE} \qquad (3.1)$$

Alternatively, the mean energy can be calculated from the energy fluence (Ψ_E) distribution:

$$\overline{E} = \frac{\int_0^{E_{max}} \Psi_E \cdot E \cdot dE}{\int_0^{E_{max}} \Psi_E \cdot dE} \tag{3.2}$$

Equations (3.1) and (3.2), however, lead to different values of $\overline{E}$ since Φ_E is not equal to Ψ_E. Regardless of the particular distribution used, the resulting mean energy is not directly related to the mean mass energy absorption coefficient of the beam, for the given medium. It follows that the collision kerma or the dose deposited (under electronic equilibrium conditions) at a point in a medium may not be calculated directly from the mean energy of the beam at that point. To this end, it is sometimes convenient to characterize the beam in terms of the effective (or equivalent) energy.

3.2.2 Effective energy

An effective energy for an energy distribution can be defined as the single energy that gives the same results as the actual energy distribution. In the context of dose deposition, the effective energy of a polyenergetic beam of photons reaching an imaging detector is the monoenergetic energy that has the same mass energy absorption coefficient as the given beam. For a material of atomic number Z, the mean mass energy absorption coefficient of a beam of photons of energies between 0 and E_{max} is calculated from

$$\frac{\overline{\mu_{en}}}{\rho} = \frac{\int_0^{E_{max}} \Psi_E(E) \cdot \frac{\mu_{en}}{\rho}(E,Z) \cdot dE}{\int_0^{E_{max}} \Psi_E(E) \cdot dE} = \frac{K_C}{\Psi} \qquad (3.3),$$

where K_C is the collision kerma. When Ψ and K_C are determined, the effective photon energy E_{eff} is defined by

$$\frac{\overline{\mu_{en}}}{\rho} = \frac{\mu_{en}(E_{eff}, K_C)}{\rho} \qquad (3.4)$$

This effective energy, determined from equations (3.3) and (3.4) , is valid only for determination of K_C or the absorbed dose under conditions of electronic equilibrium.

3.3 Materials and Methods

3.3.1 Monte Carlo code

The Monte Carlo method is a technique that is used to simulate the transport of radiation through matter. It uses knowledge of the probability distributions governing the individual interactions of electrons, photons, neutrons and other charged particles in matter to simulate the random trajectories of these particles. A large number of particles are followed in order to obtain statistically meaningful information about average values of the physical quantities of interest.

Generally, a Monte Carlo simulation code consists of the algorithms to simulate the particle transport, a method for specifying the geometry of the problem and to determine the physical quantities of interest and a means to analyse the information obtained during the simulation. A Monte Carlo code is considered as being either of the class I or class II category, depending on how it treats individual events that lead to bremsstrahlung photons and/or knock-on electrons.[6] For class I algorithms, the energy losses and angular deflections associated with all individual events are grouped together and the energy and direction of the primary electron are not affected by the creation of individual secondary particles. In class II algorithms, individual interactions affect the energy and direction of the primary electron when they create knock-on electrons or bremsstrahlung photons above certain thresholds, although the effects of secondary particle production below these thresholds are still grouped together. Class II models are, in principle, more accurate than class I models because correlations between primary and secondary particles are partially included.

A number of prewritten Monte Carlo codes are available for various applications. One of these is the Electron Gamma Shower version 4 (EGS4) Monte Carlo code system,[5] which is a class II general purpose photon-charged particle transport simulation package. In this system, the photon processes simulated are pair production, Compton scattering, and photoelectric effect. In addition, a coherent or Rayleigh scattering option which may be turned on/off by the user is available. For electrons, bremsstrahlung, Bhabha scattering, Moller scattering, annihilation at rest or in flight, Moliere multiple scattering, and ionization loss are considered. To use EGS4, the cross-section data for the various

particle processes are first generated by PEGS4, a Preprocessor for EGS4, using theoretical and empirical formulae. In addition, the user writes a "user code" through which communication with EGS4 takes place. This user code consists of a main program and two subroutines for specifying the geometry of the simulation and the output of the physical quantities of interest.

In this work a user code called INHOM[5,7,8] was used with EGS4. This user code was written to simulate the passage of a cylindrically symmetric electron or photon beam passing through a semi-infinite slab with regions of two different materials. It was originally designed to model a narrow as well as a broad parallel beam, a point source of radiation on an axis, and a pencil beam and to score the resulting dose distribution in an arbitrary number of depth and radial bins. To obtain estimates of statistical uncertainties in the physical quantities of interest, the total number of particle histories were divided into an arbitrary number of batches and the required quantities scored for each of these batches. From these data the mean quantity and the standard deviation are calculated. For this study, the code was modified to include the additional materials present in the simulation geometry and to make it possible to score the energy spectrum of the beam at an arbitrary depth.

Particle transport, in EGS4, is controlled by a number of parameters: AE and AP denote the energy thresholds required for the creation of secondary electrons and photons, respectively, while ECUT and PCUT represent the energy cutoffs (i.e. minimum total energy) of electrons and photons that are transported. In this work, PCUT = AP = 10

keV, and ECUT = AE = 561 keV were used. An ECUT of 561 keV was employed because it resulted in a decrease in calculation time but did not significantly affect the contributions from those processes which depend on electron transport. Assigning lower parameter values did not significantly affect the results of the simulations. All simulations employed between 10^6 and 3×10^6 histories (i.e. incident photons). This number of histories was chosen since it led to statistically meaningful results while keeping the time required for each simulation in the range of 5 minutes to 6 hours on an HP9000-715/75 computer workstation.

3.3.2 Geometry of the Monte Carlo simulations

The geometry used in the Monte Carlo simulations is shown in figure 3-1. It consists of a cylindrically symmetric parallel beam of photons incident on a water phantom/slab at a specified field radius. The phantom/slab is homogeneous, of infinite lateral extent and of finite thickness, and is perpendicular to the central axis of the beam. On exiting the slab the beam is allowed to fall on a portal imaging detector located at a given distance from the distal surface of the phantom/slab and consisting of a 500-mg/cm^2 thickness of Gd_2O_2S (gadolinium oxysulfide) phosphor on a copper plate of thickness 2.25-cm.[9,10] This detector geometry was chosen for this study because it is similar to the metal-phosphor detectors used on commercial video electronic portal imaging devices, and identical to the custom detector used at the Manitoba Cancer Treatment and Research Foundation on a BEAMVIEW system (Siemens Medical Labs, California). For simplicity, the detector has

been modeled as a slab of infinite lateral extent to conform to the idealized slab geometries being studied.

It is relatively time consuming to simulate the physical quantity of interest on the central axis of the beam in the detector plane using the geometry described in the preceding text, since every single particle in the beam will have to be followed. However, most of these particles are distant from the scoring region and do not contribute to the physical quantities being scored. In addition, only a limited amount of information (i.e. those of a single field size) is obtained from this geometry in a single simulation and the statistics would be relatively poor since the scoring region is limited to a small volume along the central axis. To save time and also to obtain statistically meaningful results in the simulations, the cylindrical symmetry of the problem was taken advantage of. The statement of the symmetry argument, known as the reciprocity theorem,[6,11] states that the same results will be obtained, if instead of simulating a parallel beam of large cross-sectional area A and scoring the quantity of interest in a smaller region of area a, the simulations are carried out using a pencil beam of cross-sectional area a and scoring in a larger region of area A. The application of this theorem not only improves the statistics of the simulations, but also makes it possible to obtain the required data for an arbitrary number of field sizes at the same time.

Using the user code INHOM and applying the reciprocity theorem, the energy spectrum as well as the mean and effective energies of exit photon beams at the copper surface entrance and at the copper-phosphor interface of the portal imaging detector were scored

for a number of phantom thicknesses (5-40 cm), field sizes, and air gaps (i.e. distance between the exit surface of phantom/slab and detector). Incident photon beams of energies 1.25, 2, and 5 MeV were simulated. Unless otherwise specified, calculations of the mean energy are carried out using equation (3-1).

3.4 Results and Discussion

3.4.1 Energy spectrum as a function of air gap

In order to study the variation of energy spectrum of photon beams reaching the portal imaging detector with air gap, a 20 cm thick phantom and a 30 x 30 cm^2 field were used while the air gap was varied from 0 to 60 cm. Figure 3-2 shows the spectrum at the copper-phosphor interface of the detector. For 1.25-MeV incident beam, five distinct regions may be identified on the spectrum, while for 2-, and 5-MeV beams, an additional region is discernible. These regions have been named in figure 3-3, which depicts the general shape of the spectra. The regions include (from right to left) the primary component designated by region a, the high energy scattered component (region b), and a section showing the transition from high to intermediate energies (region c). The remaining regions consist of the scattered photons of intermediate energies (region d) on which is superimposed a narrow annihilation peak at energy of 0.511 MeV (region e), and, finally, a broad low energy peak (region f). Unless otherwise specified, these annotations will be used in the sections to follow since the spectra obtained under different conditions have the same general shape as the spectrum under consideration.

As seen in these spectra (figure 3-2), the intensity of the primary and high energy scattered components are not significantly affected by the air gap. This is because the primary photons emerge from the phantom unscattered and most, except a negligibly small fraction that are scattered in the air volume, are detected regardless of the magnitude of the air gap. Furthermore, the high energy scattered photons reaching the detector were scattered through small angles by the phantom, according to the kinematics of Compton scattering. As a result, increasing the air gap did not significantly affect the probability of detecting a primary or a high energy scattered photon. In contrast, the intensity of the low as well as the intermediate energy scattered component decreases significantly as the air gap increases. This is attributed to the fact that the low energy scattered photons are generally scattered through large angles. Consequently, increasing the air gap increases the probability that a low energy scattered photon escapes the detector. A similar trend is seen in the spectra at the copper surface entrance (figure 3-4). At both the entrance and the Copper-phosphor interface of the detector, a broad peak in the spectra, ascribed to multiple scattering, was found to occur at energies of between 50 and 200 keV. The intensity of this peak is observed to be higher on the copper surface entrance than at the copper-phosphor interface due to the absorption of a significant fraction of the low energy scattered component in the copper plate.

In Compton scattering the recoiling electron is strongly forward-directed at high incident photon energies even though it becomes relatively unlikely that photons will be 180°-backscattered. This occurs because the high forward momentum in the collision causes most of the electrons and most of the scattered photons to be strongly forward-directed

when the incident energy is high. In this situation high energy photons scattered at a wide range of angles must be associated with electrons recoiling at nearly 0°. There is therefore a high probability of electron scattering near $\theta = 0°$, which is associated with the maximum electron energy. As a result, the highest concentration of Compton electrons occurs near the maximum electron energy, with a correspondingly high peak of low-energy scattered photons occurring at energies less than one-half of the electron's rest energy.[12,13] This is evident in the spectra shown in figures 3-2 and 3-4, in which the low-energy peak is found to occur in an interval centred at around 150 keV.

The second peak in the spectra occurs at 0.511 MeV for 2, and 5 MeV incident beams. This peak results from the annihilation of positrons that were produced by pair production interactions in the water phantom as well as the copper plate. Consequently, the peak is higher at the Copper-phosphor interface, where the additional contributions from the Cu plate are included. The high atomic number of the copper plate increases the probability of pair production, thus increasing the number of annihilation photons over that which would originate from the water phantom only. For 1.25-MeV beams, the peak in question is not visible in the spectra because the number of pair production interactions taking place decreases with decreasing incident energy such that only a few of these interactions are recorded at 1.25-MeV. This trend is consistent, with a higher annihilation peak observed in the spectra for 5 MeV than for 2 MeV incident beams.

Comparison of the spectra at the Copper-phosphor interface with that at the entrance of the detector also shows that the intensity of the scattered photons of intermediate energies

is higher at the Copper-phosphor interface than the entrance. This increase is due to the scattering of photons in the copper plate. On the contrary, for the high energy scattered component, no significant difference was seen between the spectra at the entrance and the copper-phosphor interface of the detector. These spectra show that the intensity of photons detected in the high energy region is roughly independent of energy of a detected photon. This observation is consistent with the prediction of the differential Klein-Nishima (KN) cross-section per unit energy for expulsion of the Compton electron with energy of between T_e and $T_e + dT_e$, or for the Compton scattered photon to emerge with energy of between E and E + dE.[12,13] That is, the differential KN cross-section predicts that the energy spectrum of scattered photons/recoiling electrons at the point of production from a high energy incident photon is almost flat except in the low/high energy region where a high peak occurs. It follows therefore that the high energy region of the spectra, depicted in figures 3-2 and 3-4, consists of singly scattered photons. Furthermore, the high energy component shifts to higher energies as the air gap increases because more singly scattered photons are able to escape the detector. Although the differential KN cross-section can be employed to compute the initial energy spectrum of Compton scattered photons, the spectrum of scattered photon energies present at a point in an extended medium under irradiation is generally degraded by the presence of scattered photons that have lost varying amounts of their energies. For this reason the spectra of photon energies at the copper-phosphor interface and at the copper surface entrance of detector, shown in figures 3-2 and 3-4 respectively, are different from the initial spectra

particularly in the low and intermediate energy regions, and therefore cannot be predicted by the differential KN cross-section.

3.4.2 Field size dependence of energy spectrum

A 20 cm thick phantom, with a 30 cm air gap was used to study the energy spectra at the Copper-phosphor interface as a function of field size. The results for 1.25-, 2-, and 5-MeV incident beams are depicted in figure 3-5, which shows the intensity of the low energy component, of the annihilation photons, and of the intermediate energy scattered photons increasing with field size. At the same time, the high energy component extends to lower energies, causing the transition from high to intermediate energies to occur at progressively lower energies. This extension effect of the high energy component may be described in terms of a quantity denoted by E_{50}, which may be defined, in the high-to-intermediate energy transition region, as the energy of photons at the 50% transition point. As illustrated in figure 3-6, E_{50} decreases with increasing field size. Interestingly, the spectra (figures 3-2 and 3-5) show that the effects of increasing field size and increasing air gap and vice versa are roughly complimentary and lead to the assertion that equivalent field size techniques may be used to model the air gap.

As the incident energy becomes higher, there is not only a reduction in intensity of the high energy scattered photons, but a reduction in intensity of this component relative to that of the low energy peak and also to the annihilation photons is observed. These may be explained by a number of factors. Firstly, there is a reduction in intensity of the high

energy scattered photons because the Klein-Nishima differential cross-section for scattering through a given solid angle decreases with increasing energy. Once a Compton interaction has occurred, however, the scattered photon, on average, progressively retains a smaller fraction of the available energy as the incident energy becomes higher.[12] It follows therefore that, with increasing incident energy, the intensity of the high energy component decreases relative to that of the low energy photons. Secondly, the annihilation photons increase in intensity with increasing incident energy, since more pair production interactions occur as the energy becomes higher. Consequently, the intensity of the high energy component relative to the annihilation photons decreases as the incident energy increases. The spectra at the copper surface entrance of detector (figure 3-7) show a similar trend.

3.4.3 Dependence of energy spectrum on phantom thickness

The dependence of energy spectrum at the Copper-phosphor interface on phantom thickness was investigated by keeping the field size fixed at 30 x 30-cm^2, and the air gap at 30-cm, while varying the phantom thickness from 5 to 40 cm. In figure 3-8, the spectra for 1.25, 2, and 5 MeV incident photons are shown. As expected, there is a decrease in primary transmission as the phantom thickness increases. As a result, fewer pair production interactions occur in the copper plate as the phantom thickness becomes larger, leading to a reduction in intensity of the annihilation photons. Similarly, the intensity of the intermediate energy scattered photons decreases with increasing phantom thickness. This reduction in intensity results mainly from the decrease in primary

transmission as the phantom thickness becomes larger, which leads to fewer primary photons entering the copper plate, and correspondingly less scatter production in this material. This effect (i.e. reduction in intensity of the intermediate energy scattered photons with increasing phantom thickness) becomes less significant as the incident energy increases since the probability of a primary photon scattering in the copper plate decreases as the primary energy increases. Unlike the annihilation and the intermediate energy scattered photons, the low and the high energy scattered components of the spectra build up to a maximum and thereafter decrease with increasing phantom thickness. This trend occurs because the exponential attenuation of the primary in the phantom results in the production of phantom scatter at a progressively lower rate as the phantom thickness increases. At the same time, some of the scattered photons which were generated upstream in the phantom do not deposit all their energy locally, but travel further downstream; thus the intensity of this component increases to a maximum, at which point it decreases with increasing phantom thickness. The net effect therefore is a buildup of the scattered photons to a maximum, beyond which their intensity decreases as the phantom thickness increases. Although this effect is present for the entire scattered photon spectrum, the initial increase in intensity is not seen at intermediate energies due to the additional contribution of the copper-scattered photons (whose intensity is progressively larger for smaller phantom thicknesses) to this component.

3.4.4 Variation of mean and effective energies with field size

The mean energy of exit photon beams that reach the portal imaging detector has been investigated as a function of field size. For the scattered component of the beam at the copper-phosphor interface of the detector, the mean energy as a function of field size is shown in figure 3-9. The mean energy initially increases with increasing field size, reaches a maximum at intermediate field sizes, and thereafter decreases and asymptotically approaches a limit (independent of the air gap) at large fields. The value of maximum mean energy also does not depend on air gap, but is reached at larger field sizes as the air gap increases. That this shifting effect preserves the general shape of the curves provides additional support for the use of an equivalent field size technique for modeling the air gap.

The observed shape of the mean energy curves can be explained by considering the energy spectrum of the scattered photons at the copper-phosphor interface of the detector (figure 3-5). This spectrum reveals four effects which come into play as the field size is increased: (i) an increase in the intensity of the low energy scattered component, (ii) a rise in the annihilation peak, (iii) an increase in intensity of the intermediate energy scattered photons and a corresponding decrease in the width of this component, and (iv) an extension of the high energy scattered component to lower energies. For small field sizes, the area under the spectrum of the intermediate energy scattered photons is large compared to those of the other regions. As a result, the relative contribution of factor (iii) to the mean energy dominates for small field sizes. As the field size increases the relative

increase in the area under the spectrum occupied by the high energy scattered photons becomes larger. Consequently, the mean energy increases with field size until the high energy component has extended to include a wide range of lower energies, at which point the contribution of the intermediate energy scattered photons becomes less significant. At this point, the mean energy reaches a maximum and starts to decrease with further increase in field size, since the high energy component progressively extends to lower energies. This reduction of the mean energy is further reinforced by the increase in intensities of the low energy component and the annihilation photons with increasing field size. In figure 3-10, the variation of the mean energy of scattered photons with field size for a variety of phantom thicknesses has been compared (see discussion in section 3.4.6).

The mean and effective energies at the copper-phosphor interface, and the mean energy at the copper surface entrance of the detector are compared with each other in figure 3-11. Unlike the copper-phosphor interface, the mean energy curve at the copper surface entrance does not have a significant initial build up. This occurs because the intermediate energy scattered component, whose relative contribution gives rise to the initial buildup, is not as large at the copper surface entrance as at the copper-phosphor interface. Furthermore, for small field sizes, the relative increase in intensities of the intermediate energy scattered component and of the annihilation photons at the copper-phosphor interface resulting from the presence of the copper plate (which tends to decrease the mean energy below that at the entrance) is large compared to the preferential attenuation effect of the low energy scattered photons in the copper plate (whose effect is to increase the mean energy at the interface over that at the entrance). The contribution of the latter

effect is smaller since there are relatively few low energy scattered photons to be preferentially attenuated in the copper plate at small fields (see figure 3-7). For large field sizes, however, the converse is true. The mean energy is therefore higher at the copper surface entrance than the copper-phosphor interface for small field sizes, whereas for large field sizes the reverse is seen.

Figure 3-11 shows that the effective energy at the copper-phosphor interface as a function of field size has a shape similar to that of the mean energy at the interface. However, the effective energy is lower since the spectrum is weighted by the mass-energy absorption coefficient for the phosphor, which increases rapidly with decreasing energy below about 1-MeV (figure 3-12). The mass energy absorption coefficient reaches a minimum at 2-MeV, at which point it begins increasing. For incident energies above this value the effective energy could not be calculated because, in this energy range, the mass-energy absorption coefficient for the phosphor no longer has a one-to-one relationship with energy, leading to a nonunique effective energy. Similarly, between energies of about 40 and 80 keV the mass energy absorption coefficient for the phosphor does not have a one-to-one relationship with energy due the occurrence of the k-edge around 50-keV. This, however, did not pose a problem since we were working above this range of energies. Unlike the phosphor, the mass energy absorption coefficient for water, increases rapidly with decreasing energy below 50-keV and does not vary significantly with energy between 0.05 and 10 MeV. The differences in the mass-energy absorption coefficient for the two materials under consideration (i.e. phosphor and water) will lead to different effective energies for a given beam of photons.

For all detected photons (i.e. primary plus scatter) the mean energy at the Copper-phosphor interface as a function of field size is shown in figure 3-13. For small field sizes the mean energy decreases slowly with increasing field size. At intermediate field sizes, however, it begins to decrease rapidly till large field sizes are reached, at which point it starts to decrease slowly again and eventually approaches an asymptotic minimum. This minimum value is independent of air gap since radiation equilibrium is present at large field sizes, leading to an unchanging spectrum as a function of air gap for the field sizes in question.

The shape of the mean energy curves are determined by the relative contributions of the scattered photons and of the primary component. Although the intensity of the primary component is independent of field size (for a fixed phantom thickness), the relative primary contribution decreases with increasing field size since the fraction of scattered photons increases. This leads to an increase in the relative scatter contribution as the field size increases and a corresponding decrease in the mean energy. For small field sizes the mean energy at the copper-phosphor interface does not seem to approach the primary energy, as would be expected. If data for very small field sizes are included, as in figure 3-14, it becomes apparent that the mean energy at the copper-phosphor interface approaches the primary energy in the limit of zero field size. Unlike the copper-phosphor interface, the mean energy curve at the copper surface entrance clearly approaches the primary photon energy even if data for very small field sizes are not included. The explanation for this is that the shape of the curve at the entrance is determined mainly by the relative contributions of the primary and scattered photons originating from the water phantom.

At the copper-phosphor interface however there is an additional effect introduced by the scattered photons that were produced in the copper plate. For very small field sizes the contribution of these copper-scattered photons is significant compared to that of the phantom-scattered photons since the intensity of the latter is limited regardless of the size of the air gap. As a result, the effect of the copper-scattered photons is manifested at the interface for very small field sizes, leading to lower mean energies at the interface than the entrance of the detector. This trend is reversed for large field sizes where the increase of number of copper-scattered photons (which tends to decrease the mean energy at the interface below that at the entrance) is small in comparison to the preferential attenuation effect of the copper plate on the low energy phantom-scattered photons (which tends to increase the mean energy at the copper-phosphor interface over that at the entrance).

Moreover, for the geometry corresponding to figure 3-14 (i.e. 20-cm thick phantom and 30 cm air gap), most changes in the mean energy occur at field sizes of between 10 x 10 and 200 x 200 cm^2. Qualitatively, this effect results from the manner in which phantom-scatter reaching the detector increases with field size for a given air gap. In the case of small air gaps, there is a rapid increase of scatter with field size, with the rate of increase becoming less as the field size increases. For large air gaps, however, the rapid increase of scatter in the detector plane occurs at larger field sizes and is preceded by a more gradual increase. Therefore, for a large air gap of magnitude 30-cm, say, one sees a slow increase of scatter beginning at a field size of 0 x 0 cm^2 and extending to about 10 x 10 cm^2, followed by a rapid increase of scatter. The gradual increase of scatter at small field sizes leads to the initial slow decrease in the mean energy observed at field sizes of between 0 x

0 and 10 x 10 cm^2 (figure 3-14), whereas the rapid increase of scatter at intermediate fields results in the rapid reduction of the mean energy at field sizes of between 10 x 10 and 200 x 200 cm^2. The mean energy does not vary significantly at infinitely large field sizes since radiation equilibrium conditions are believed to be approached under those conditions.

3.4.5 Mean and effective energies as a function of air gap

The mean energy of the scattered photons reaching the copper-phosphor interface as a function of air gap is shown in figure 3-15. As the air gap increases, the mean energy builds up to a maximum and decreases thereafter. This initial buildup is more gradual for larger field sizes, whereas the maximum mean energy is roughly independent of field size. An understanding of this behaviour can be obtained from an analysis of the energy spectrum of the beam at the copper-phosphor interface (figure 3-2). For small air gaps, the intensities of the low and the intermediate energy scattered photons decrease with increasing air gap, whereas that of the high energy scattered component remains constant. Consequently, for small air gaps the relative contributions of the low and intermediate energy components decrease significantly as the air gap increases, with a corresponding increase in the relative contribution of the high energy scattered component. This leads to an initial buildup of the mean energy. In contrast, for large air gaps, the area under the spectrum of the low and intermediate energy scattered photons decreases with increasing air gap at a relatively lower rate than the area occupied by the high energy scattered component. It follows therefore that, for the range of air gaps in question, the effect of

reduction in area under the spectrum of the high energy component on the mean energy is large compared to those of the other scattered components. For this reason a decrease in the mean energy is observed for large air gaps. In the limit of large field sizes the mean energy is independent of air gap since under such conditions it is assumed that radiation equilibrium is achieved and the spectrum does not vary with changing air gap.

For all detected photons (i.e. primary and scatter) the shape of the mean energy curve, as depicted in figure 3-16, is determined by the relative contributions of the primary and scattered components. While the primary component is almost independent of air gap, the intensity of the scattered component decreases with increasing air gap. As a result, the relative contribution of the scattered photons decreases as the air gap become larger, with a corresponding increase in the relative primary contribution. For this reason, the mean energy of the beam increases with air gap. This increase is more gradual for larger field sizes. Under large air gap conditions, there is limited scatter and the rate of buildup of the mean energy progressively decreases. Consequently, the mean energy approaches an asymptotic maximum in the limit of large air gaps. At the copper-phosphor interface of detector, this maximum seems to be lower than the expected value, namely, the primary photon energy. However, as discussed in section 3.4.4, if data for very small field sizes are included in the analysis, one observes that the maximum value of the mean energy at the copper-phosphor interface does, in fact, approach the primary photon energy.

In figure 3-17, the mean and effective energies of the scattered component of the beam reaching the copper-phosphor interface are compared to each other and to the mean

energy at the copper surface entrance. For small air gaps the mean energy at the interface is higher than that at the entrance because the intensity of the low energy scattered photons reaching the detector is large. Consequently, the effect of their preferential attenuation in the copper plate (which tends to increase the mean energy at the interface over that at the entrance) is correspondingly large, and outweighs the effect of the additional intensity of the annihilation and the scattered photons resulting from the presence of the copper plate (which contributes to a reduction in the mean energy at the interface below that at the entrance of detector). This trend is reversed for large air gaps, where the intensity of the low-energy scattered photons reaching the copper surface entrance is so small that their preferential attenuation in the copper plate has an insignificant effect. Moreover, figure 3-17 reveals that the point at which the mean energy curve at the interface crosses that at the copper surface entrance of detector occurs at smaller air gaps for higher incident energies. This is because the relative contribution of the annihilation photons produced by the copper plate and reaching the copper-phosphor interface (whose effect is to decrease the mean energy at the interface below that at the entrance) increases with incident energy. Consequently, as the incident energy increases, the effect of these copper-produced annihilation photons on the mean energy at the interface also increases and begins to outweigh the preferential attenuation effect of the copper plate at progressively smaller air gaps.

As discussed in section 3.4.4, the effective energy at the copper-phosphor interface has a shape similar to that of the mean energy at this point. The only major difference between these two quantities is that the effective energies are of much lower values. These

changes in the mean and effective energies of the scattered photons are reflected in the corresponding curves for the entire beam (primary plus scatter), shown in figure 3-18.

3.4.6 Dependence of mean and effective energies on phantom thickness

As a function of phantom thickness, the mean energy of the scattered photons at the copper-phosphor interface of the detector is determined by the relative proportions of: (i) the low energy scattered photons, (ii) the intermediate energy scattered and annihilation photons, and (iii) the high energy scattered component. As the phantom thickness increases, the primary transmission is reduced and this, in turn, reduces the relative intensity of the annihilation photons (which are predominantly produced in the copper plate) and of the intermediate energy scattered photons (which consist, in part, of the copper-scattered photons). This reduction in the relative proportions of the annihilation and/or the intermediate energy scattered photons, together with the increase in the relative intensity of the high energy scattered component with phantom thickness (figure 3-19), tend to increase the mean energy at the interface. For 1.25 and 2-MeV beams this effect is offset by the increase in the relative intensity of the low energy scattered photons (figure 3-19), whose effect is to decrease the mean energy. These factors contribute differently to the mean energy (depending on the field size/air gap, as discussed in section 3.4.3). For small field sizes, the relative contribution of the low energy photons is small since the intensity of this component is limited. As a result, the change in the mean energy with increasing phantom thickness, for small field sizes, is determined mainly by the decrease in relative intensity of the annihilation and/or of the intermediate energy scattered photons,

and also by the increase in the relative intensity of the high energy scattered component. Consequently, for the range of field sizes in question, the mean energy at the interface increases with phantom thickness (refer to figure 3-10). This trend, in the case of 1.25 and 2-MeV beams, is reversed for large field sizes where the relative intensity of the low energy scattered photons is large and leads to a correspondingly large relative contribution to the mean energy.

Unlike 1.25 and 2 MeV incident beams, the relative contribution of the low energy scattered component to the mean energy, for 5-MeV beams, decreases with increasing phantom thickness (figure 3-19) and tends to increase the mean energy at the interface. In addition, the relative intensity of the annihilation photons, for this incident energy, is large and so the effect of its decrease with increasing phantom thickness on the mean energy is correspondingly large. For 5-MeV beams, therefore, the decrease in the relative contributions of the low energy scattered, of the annihilation and intermediate energy scattered photons, as well as the increase in the relative intensity of the high energy scattered component with increasing phantom thickness all contribute to an increase in the mean energy. The net effect is an increase in the mean energy with phantom thickness for all field sizes studied (figure 3-10(c)).

In figure 3-20, a comparison is made between the mean and effective energies of the scattered photons at the interface and the entrance of the detector. For small phantom thicknesses the mean energy at the entrance is higher than that at the interface because, for this range of phantom thicknesses, the additional intensity of the annihilation photons

produced in the copper plate and reaching the interface, and the intensity of the copper-scattered photons at this point is large. Consequently, the influence of these factors on the mean energy at the interface (namely, a reduction in this quantity below that at the entrance) is higher than that of the preferential attenuation of the low energy scattered photons in the copper plate (which tends to increase the mean energy at the interface over that at the entrance). For 1.25 and 2-MeV beams the reversed trend is seen at large phantom thicknesses, where the relative intensity of the annihilation and/or the copper-scattered photons is limited due to the relatively small primary transmission through the phantom.

In contrast, for the 5-MeV beam, the mean energy of the scattered photons reaching the copper surface entrance of the detector is higher than that at the copper-phosphor interface for all phantom thicknesses studied (figure 3-20). This arises because the intensity of the copper-produced annihilation photons reaching the copper-phosphor interface increases with incident energy. For the 5-MeV beams the relative intensity of these annihilation photons is large and its influence on the mean energy at the interface (i.e. a reduction in this quantity below that at the entrance) outweighs that of the preferential attenuation effect of the low energy scattered photons in the copper plate. At the copper surface entrance of the detector the mean energy of the scattered photons, for the incident energy in question, does not vary significantly with changing phantom thickness. The reason for this is that the decrease in relative intensity of the annihilation photons with increasing phantom thickness at the entrance (which results in an increase in the mean energy) is almost exactly balanced by the effect of the relative build up of the

low energy scattered component (which tends to decrease the mean energy). Since the characteristics of the effective energy shown in figure 3-20 are similar to those of the curves discussed in section 3.4.4, this quantity does not merit any additional consideration. The corresponding curves for the entire beam of photons (primary plus scatter) are shown in figure 3-21. The trends seen in this figure follows directly from the differences in mean/effective energies of the scattered photons presented in the foregoing discussion.

In figure 3-22, the mean energy of the entire beam of photons (primary plus scatter) at the copper-phosphor interface of detector is shown as a function of phantom thickness for a variety of field sizes. The reduction in the mean energy arises because, with increasing phantom thickness, the relative primary contribution to the mean energy decreases, with a corresponding increase in the relative scatter contribution (see figure 3-23).

As observed earlier in section 3.4.4, the mean energy at the copper-phosphor interface of detector approaches a limit, independent of air gap, at large field sizes. The ratio of this mean energy limit and the primary energy is plotted as a function of phantom thickness in figure 3-24. As expected, the shapes of the curves are similar to those of the mean energy discussed in the preceding text. However, the decrease in the relative mean energy limit with increasing incident energy, for the scattered component of the beam, was not expected. An explanation for this is as follows: although the primary transmission increases with a corresponding decrease in the intensity of the high energy singly scattered component as the incident energy becomes higher, the contribution of the annihilation and/or the low energy scattered photons relative to that of the high energy component

increases with incident energy (as discussed in section 3.4.2). As a result, the relative mean energy limit becomes lower as the incident energy is increased. Unlike the scattered photons, the relative mean energy curve of the entire beam of photons (primary plus scatter) in the limit of large fields, depicted in figure 3-24(b), indicates that the relative mean energy limit is almost independent of incident energy. This means that, for a specified phantom thickness, the increase in the relative intensity of the annihilation and/or the low energy scattered components with increasing incident energy (which contributes to a reduction in the relative mean energy limit) is roughly balanced by the relative increase in primary transmission (whose effect is to increase the relative mean energy limit with incident energy). Similar observations were made for the effective energies at the copper-phosphor interface (see figure 3-25).

3.5 Conclusions

The spectral characteristics of exit photon beams have been studied. It was found that the intensity, energy spectrum, mean and effective energies of the beams are significantly affected by variations in the patient/detector geometry. This indicates that to accurately calculate the dose deposited in the high atomic number portal imaging detector as a function of field size, air gap, and phantom thickness, both the primary and the scattered components and their effective energies need to be considered. Comparisons made between the energy spectra at the copper surface entrance and those at the copper-phosphor interface showed a significant difference. A corresponding difference in the mean energies was observed. This implies that the detector design plays an important role

and needs to be carefully considered when carrying out electronic portal imaging dosimetry. Interestingly, the effects of an increasing air gap and an increasing field size (and vice versa) were found to be roughly complementary. Therefore, we hypothesize that equivalent field size techniques may be used to account for intensity and spectral changes arising from air gap variations.

References

1. D. A. Jaffray, J. J. Battista, A. Fenster, and P. Munro, "Monte Carlo studies of x-ray energy absorption and quantum noise in megavoltage transmission radiography," Med. Phys. **22,** 1077-1088 (1995).

2. D. A. Jaffray, J. J. Battista, A. Fenster, and P. Munro, "X-ray scatter in megavoltage transmission radiography: Physical characteristics and influence on image quality," Med. Phys. **21,** 45-60 (1994).

3. H.-P. Chan and K. Doi, "Physical characteristics of scattered radiation in diagnostic radiology: Monte Carlo simulation studies," Med. Phys. **12,** 152-165 (1985).

4. C.-W. Cheng, K. W. Taylor, and A. F. Halloway, "The spectrum and angular distribution of x-rays scattered from a water phantom," Med. Phys. **22,** 1235-1245 (1995).

5. W. R. Nelson, H. Hirayama, and D. W. O. Rogers, "The EGS4 Code System," Stanford Linear Accelerator Centre Report SLAC-265 UC-32, National technical Information Services, U.S. Dept. of Commerce, 5285 Port Royal Road, Springfield, Virg-22161 (1985).

6. D. W. O. Rogers and A. F. Bielajew, "Monte Carlo Techniques of Electron and Photon Transport for Radiation Dosimetry," *in The Dosimetry of Ionizing Radiation,*

Volume III, edited by K. R. Kase, B. E. Bjarngard and F. H. Attix, (Academic Press, Inc., 1990).

7. D. W. O. Rogers, "Fluence to dose equivalent conversion factors calculated with EGS3 for electrons from 100 keV to 20 GeV and photons from 11 keV to 20 GeV," Health Physics **46**, 891-914 (1984).

8. D. W. O. Rogers, "Low energy electron transport with EGS", Nuclear Instruments and Methods **A227**, 535-548 (1984).

9. B. Work, T. Radcliffe, K. W. Leszczynski, S. Shalev, and R. Rajapakshe, "Optimization of metal/phosphor screens for on-line portal imaging," Med. Phys. **21**, 227-235 (1994).

10. T. Radcliffe, G. Barnea, B. Work, R. Rajapakshe, and S. Shalev, "Monte Carlo optimization of metal/phosphor screens at megavoltage energies," Med. Phys. **20**, 1161-1169 (1993).

11. F. H. Attix, *Introduction to Radiological Physics and Radiation Dosimetry*, (J. Wiley and Sons, Inc., 1986).

12. F. H. Attix, *Introduction to Radiological Physics and Radiation Dosimetry*, (J. Wiley and Sons, Inc., 1986), 124-159.

13. D. A. Anderson, *Absorption of Ionizing Radiation*, (University Park Press, 1984), 113-132.

14. E. Storm and H. I. Israel, "Photon cross sections from 1 keV to 100 MeV for elements Z = 1 to Z = 100," Nuclear Data Tables A7, 565-681 (1970).

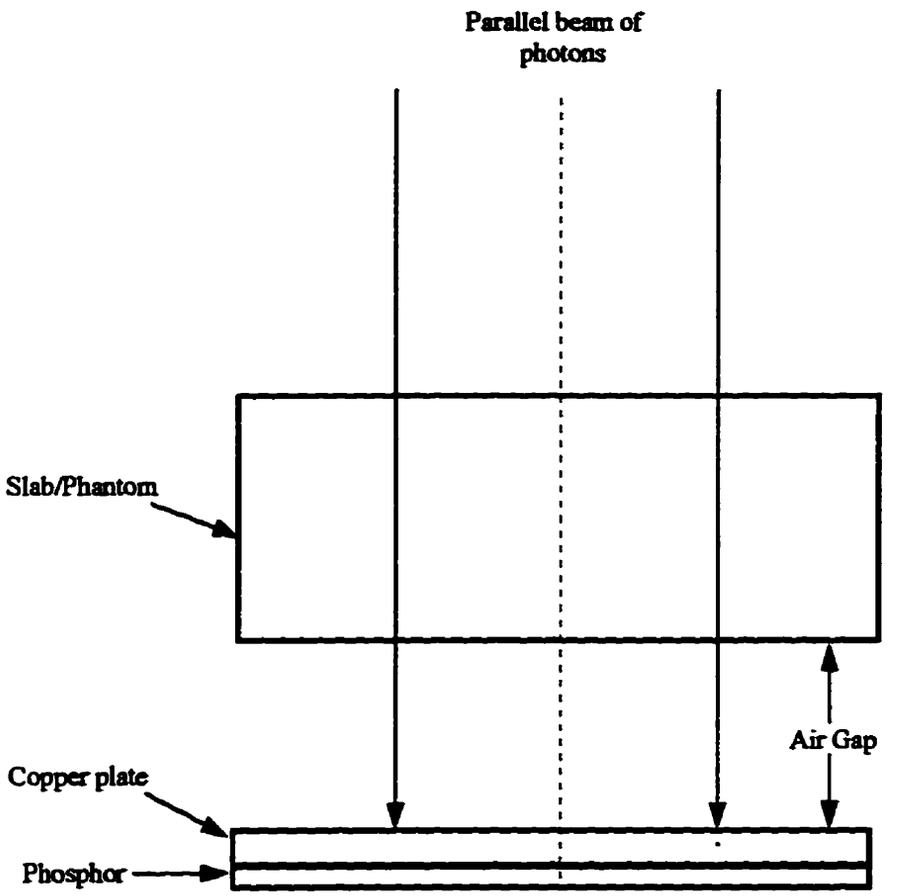

Figure 3-1. Schematic diagram of the geometry used for the Monte Carlo simulations. A parallel beam of monoenergetic photons were incident on a slab water phantom at a specified field radius. The polyenergetic beam that emerges from the phantom is allowed to fall on a metal-phosphor detector.

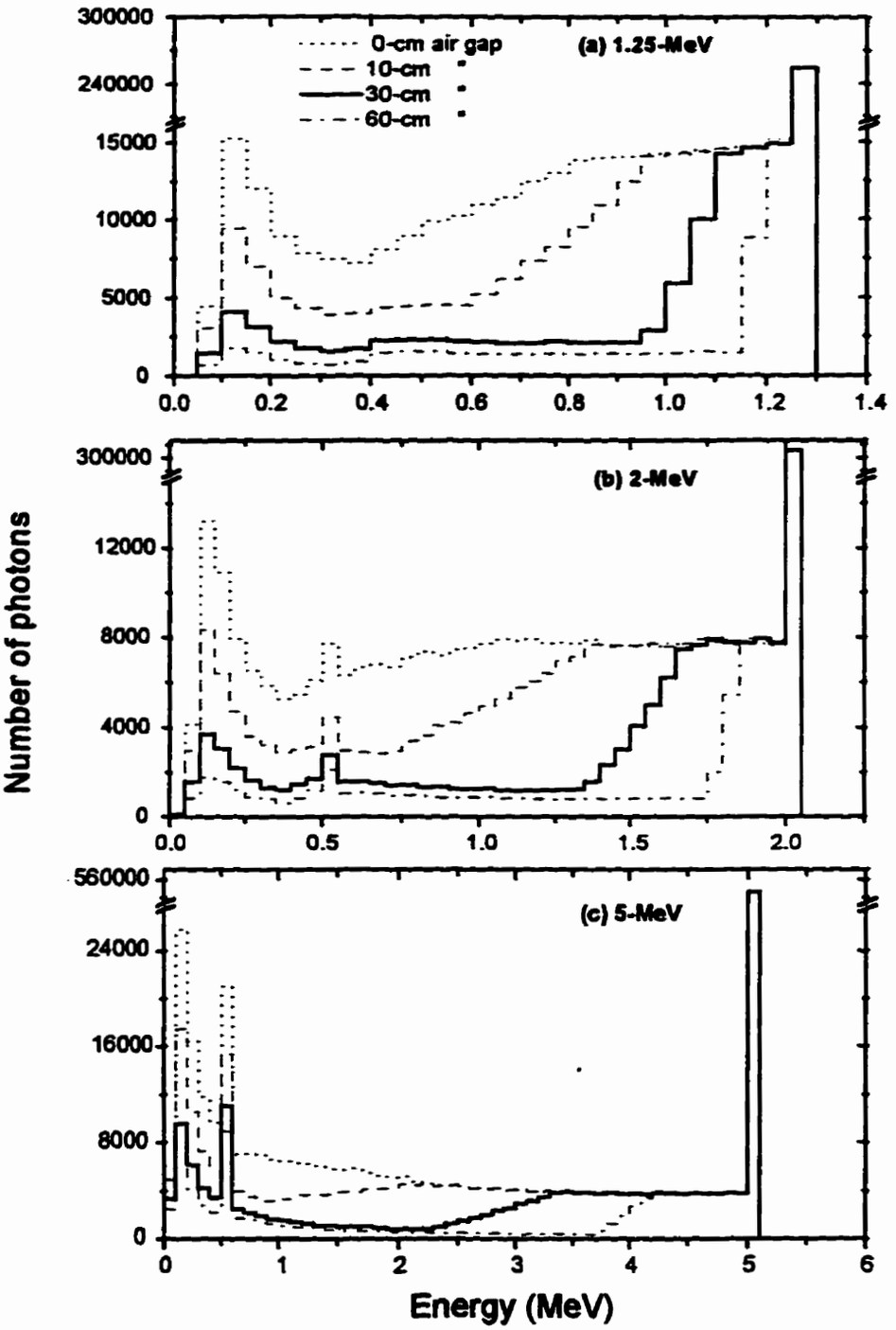

Figure 3-2 Energy spectrum at the copper-phosphor interface of the portal imaging detector as a function of air gap for 20-cm phantom/slab thickness and a 30 x 30 cm^2 field size. (a) 1.25-MeV, (b) 2-MeV, and (c) 5-MeV incident beams.

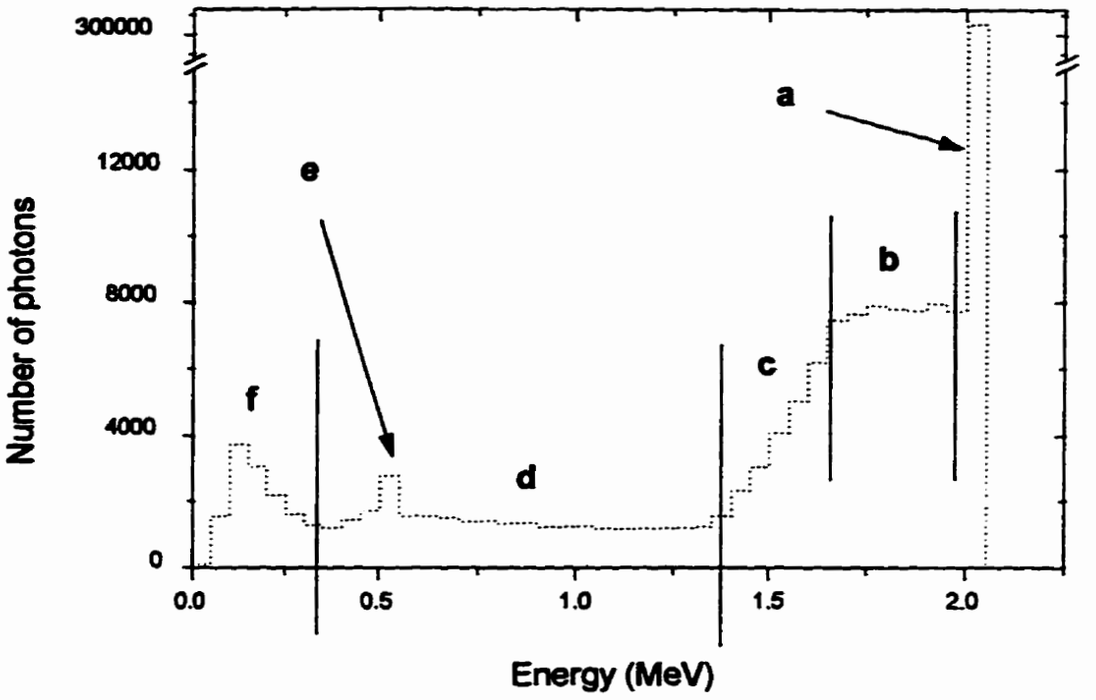

Figure 3-3. The spectrum of exit photon beams under various conditions has the same general shape. Six distinct regions can be identified in this general spectrum. These comprise (from right to left) the primary component designated by region a, the high energy scattered component (region b), and the intermediate-to-high energy transitional zone (region c). The remaining sections include the scattered photons of intermediate energies (region d), on whose spectrum is superimposed a narrow peak at energies of between 0.5 and 0.6 MeV (region e), and finally, a broad low energy peak designated by region f. These annotations have been used in the remaining sections of this chapter.

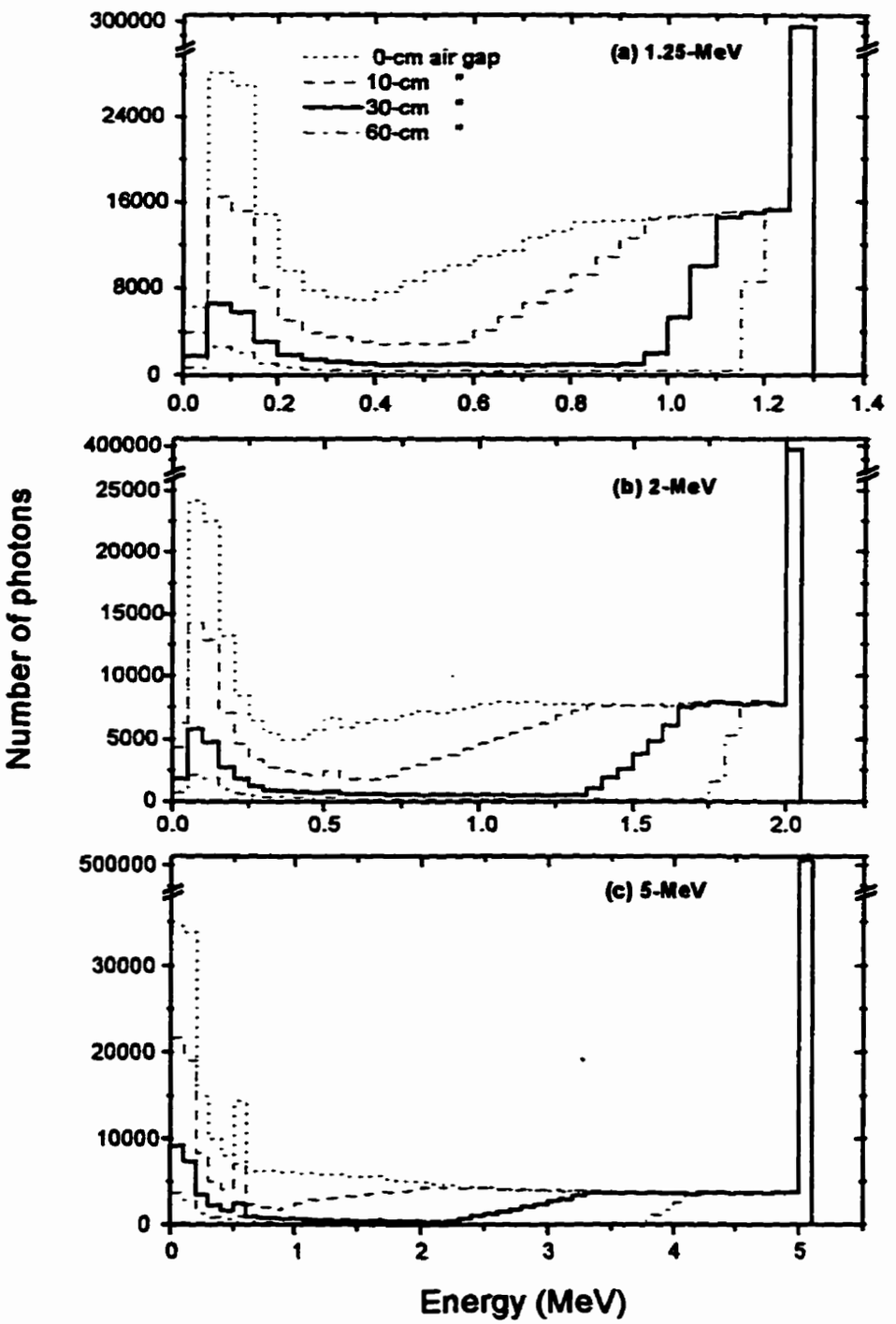

Figure 3-4. Energy spectrum at the copper surface entrance of the portal imaging detector as a function of air gap for 20-cm phantom/slab thickness and a 30 x 30 cm^2 field size. (a) 1.25-MeV, (b) 2-MeV, and (c) 5-MeV incident beams.

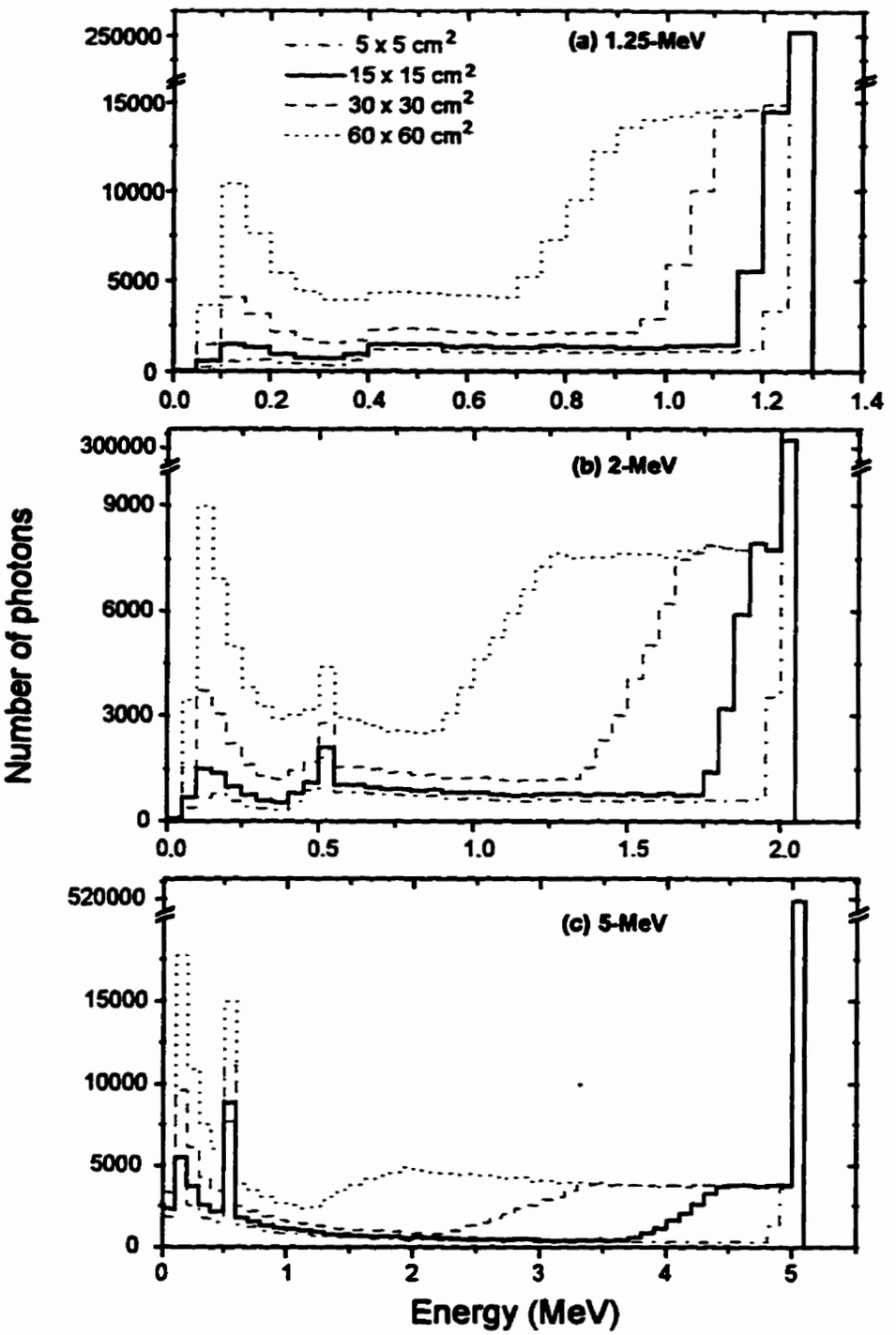

Figure 3-5. Field size dependence of the energy spectrum at the copper-phosphor interface of the portal imaging detector for a 20-cm phantom thickness and a 30-cm air gap.

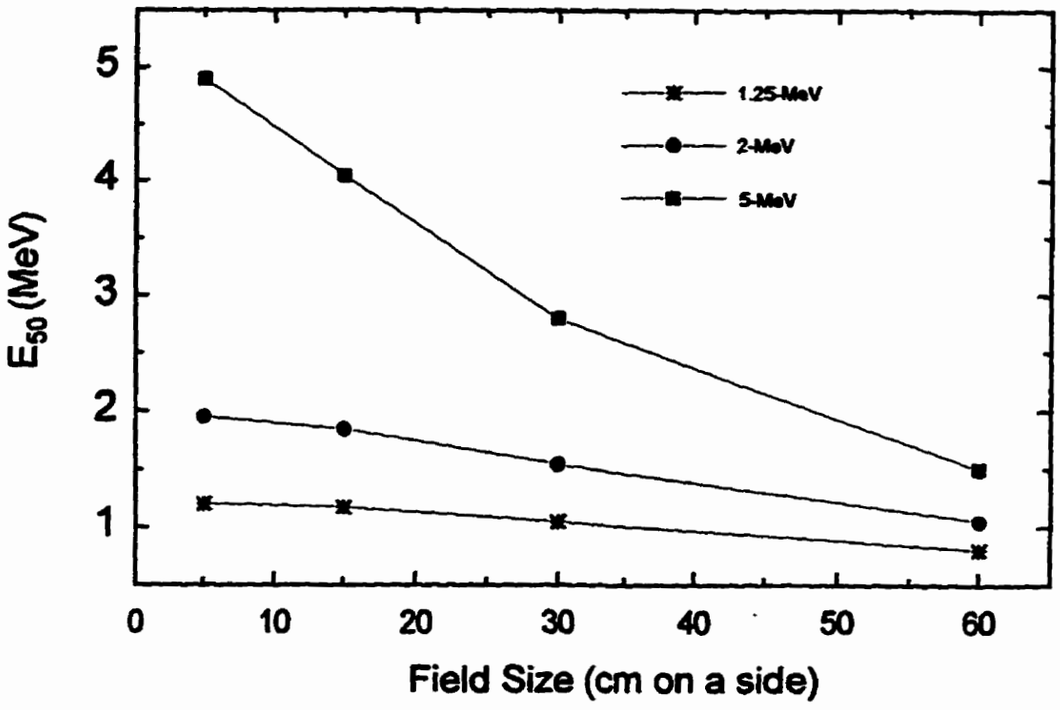

Figure 3-6. The variation of E_{50} (i.e. energy at the point on the spectrum corresponding to 50% transition from high to intermediate energies) with field size and energy. Geometry: 20-cm thick phantom, 30-cm air gap.

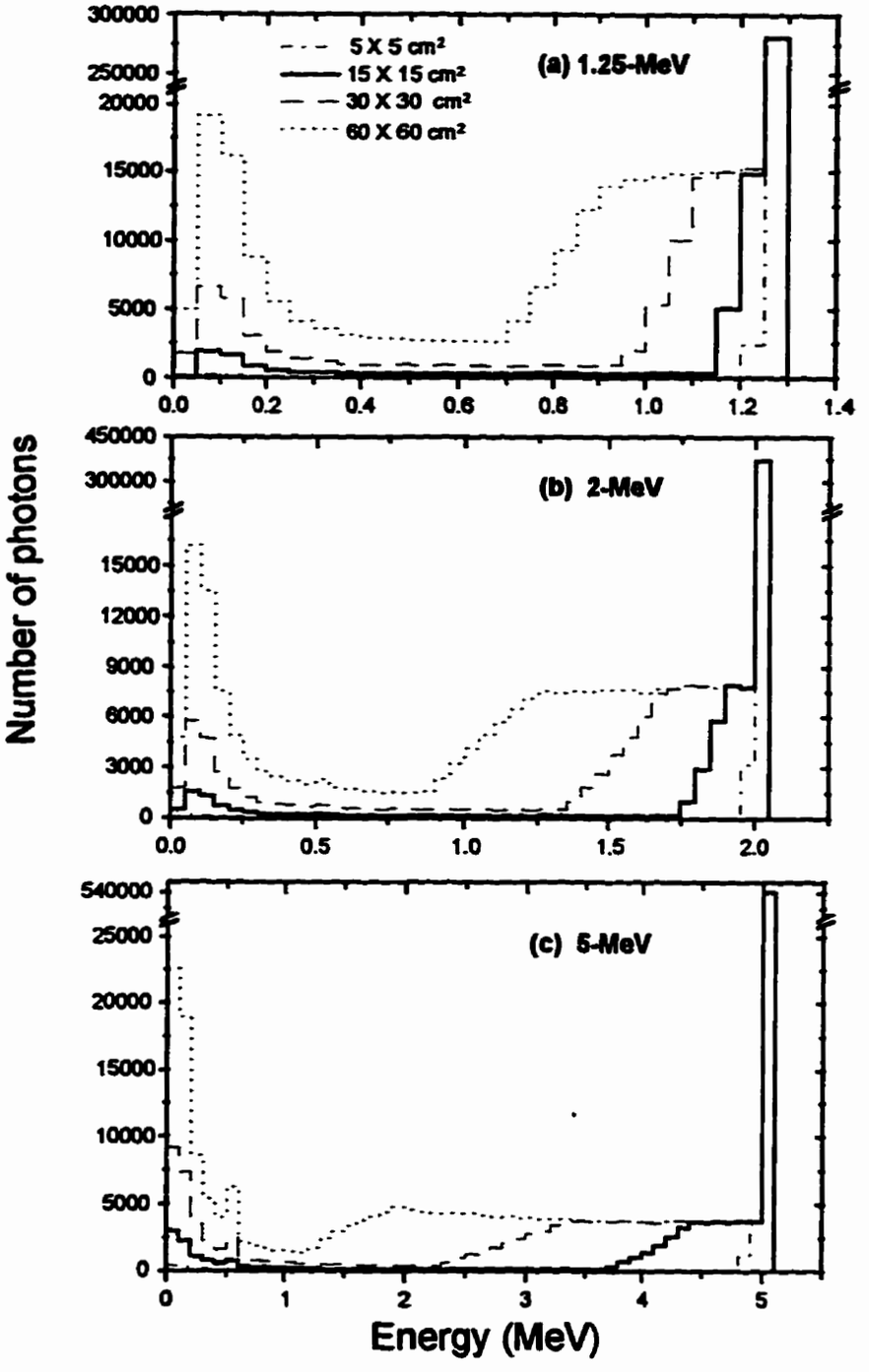

Figure 3-7. Field size dependence of the energy spectrum at the copper surface entrance of the portal imaging detector for a 20-cm phantom thickness and a 30-cm air gap.

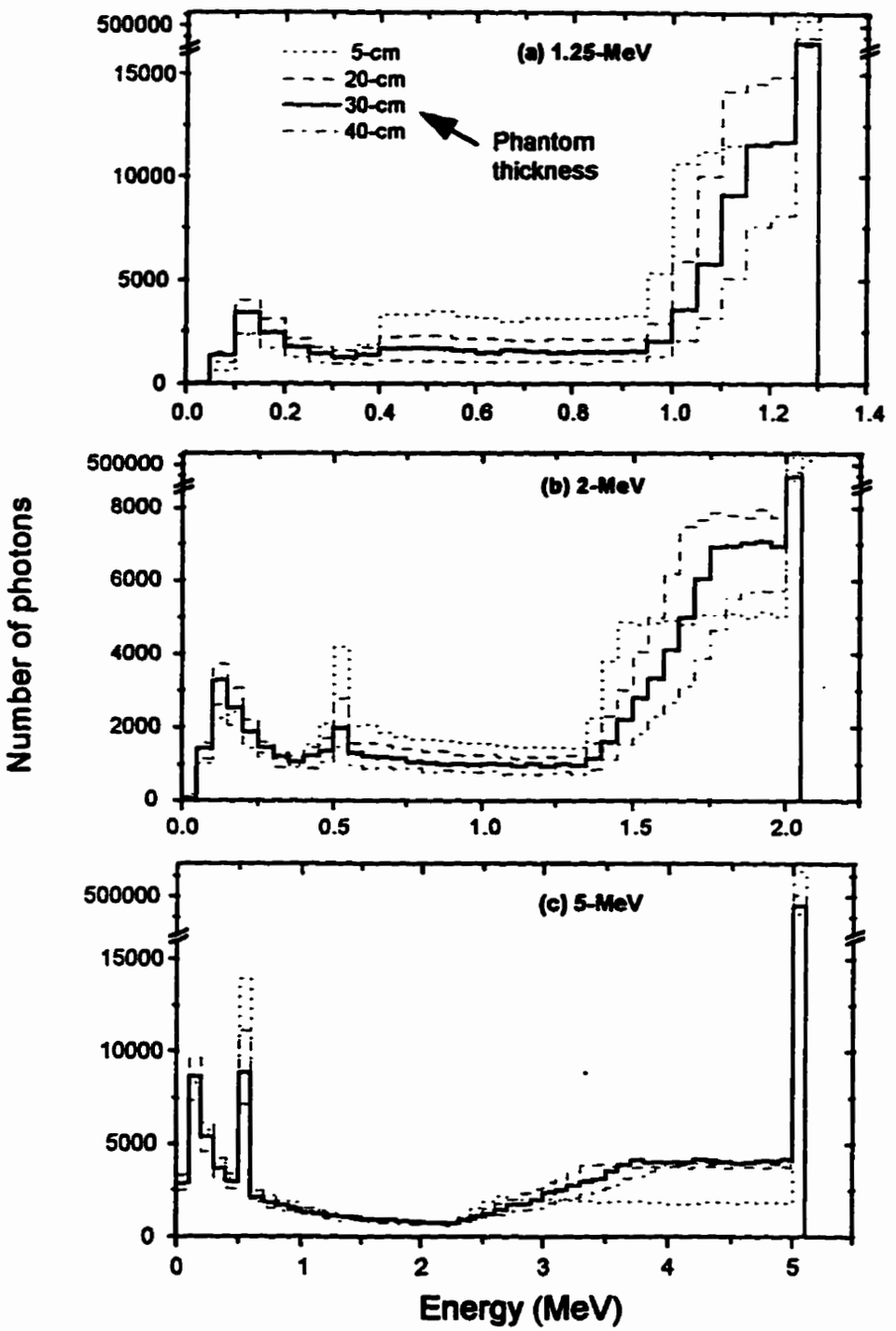

Figure 3-8. Spectral distribution of exit photon beams reaching the copper-phosphor interface of the portal imaging detector for an air gap thickness of 30-cm and a field size of 30 x 30 cm^2. Results for various phantom thicknesses (5, 20, 30 and 40 cm) are compared.

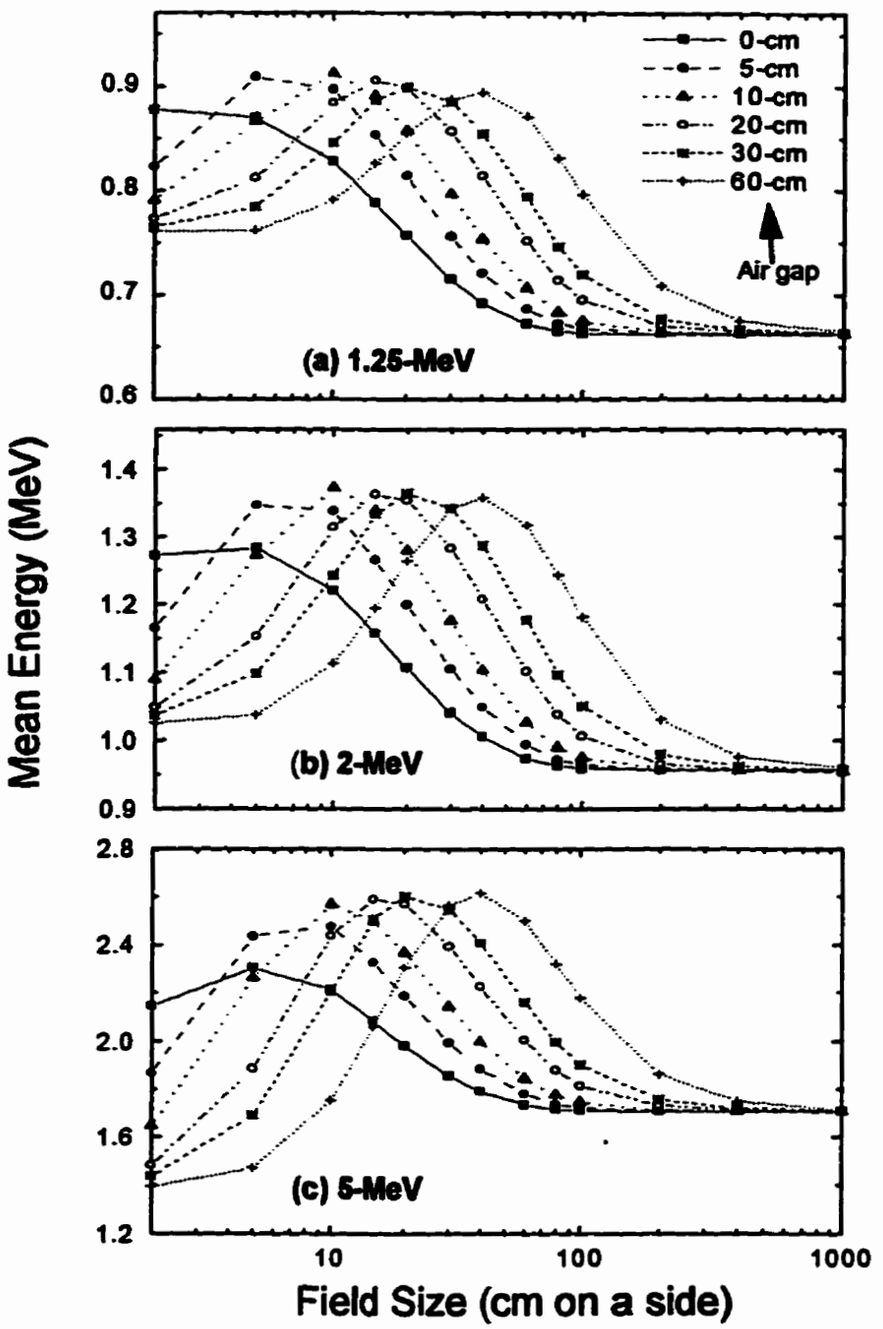

Figure 3-9. The mean energy of the scattered photons reaching the copper-phosphor interface of the detector as a function of field size and air gap for a 20-cm thick phantom.

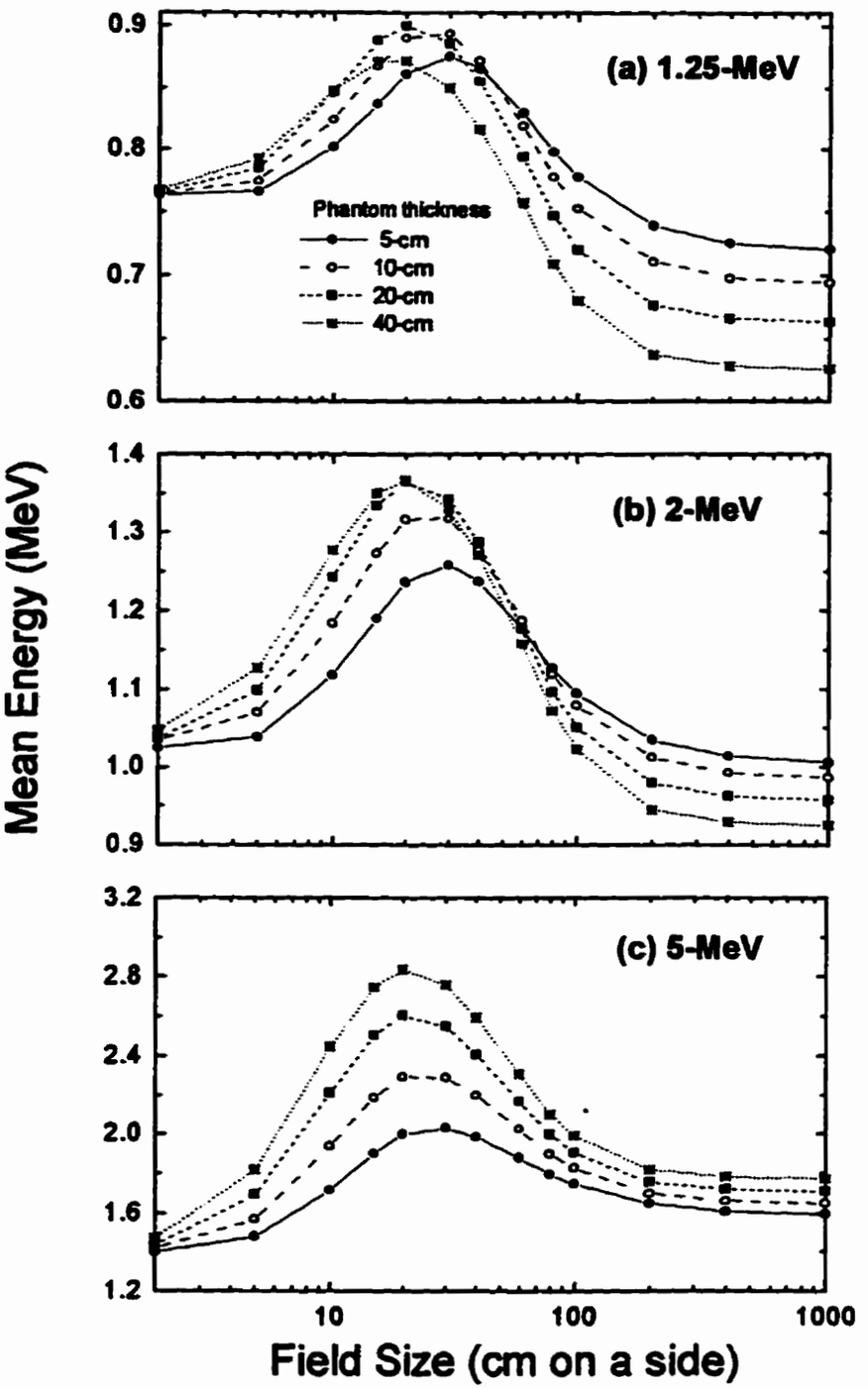

Figure 3-10. The mean energy of scattered photons reaching the copper-phosphor interface of detector as a function of field size and phantom thickness after passing through a 30-cm air gap.

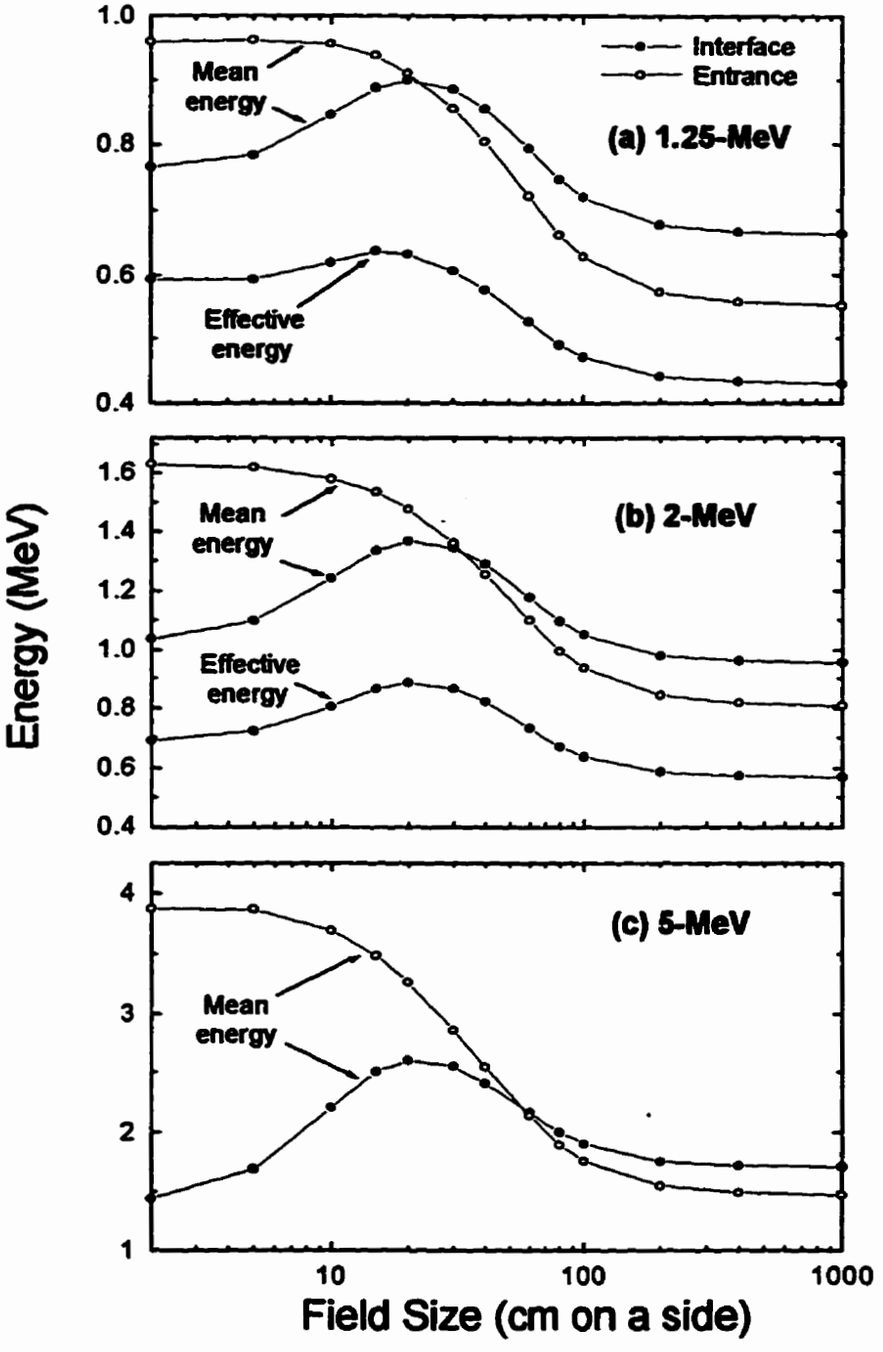

Figure 3-11. Comparison of the mean and effective energies of scattered photons at the copper-phosphor interface with each other and with the mean energy at the copper surface entrance. The data shown is for a 20-cm phantom thickness and a 30-cm air gap.

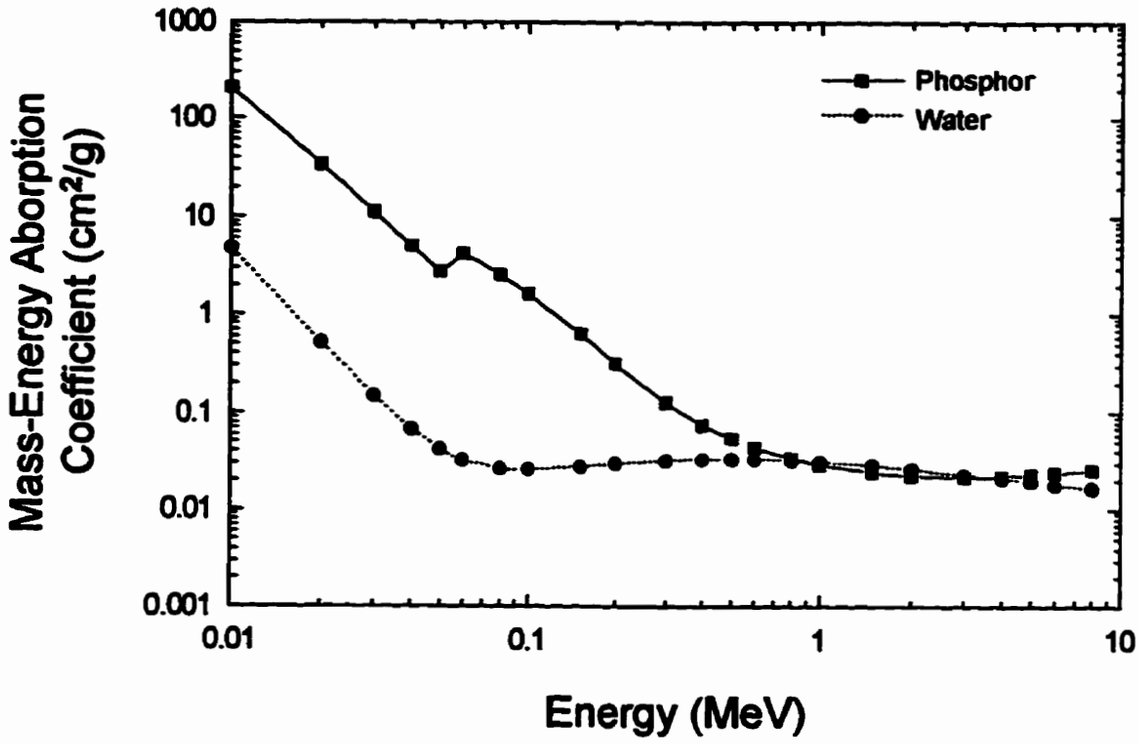

Figure 3-12. Dependence of mass energy absorption coefficient (μ_{ab}/ρ) on energy. Data, adapted from Storm and Israel,[14] for the gadolinium oxysulfide phosphor are compared with those for water.

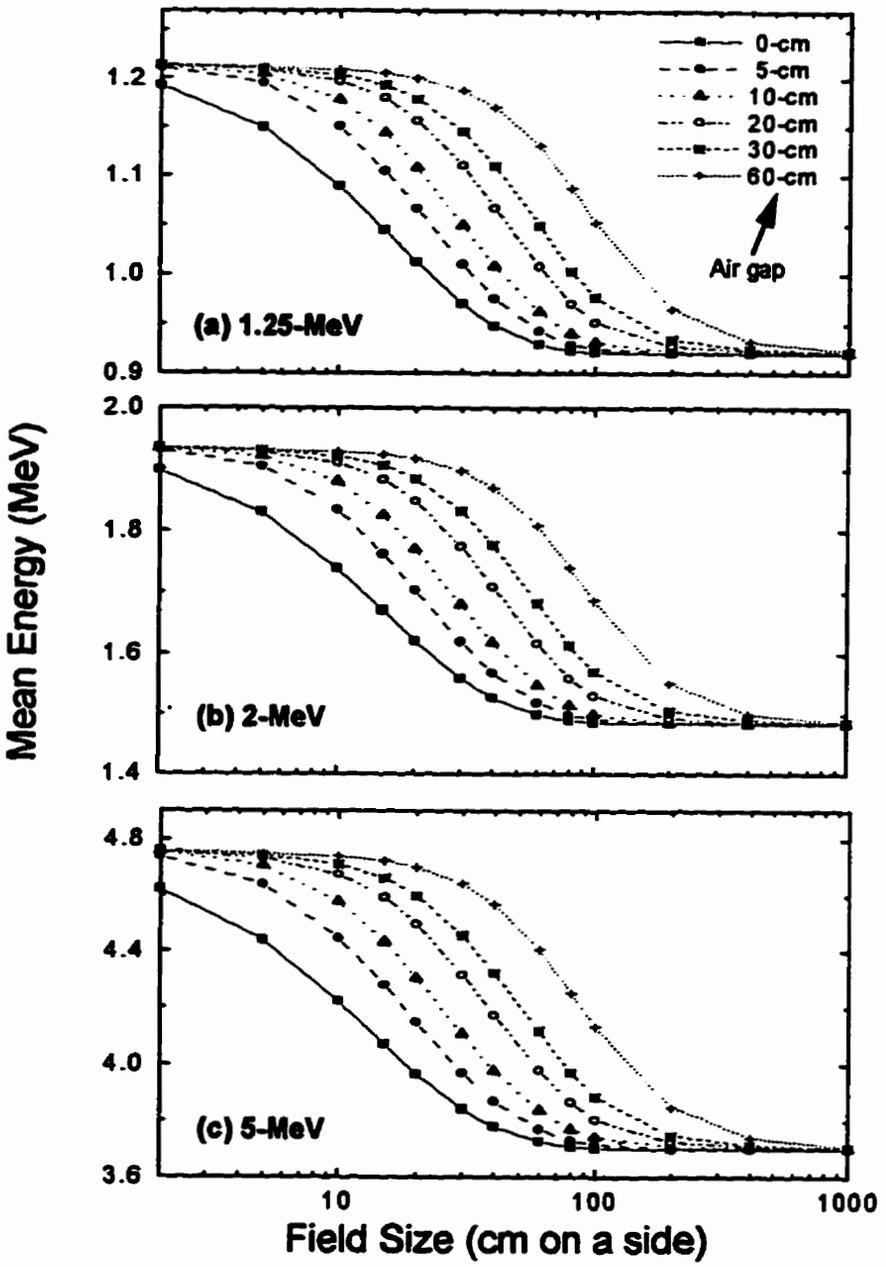

Figure 3-13. Mean energy of the photon beam (primary plus scattered components) at the copper-phosphor interface as a function of field size. Results are shown for a 20-cm thick phantom and air gaps of 0, 5, 10, 20, 30, and 60 cm.

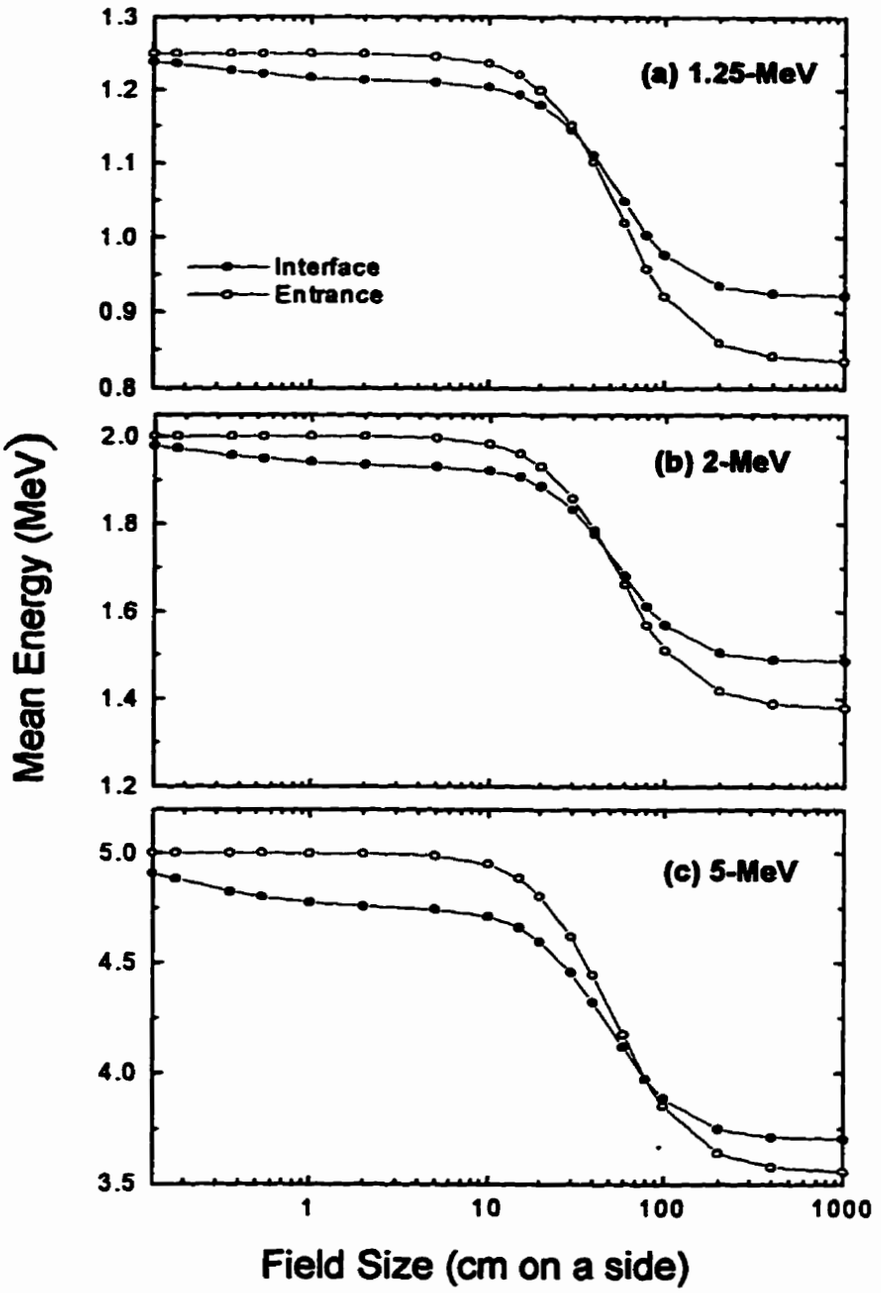

Figure 3-14. The mean energy of the photon beam (primary plus scattered components) at the copper-phosphor interface compared with that at the copper surface entrance. Geometry: 20-cm thick phantom, 30-cm air gap.

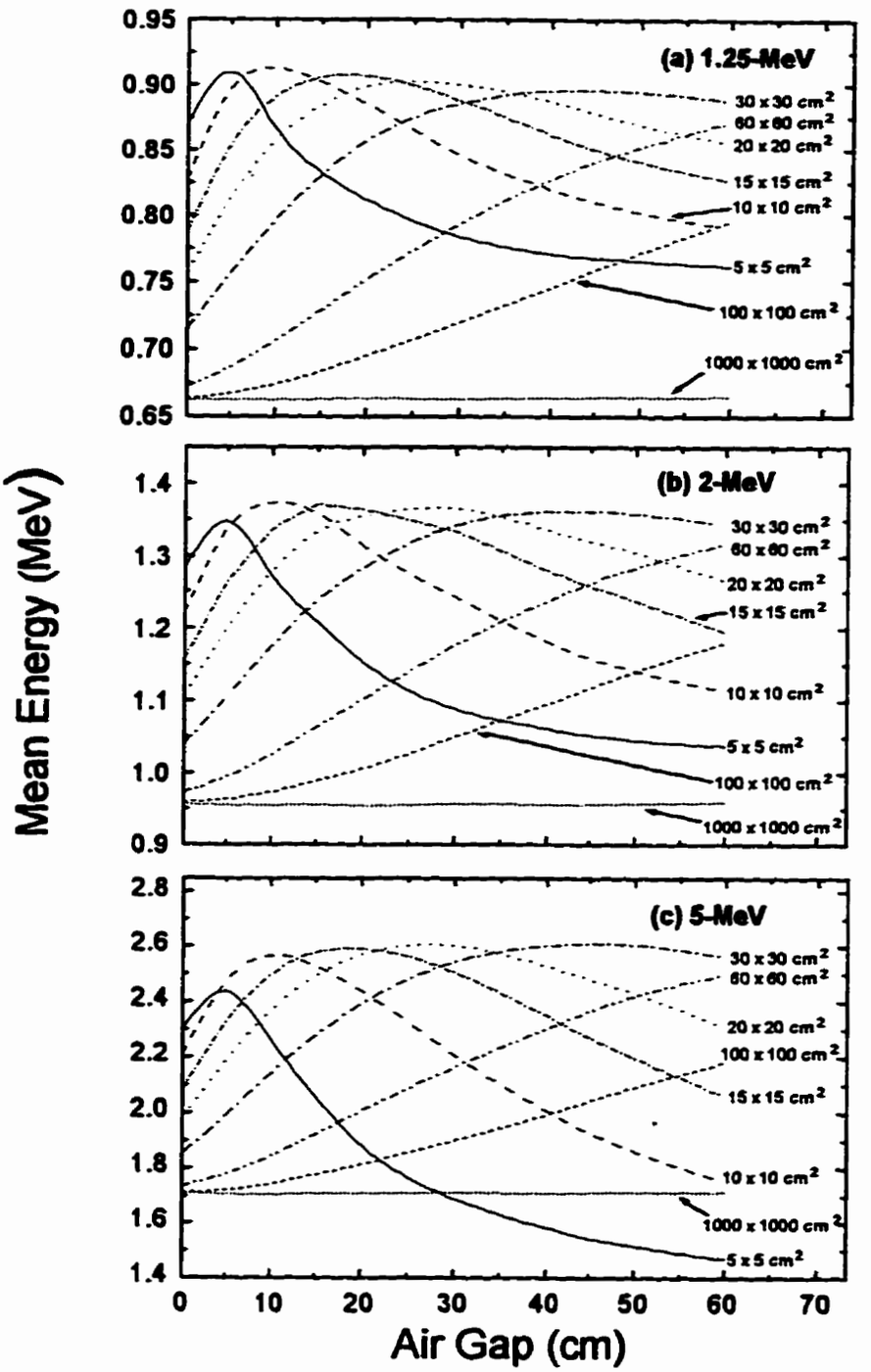

Figure 3-15. Air gap dependence of mean energy of the scattered photons reaching the copper-phosphor interface of the detector. Results are shown for a phantom thickness of 20-cm and a series of field sizes.

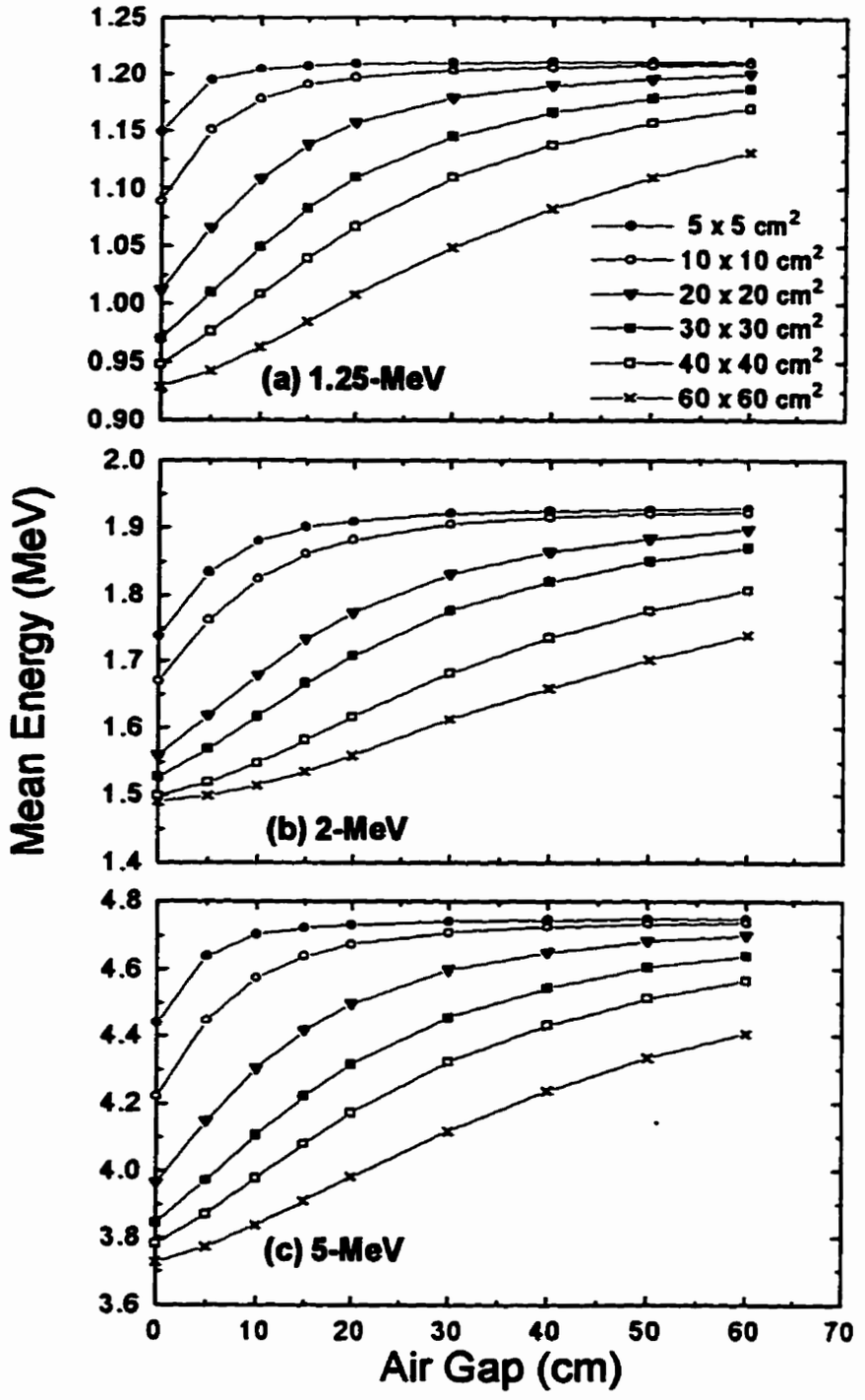

Figure 3-16. Mean energy of the photon beam (primary plus scatter) at the copper-phosphor interface as a function of air gap for 20-cm thick phantom. Data for 5 x 5, 10 x 10, 20 x 20, 30 x 30, 40 x 40, and 60 x 60 cm^2 fields are shown.

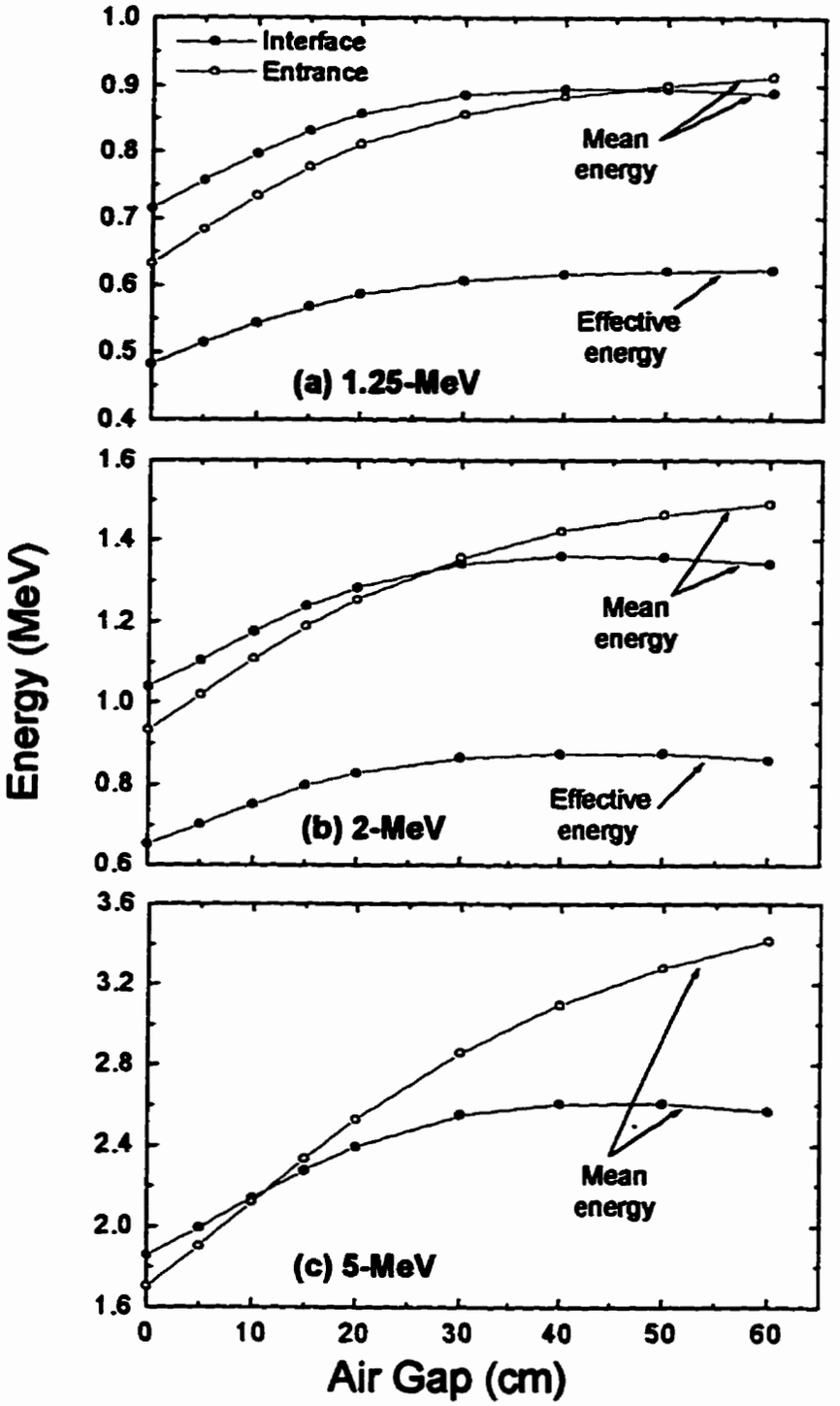

Figure 3-17. The mean and effective energies of the scattered component of the beam at the detector interface are compared with those at the entrance. Data reported are for a 20-cm thick phantom and 30 x 30 cm^2 field.

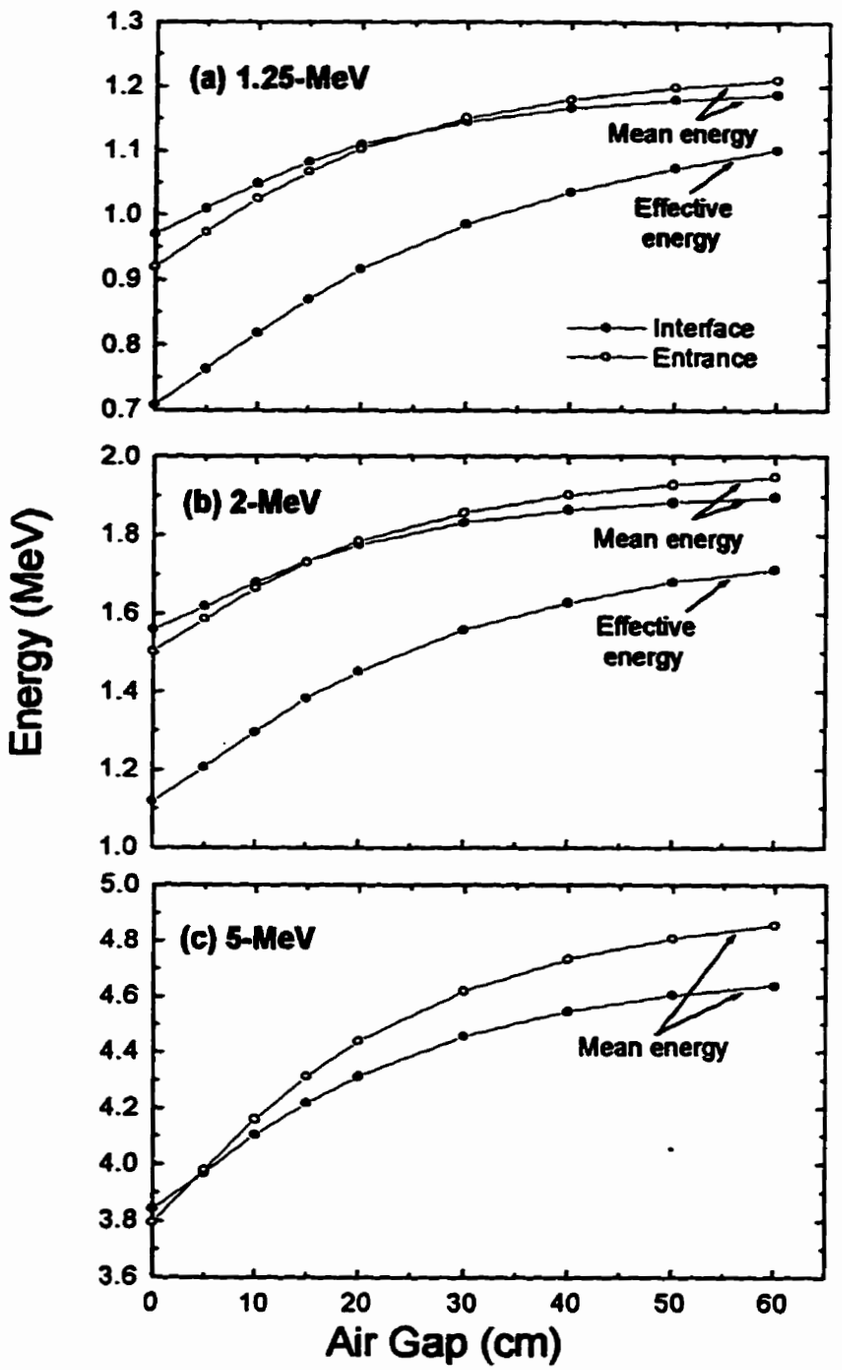

Figure 3-18. Comparison of the mean and effective energies of the photon beam (primary plus scatter) at the copper-phosphor interface with those at the copper surface entrance. A phantom thickness of 20-cm and a field size of 30 x 30 cm^2 were simulated.

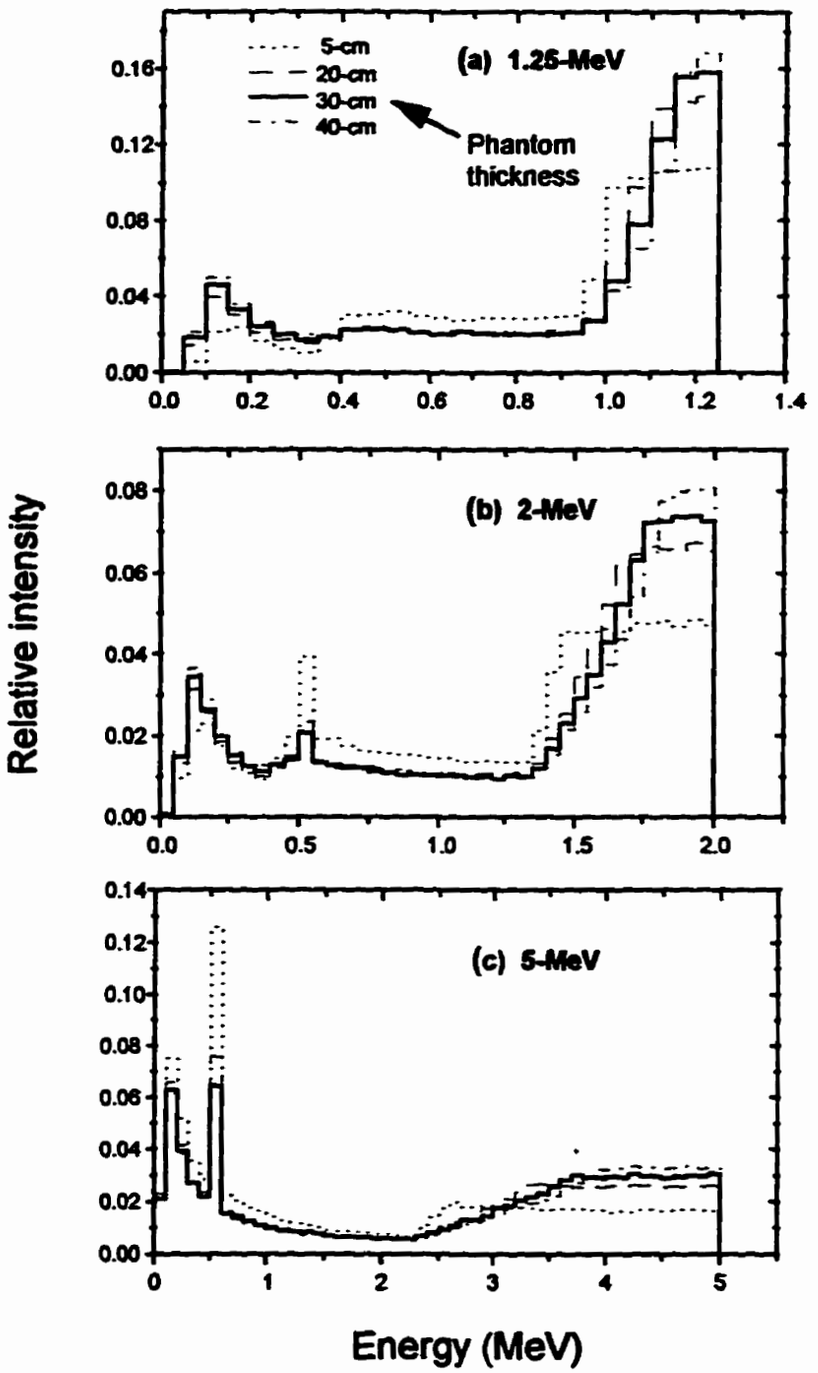

Figure 3-19. Normalized spectrum of scattered photons reaching the copper-phosphor interface of detector for an air gap thickness of 30-cm and a field size of 30 x 30 cm^2. The area under each unnormalized spectrum of the scattered photons (figure 3-4) was used as the normalization factor to allow comparison of spectra for different phantom thicknesses (5, 20, 30 and 40 cm).

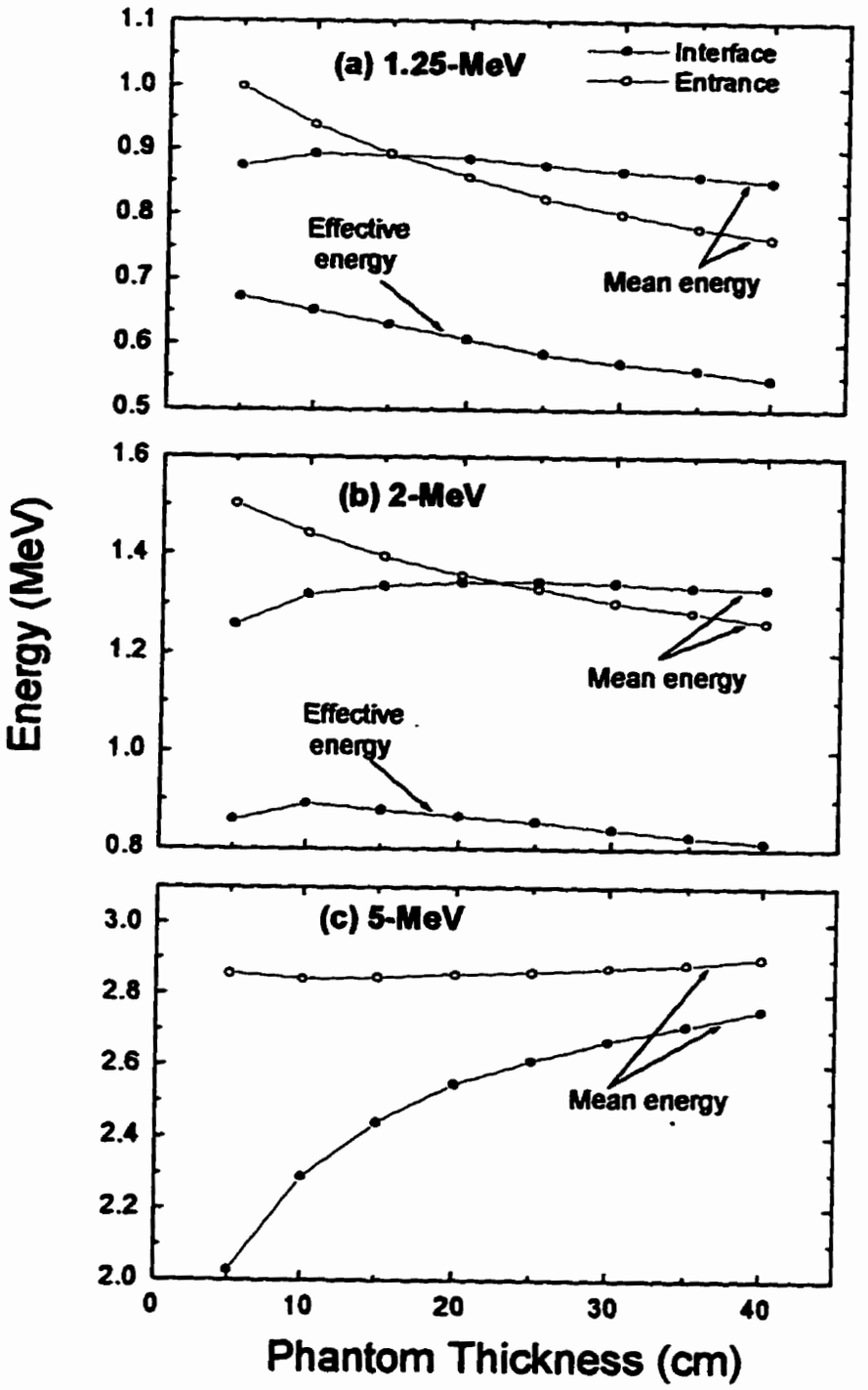

Figure 3-20. The mean and effective energies of the scattered component of the beam at the detector interface are compared with those at the entrance. Data reported here are for a 30 x 30 cm^2 field and 30-cm air gap.

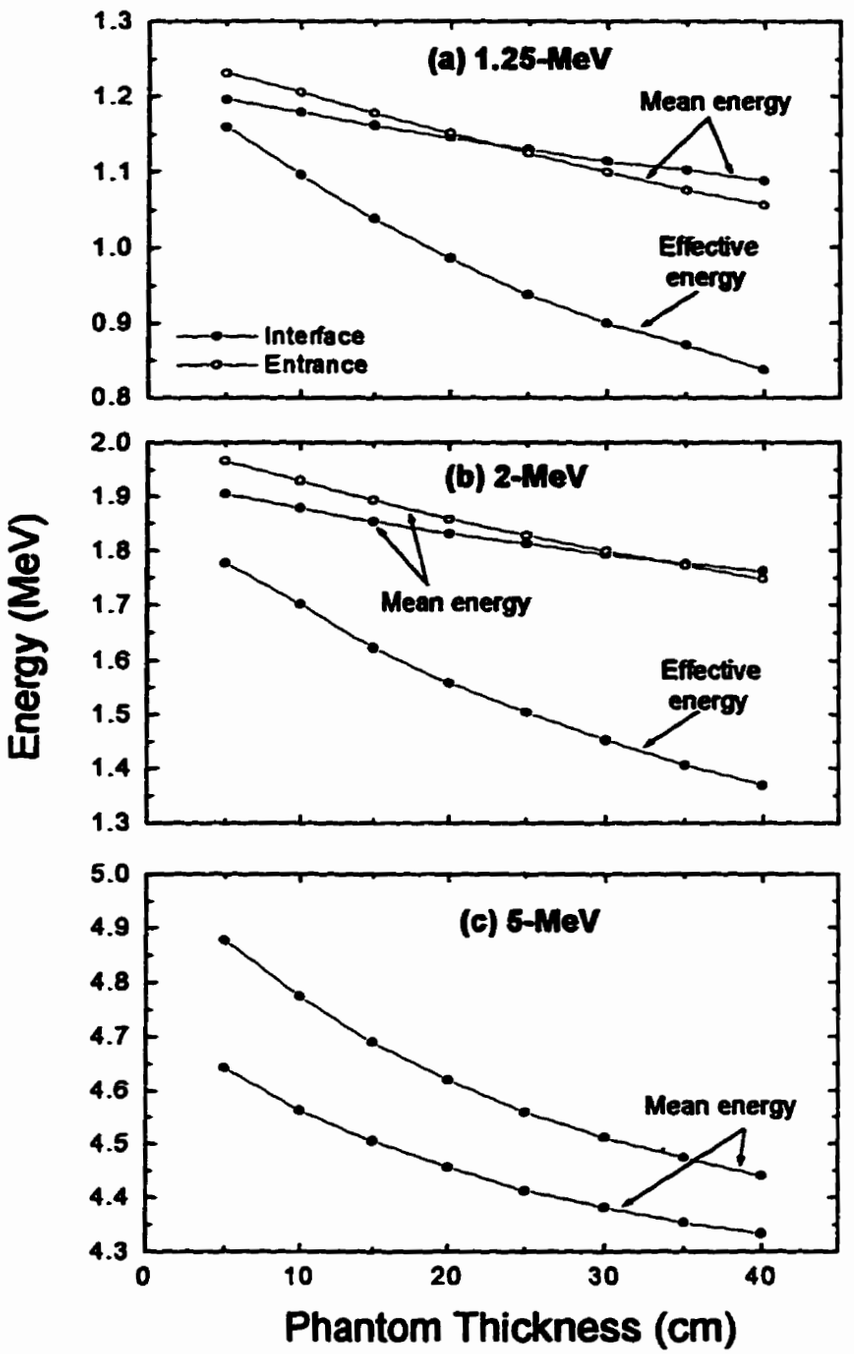

Figure 3-21. The mean energy of the photon beam (primary plus scatter) reaching the copper surface entrance and the mean and effective energies at the copper-phosphor interface are compared with each other. The beam of field size 30 x 30 cm^2 was allowed to traverse an air gap of 30-cm.

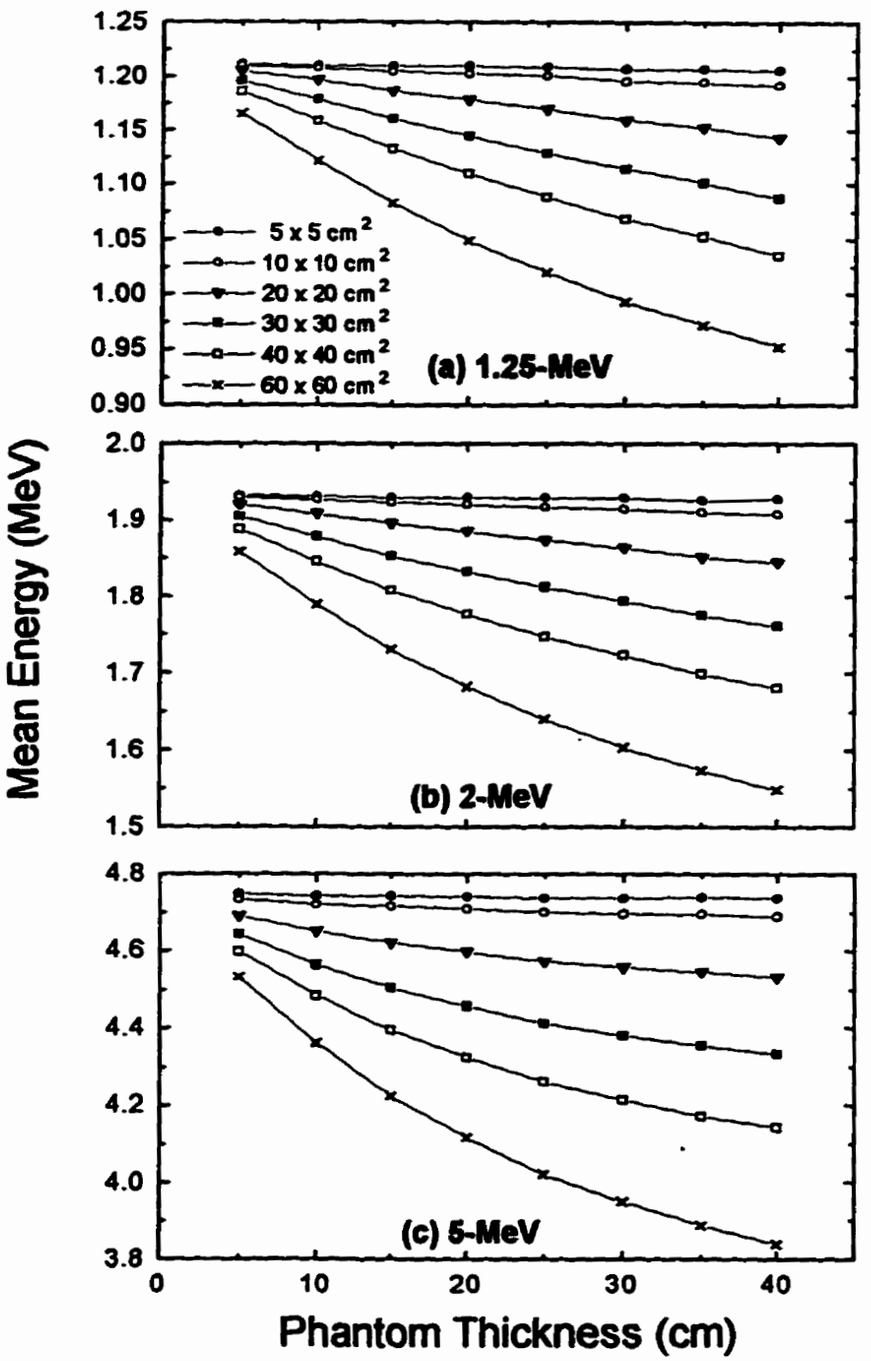

Figure 3-22. Dependence of mean energy of the photon beam (primary plus scatter) reaching the copper-phosphor interface on phantom thickness. Results for a number of field sizes and an air gap of 30-cm are compared.

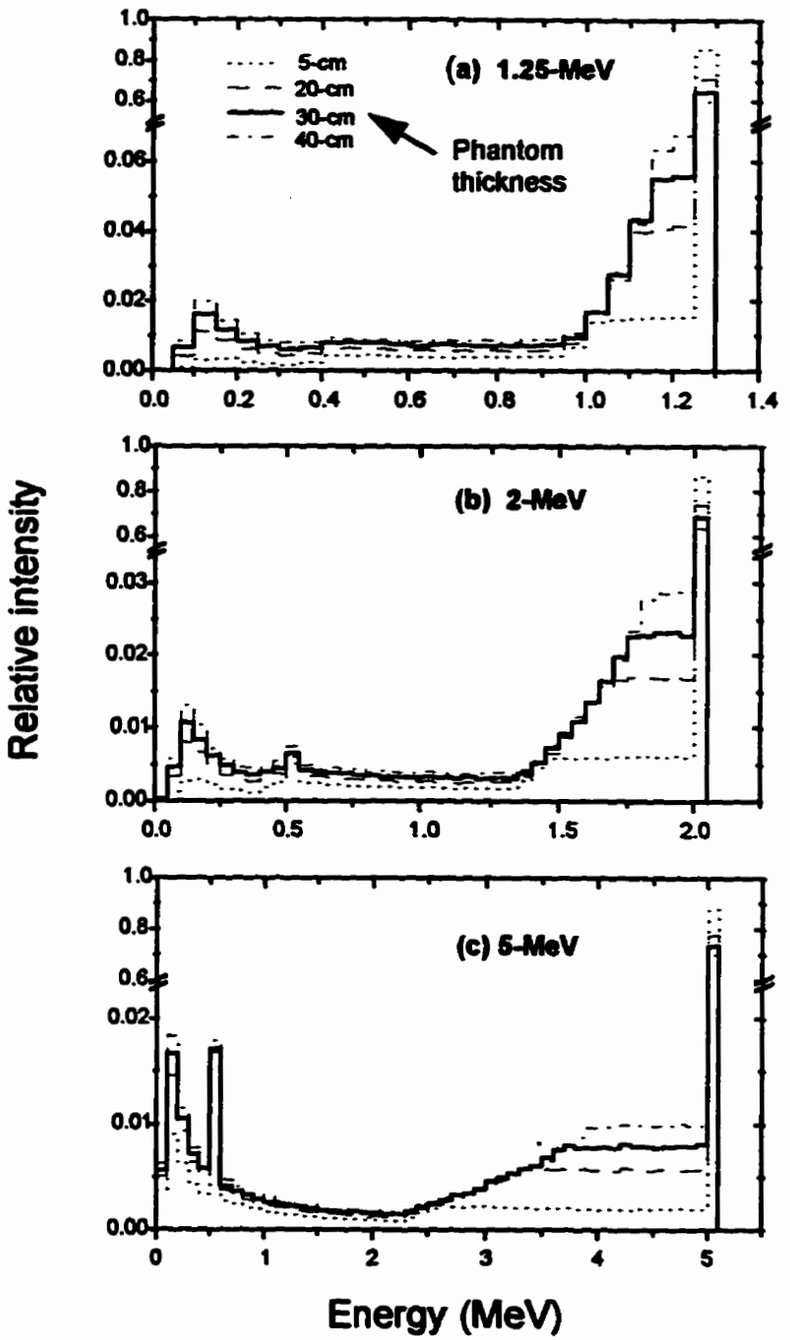

Figure 3-23. Normalized spectrum of photon beams (primary plus scatter) reaching the copper-phosphor interface of detector for an air gap thickness of 30-cm and a field size of 30 x 30 cm^2. The area under each unnormalized spectrum (refer to figure 3-4) was used as the normalization factor to allow comparison of spectra for different phantom thicknesses (5, 20, 30 and 40 cm).

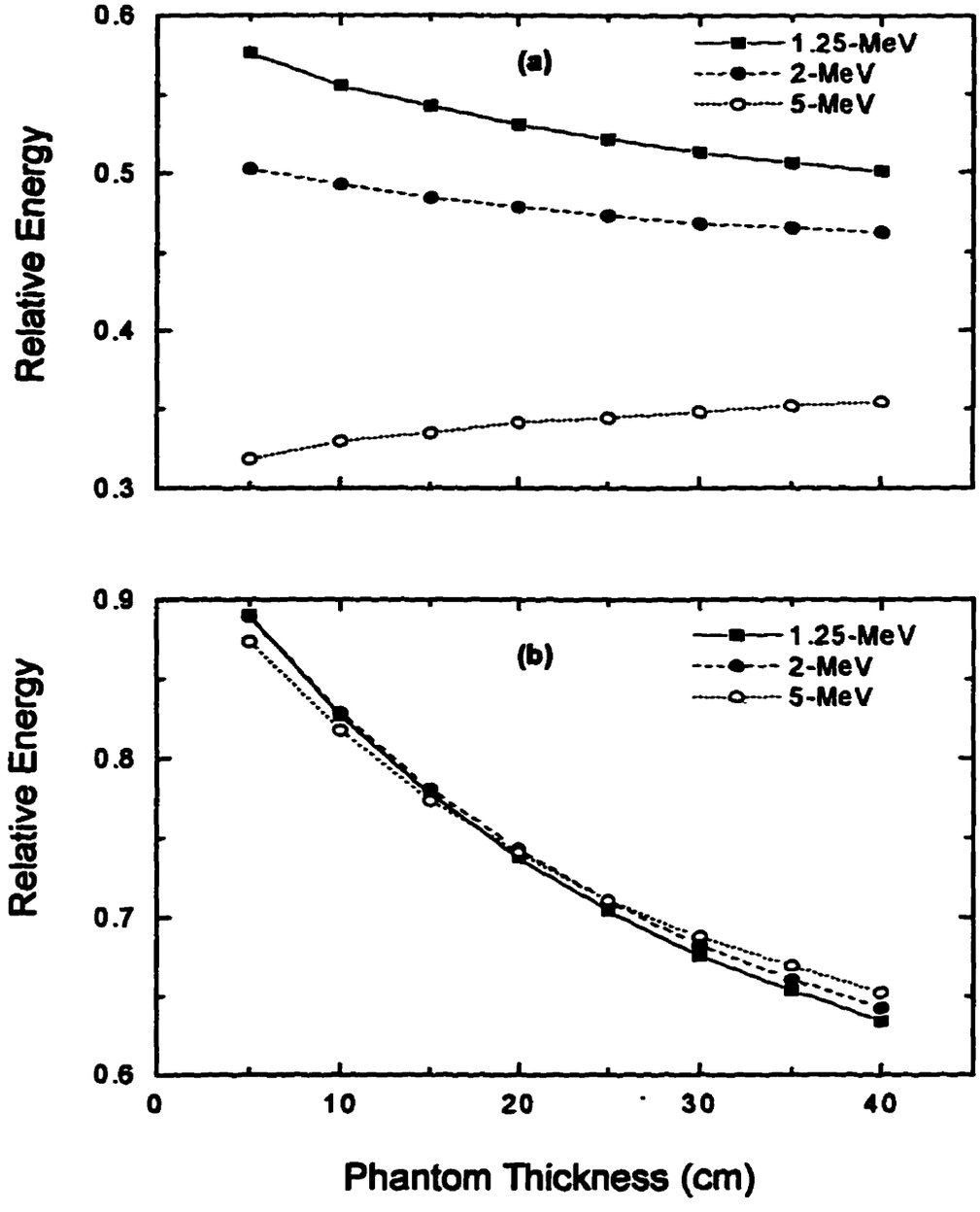

Figure 3-24. In the limit of large field sizes, the mean energy of the scattered as well as the entire beam of photons at the detector interface approaches an asymptotic value. This value relative to the incident primary energy is shown as a function of phantom thickness for 1.25-, 2-, and 5-MeV monoenergetic incident beams. (a) Scattered component of beam. (b) Entire beam.

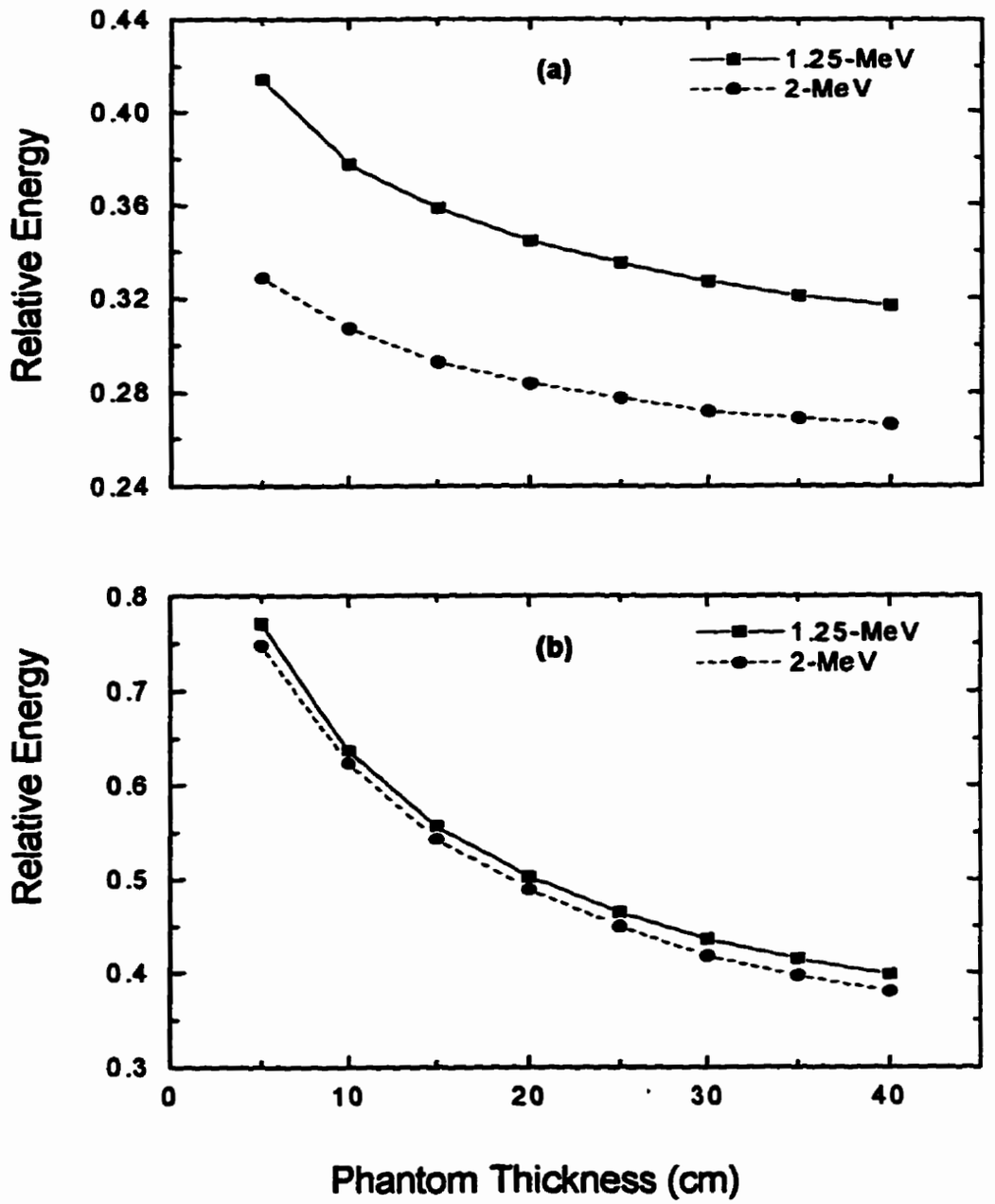

Figure 3-25. For infinitely large field sizes the effective energy of photon beams reaching the detector interface approaches an asymptotic limit. The ratio of this limit to the incident primary energy is shown as a function of phantom thickness. Results for 1.25- and 2-MeV monoenergetic incident beams are compared. (a) Scattered component of beam. (b) Entire beam.

Chapter 4

Exit dosimetry

4.1 Introduction

The use of an electronic portal imaging device (EPID) to monitor patient dose during irradiation has been proposed by a number of authors.[1-15] One way of accomplishing this is to compare exit doses measured with an EPID during treatment with portal dose images calculated during treatment planning. The development of this technique is, however, limited by the inability of the current dose calculation algorithms[16-26] to accurately calculate exit doses.[27-29] These algorithms do not properly model the air gap (between the distal surface of patient and the detector), and/or the backscatter at the detector nor do they accurately consider the high atomic number materials present in a metal-phosphor detector. In addition, the use of the current algorithms requires precalculated or premeasured input data which are usually generated in water or water equivalent materials. As such, exit doses to the non-water equivalent metal-phosphor detectors[30-32] calculated using these techniques may not be a true representation of the actual dose that was deposited since none of the existing algorithms account for dose perturbations due to changes in atomic composition.[21]

In order to improve the existing algorithms to enable them to accurately calculate the dose to a high atomic number metal-phosphor detector, it is essential that we obtain a sound

understanding of how the various factors influence this dose. Analysis of the spectral characteristics of exit photon beams carried out in chapter 3 showed that the energy spectrum, and the mean and effective energies of the beam reaching the detector are significantly affected by the patient/detector geometry as well as the detector material. These spectral changes are expected to translate into significant dose perturbations in the detector since metal-phosphor detectors have non-linear response. Although a number of studies[1-15] have provided useful information on portal imaging dosimetry, they do not address most of the problems in question. The aim of this chapter is to investigate the influence of the patient/detector geometry and the detector material on the dose to the detector. This study, which was performed using Monte Carlo techniques, has provided an understanding of the various factors and their impact on the dose to a metal-phosphor portal imaging detector.

4.2 Materials and Methods

4.2.1 Monte Carlo simulations of monoenergetic photon beams

As in the investigation of the spectral characteristics in chapter 3, this study employs the EGS4[33] Monte Carlo simulation code in conjunction with the user code called INHOM[33-35] to simulate monoenergetic incident beams of photons in homogeneous slab phantom geometries. The cutoff energies of photons and electrons were set as follows: PCUT = AP = 10 keV and ECUT = AE = 561 keV as was discussed in section 3.3.1.

The simulation geometry, depicted in figure 3-1, has been discussed in chapter 3. This parallel beam geometry was employed for the simulations to make it possible to reduce the calculation time and to improve the statistics of the results through the application of the reciprocity theorem (see section 3.3). While this theorem is not directly applicable to a diverging beam geometry (i.e. figure 4-1), it is possible to apply it to a parallel beam geometry (i.e. infinite SSD) and to convert the results to those of a diverging beam (finite SSD) using a standard technique.[36]

Suppose the distance from the radiation source to phantom surface (SSD) is represented by f, and the detector is located at depth d from the incident surface of the phantom. We denote the central-axis dose in the detector (more correctly in the phosphor) due to the primary photons by P_{EPI} and that due to the scattered photons by S_{EPI}, given that the projected field size in the detector plane is $s \times s$. The total dose deposited in the detector, on the central-axis, is then given by

$$D_{EPI} = P_{EPI} + S_{EPI} \qquad (4\text{-}1)$$

The quantity defined by equation (4-1) will be referred to as the exit dose.

If D_{max} represents the dose maximum in a water phantom measured at the same distance from the source as D_{EPI}, where the projected size of the field is $s \times s$, then the exit dose to maximum dose ratio (i.e. exit-maximum ratio, EMR) is defined as

$$\text{EMR} = D_{EPI} / D_{max} \qquad (4\text{-}2),$$

and the percentage exit dose (PED) by

$$PED = 100 \cdot EMR \qquad (4\text{-}3).$$

One notes that the definition of EMR, given by equation (4-2), is analogous to that of tissue-maximum-ratio.

In this chapter, the exit dose and the percentage exit dose (PED) are studied. Using the user-code, INHOM, exit doses and PEDs were scored as a function of field size, air gap, phantom thickness, and incident beam quality.

4.2.2 Influence of detector material

Dose calculation algorithms are designed to calculate the dose to water and/or water equivalent media. To obtain an insight into typical errors that may occur if the changes in atomic composition are not accounted for when these algorithms are used to calculate the dose to the non-water equivalent, high atomic number metal-phosphor detector, exit doses calculated in various detector materials were compared to each other. These included copper-phosphor, copper-water, water-water, and water-phosphor detectors, all of which were of the same radiological thicknesses.

4.3 Results and discussion

4.3.1 Validity of the reciprocity theorem

To ensure that the application of the reciprocity theorem in simulating a parallel beam and conversion of the resulting data from infinite to finite SSD provides the expected data (i.e. diverging beam data), results of simulations carried out using this approach were compared to those performed directly with a diverging beam. Using monoenergetic 1.25-MeV incident beams and 20-cm thick phantom, PEDs were scored as a function of air gap for 30 x 30 cm^2 field size, and as a function of field size for 30-cm air gap. As shown in figure 4-2, there is good agreement between the two sets of PED data within the limits of experimental uncertainties. The error bars indicate one standard deviation. No errors are explicitly shown for the corrected parallel beam data as the errors are less than the size of the data points. An improvement in the statistics of the data achieved through the use of the reciprocity theorem is clearly apparent. For the direct diverging beam simulations, it took over 2 hours to obtain a single data point, whereas a single simulation carried out through the reciprocity theorem route generated all data points (for a given air gap and phantom thickness) in about 45 minutes. There is therefore a tremendous saving of CPU time if the latter approach is used.

4.3.2 Dependence of percentage exit dose on field size

The dependence of PED on field size was investigated using a 20-cm thick phantom along with a given air gap. The field sizes were specified at a distance of 100-cm from the

source and were varied from 2 x 2 to 60 x 60 cm^2. Although square field sizes are reported in this section, the simulations employed circular fields of equivalent areas since the incident beams modeled had cylindrical symmetry. In figure 4-3, the change in PED with field size is shown for 0, 5, 10, 20, 30, 40, and 60-cm air gaps. For small air gaps the PED follows the shape normally associated with the increase of scatter in phantom. That is, there is an initial rapid increase with the rate of increase becoming less as the field size increases. For large air gaps, however, the initial increase of the PED is more gradual. The increase in the PED with field size is caused by the buildup of the scatter fluence with increasing field size. While the primary fluence does not depend on field size, the scatter fluence increases with field size and approaches an asymptotic maximum for large field sizes (see section 3.4.2).[30] We postulate that this maximum is independent of air gap due to the presence of radiation equilibrium (which is said to exist in a given region of a medium, if every particle of a given energy that scatters out of this region is replaced by another particle of the same type and energy) under those conditions.

In the limit of 0 x 0 cm^2 field size, the scatter fluence approaches zero and the dose deposited in the detector (on the central-axis) is due only to the primary photons. A rough estimate of this primary dose may be obtained analytically if the perturbation of dose in the phosphor resulting from the presence of the copper-phosphor interface is neglected, and the presence of electronic equilibrium in the phosphor is assumed. Using these assumptions, the PED due to the primary photons (PED_P) was calculated analytically by considering only primary attenuation in the various materials. Table 4-1 compares the analytically calculated PEDs with those generated by the Monte Carlo method for a

variety of incident energies (1.25-, 2-, and 5-MeV). For 1.25- and 2-MeV incident beams there is a discrepancy of 7% and 4%, respectively, between the analytical and the Monte Carlo data, with the former being lower in both cases. These differences are not surprising in view of the fact that the effective atomic number of the phosphor is much higher than the atomic number of copper, leading to electronic disequilibrium and dose perturbations in the vicinity of the copper-phosphor interface.[37-41] Since the forward direction of the beam is from the copper plate (lower Z) to the phosphor (higher Z) there will be dose enhancement at the interface and in a region of the phosphor immediately after the interface. This dose enhancement results from the increase in backscatter arising from the transition from copper to phosphor, and its magnitude depends on the distance of the point of calculation from the interface and the incident energy. At points far enough from the interface this effect will not be seen since there would be electronic equilibrium. While we score the average dose to the entire thickness of phosphor, this thickness (500 mg/cm^2 or 1 mm) is not large enough to render the interface effects insignificant. The Monte Carlo method accounts for these interface effects whereas the dose enhancement in the phosphor is not reflected in the analytical calculations of the PED.

As the incident energy increases, the range of electrons generated by primary photons in the copper plate and reaching the phosphor increases. At higher energies most of these electrons will have enough range to traverse the thickness of phosphor while backscatter from the phosphor will be much reduced. When this happens there will be electronic disequilibrium in the phosphor and the average dose deposited in this material will be lower than the equilibrium dose. The analytical calculations assumed the presence of

electronic equilibrium in the phosphor. As a result, the PEDs calculated analytically for higher energies will be higher than those calculated with the Monte Carlo method. This is the case for 5-MeV incident beams, where the average energy of an electron produced in the copper plate after primary photon interaction is 3.37-MeV,[42] and the corresponding CSDA range in copper is 2373-mg/cm^2.[43] The CSDA range in the phosphor (with a higher atomic number) will even be greater since the CSDA range in mass/area increases with increasing atomic number. Therefore, most of the electrons produced in the copper plate and reaching the phosphor (which is only 500-mg/cm^2 thick) will be able to traverse it even if the effect of scattering on the actual range is considered.

4.3.3 Variation of percentage exit dose with air gap

The effect of an air gap on exit doses was studied using a water phantom of thickness 20-cm, whose position relative to the source was fixed. The air gap was varied (from 0 to 60-cm) by changing the source to detector distance (SDD) as opposed to keeping the SDD constant while changing the SSD. This choice was made because it enabled us to vary the air gap without changing the area traversed by the beam in the phantom. Figure 4-4 shows the PED for 5 x 5, 10 x 10, 15 x 15, 20 x 20, 30 x 30, and 40 x 40 cm^2 field sizes. The PED (which, by definition, is not affected by changing SDD) decreases roughly exponentially as the air gap increases and asymptotically approaches the value described by narrow beam attenuation. This attenuation is more gradual for larger field sizes. The reduction of PED is attributed to the loss of radiation equilibrium in the air volume. In the phantom, some of the photons are scattered towards the central-axis of the beam at

varying angles (i.e. in-scatter) while others are scattered away from this axis in different directions (out-scatter). Both the in-scattered and the out-scattered photons emerge from the phantom at various angles, with a fraction of the former category of photons being detected on the central-axis in the detector plane. With an air gap, some of the in-scattered photons, which would otherwise have been detected, become out-scattered photons in the air gap and are not detected. This effect becomes more pronounced as the air gap increases, leading to a reduction in the PED. In the limit of infinite air gap, every in-scattered photon will eventually change its status in the air gap to become an out-scattered photon, unless the field size is infinitely large. Consequently, for infinite air gap (and finite field sizes), no scattered photons are detected on the central-axis in the detector plane. Therefore, under those conditions, the dose deposited in the detector is the primary dose (PED_p).

4.3.4 Percentage exit dose as a function of phantom thickness

In studying the dependence of PED on phantom thickness, the position of the detector relative to the source was held constant at 130-cm. The phantom thickness was varied (from 5 to 40 cm) by keeping the source to exit surface of phantom distance fixed (100-cm) while adding new material to the side closest to the radiation source. This resulted in a fixed air gap of 30-cm. In figure 4-5, the PEDs are shown for 5 x 5, 20 x 20, 30 x 30, and 40 x 40 cm^2 field sizes. As expected, the PED decreases roughly exponentially with increasing phantom thickness due mainly to the exponential attenuation of the primary component of the beam. Although the scattered component initially increases with

phantom thickness, reaches a maximum and then starts to decline (see section 3.4.3),[30] the change in primary fluence with phantom thickness is large compared to the change in scatter fluence. Consequently, the reduction in primary fluence dominates the changes introduced by scatter fluence. For larger field sizes the exponential attenuation of the PED is more gradual because the contribution of scatter is progressively larger. In the limit of large phantom thicknesses, both the intensities of the primary and the scattered components of the beam asymptotically approach zero. The PED therefore approaches zero for infinitely large phantom thicknesses. For zero phantom thickness (i.e. open beam geometry), the radiation beam is incident directly on the detector, and the PED, in this case, is the dose deposited in the detector expressed as a percentage of dose maximum at the same distance in water. The PED under open beam conditions (i.e. open beam PED, denoted by PED_{ob}) can be roughly estimated if interface effects are neglected and the presence of electronic equilibrium in the phosphor is assumed (see section 4.3.2). The open beam PED calculated based on these assumptions, with the calculations taking into account only primary attenuation, is compared with data generated with the Monte Carlo method in table 4-2. For 1.25- and 2-MeV incident beams the analytical calculations are less than the Monte calculations by 9% and 4%, respectively, whereas for 5-MeV beams the converse is true, with a discrepancy of 7%. The trend seen here is similar to that observed in section 4.3.2 and therefore does not merit any further discussion.

Since it is impossible to carry out Monte Carlo simulations for a 0 x 0 cm^2 field size, the Monte Carlo PED_{ob} data shown in the aforementioned table were generated by using a field size of 2 x 2 cm^2, where it was assumed that negligible scatter reaches the detector

for this field size. To obtain the PED_{ob} data, the Monte Carlo calculated PEDs at 2 x 2 cm^2 field size, depicted as data points in figure 4-6, were extrapolated to zero phantom thickness by least squares fitting with equations of form

$$PED = PED_{ob} \cdot \exp(-\mu d) \qquad (4\text{-}4),$$

where PED_{ob} is the percentage exit dose for zero phantom thickness and also the parameter to be determined, μ is the primary attenuation coefficient for the given incident energy, and d is the thickness of the water phantom. The fact that excellent fits are obtained for all incident energies establishes the validity of our earlier assumption of negligible scatter reaching detector for a 2 x 2 cm^2 field size.

4.3.5 Effects of the non-water equivalence of detector

In an attempt to understand the influence of the detector material and its impact on the exit dose, PEDs calculated in Cu-phosphor, Cu-water, water-water, and water-phosphor detectors were compared to each other (see figure 4-7). As expected, PEDs in the water-phosphor detector are greater than those in the Cu-phosphor detector due to the greater attenuation of the beam in copper. Although the effect of greater attenuation in copper also explains the differences in PED between the water-water and Cu-water detectors, the magnitude of dose reductions resulting from the replacement of water with Cu in the latter pair of detectors (i.e. water-water and Cu-water) is smaller than that for the water-phosphor and Cu-phosphor detector pair. This difference arises from the difference in energy response of the detectors in question. While the energy spectrum that reaches both

the phosphor (in the Cu-phosphor detector) and water (in the Cu-water detector) are similar, except for backscatter, the absorbed dose in an individual detector will depend on its sensitivity to the radiation beam incident on it.

PEDs in the water-phosphor detector were expected to differ from those in the water-water detector. However, the magnitude of the difference seen for large field sizes was not anticipated. This result may be explained as follows. Compton scattering is the predominant mode of interaction in water for the energy range considered while, due to the high atomic number of Gd ($Z = 64$), there is significant photoelectric absorption of the lower-energy scattered photons (which predominates at large field sizes) in the phosphor, leading to an increase in PED for this material. Higher PEDs in water-water detector relative to those in water-phosphor detector are observed for small fields and result from the greater mass energy absorption coefficient for water at 1.25 MeV than for the phosphor at this energy (see figure 3-12).

As a function of air gap, the relative response of the various detectors are compared in figure 4-8 for a 20-cm thick phantom and 30 x 30 cm^2 field. As in the preceding discussion, the PED in the phosphor-based detectors is higher than that in the water-based detectors. In addition, the replacement of water with Cu (as is the case for water-phosphor and Cu-phosphor detectors, or for water-water and Cu-water detectors) lead to lower PEDs. Furthermore, the difference in response for any pair of detectors (except for the water-water and copper-water pair) decreases as the air gap increases. This is due to

the relative decrease of the low energy scattered photons, to which the phosphor is sensitive, with increasing air gap.

4.4 Conclusions

The influence of the patient/detector geometry and detector material on PEDs has been studied. The PED was found to decrease roughly exponentially with increasing air gap due to the loss of radiation equilibrium in the air gap. As a function of field size, the PED, in the case of small air gaps, was observed to follow the shape associated with the increase of scatter in phantom. That is, an initial rapid increase, with the rate of increase becoming less as the field size increases. For large air gaps, however, the initial increase of the PED with field size was more gradual. As expected, the PED decreased exponentially as the phantom thickness was increased. This was attributed mainly to the exponential attenuation of the primary component. The foregoing discussion shows that changes in the scatter fluence arising from variations in the phantom/detector geometry significantly affects the exit dose in a metal-phosphor detector.

Comparisons of the relative response of various detector materials showed a significant difference, with the phosphor-based detectors exhibiting a high response compared to the water-based detectors in those situations where the intensity of the scattered photons reaching the detector was large (e.g. large field size and small air gap). In cases of limited scatter at the detector (e.g. small field sizes and/or large air gaps), the relative response of water was found to be slightly higher than that of phosphor. These indicate that the exit

dose (or PED) detected is significantly affected by the atomic composition (or atomic number) of the particular detector used. This effect needs to be considered in order to be able to accurately calculate the dose deposited in a metal-phosphor detector. The existing dose calculation algorithms (which do not account for dose perturbations due to changes in atomic numbers) need to be improved if they are to be used to predict the exit dose to a metal phosphor detector.

References

1. J. Leong, "Use of digital fluoroscopy as an on-line verification device in radiation therapy," Phys. Med. Biol. **31,** 985-992 (1986).

2. J. W. Wong, J. W. Slessinger et al, "Portal Dose Images I: Quantitative Treatment Plan Verification," Int. J. Rad. Oncol. Biol. Phys. **18,** 1455-1463 (1989).

3. X. Ying, L. Y. Geer and J. W. Wong, "Portal Dose Images II: Patient Dose Estimation," Int. J. Rad. Oncol. Biol. Phys. **18,** 1465-1475 (1990).

4. B. J. M. Heijmen, J. S. Stroom, H. Huizenga, and A. G. Visser, "In vivo dose measurements using an electronic portal imaging device: A feasibility study," Radiother. Oncol. **24** Suppl., S25 (1992).

5. B. J. M. Heijmen, J. S. Stroom, H. Huizenga, and A. G. Visser, "Application of a fluoroscopic portal imaging system with a CCD camera for accurate in vivo dosimetry (Abs.)," Med. Phys. **20,** 870 (1993).

6. M. C. Kirby, and P. C. Williams, "The use an electronic portal imaging device for exit dosimetry and quality control measurements (abs)," Int. J. Rad. Oncol. Biol. Phys. **27,** Suppl. 1, 165 (1993).

7. M. C. Kirby, and P. C. Williams, "Measurement possibilities using an electronic portal imaging device," Radiother. Oncol. **29,** 237-243 (1993).

8. V. N. Hansen, P. M. Evans, and W. Swindell, "Transit dosimetry: Computer generated dose images for verification," *in Proceedings of the Xith ICCR (International Congress on the use of Computers in Radiation Therapy)*, edited by A. R. Hounsell, J. M. Wilkinson, and P. C. Williams (Christie Hospital NHS Trust, Manchester, 1993), pp. 166-117.

9. S. Pistorius and C. Yeboah, "Analysis and modeling of electronic portal imaging exit dose measurements," Radiother. Oncol. **37** (Suppl. 1), S21 (1995).

10. C. Yeboah and S. Pistorius, "Investigation of the factors that affect the use of an electronic portal imaging device for quantitative dosimetry (abs)," Med. Phys **23**, 811 (1996).

11. R. Rajapakshe, Optimization of a real-time portal imaging system for quantitative imaging, Ph.D. Thesis, University of Manitoba, Winnipeg, Canada (1995).

12. P. Stucchi, L. Conte, C. Mordacchini et al., "The use of an electronic portal imaging device for exit dosimetry," Radiother. Oncol. **37** (Suppl. 1), S21 (1995).

13. W. Swindell and P. M. Evans, "Scattered radiation in portal images: A Monte Carlo simulation and a simple physical model," Med. Phys. **23,** 1-11 (1996).

14. T. R. McNutt, T. R. Mackie, P. Reckwerdt, N. Papanikolaou, and B. R. Paliwal, "Calculation of portal dose using the convolution/superposition method," Med. Phys. **23,** 527-535 (1996).

15. T. R. McNutt, T. R. Mackie, P. Reckwerdt, and B. R. Paliwal, "Modeling dose distributions from portal dose images using the convolution/superposition method," Med. Phys. 23, 1381-1392 (1996).

16. T. R. Mackie, J. W. Shrimger and J. J. Battista, "A convolution method of calculating dose for 15 MV X-rays," Med. Phys. **12,** 188-196 (1985).

17. R. Mohan and C. Chui, "Differential pencil beam dose computational model for photons," Med. Phys. **13,** 64-73 (1986).

18. A. Ahnesjö, P. Andreo, and A. Brahme, "Calculation and application of point spread functions for treatment planning with high energy photon beams," Acta. Oncol. **26,** 49-56 (1987).

19. A. Ahnesjö, "Collapsed cone convolution of radiant energy for photon dose calculations in heterogeneous media," Med. Phys. **16,** 577-592 (1989).

20. J. R. Cunningham, "Tissue inhomogeneity corrections in photon-beam treatment planning," *in Progress in Modern Radiation Physics*, edited by C. G. Orton (Plenum Press, New York, 1985), 103-131.

21. J. W. Wong and J. A. Purdy, "Review of methods of inhomogeneity corrections," in Medical Physics monograph No. 19, edited by J. A. Purdy (American Institute of Physics, Inc., 1992), 887-899.

22. M. R. Sontag and J. R. Cunningham, "The equivalent tissue-air ratio method for making absorbed dose calculations in a heterogeneous medium," Radiology **129**, 787-798 (1978).

23. M. E. J. Young and R. O. Kornelsen, "Dose corrections for low-density tissue inhomogeneities and air channels for 10-MV x rays," Med. Phys. 10, 450-455 (1983).

24. J. E. O'Connor, "The density scaling theorem applied to lateral electronic equilibrium," Med. Phys. 11, 678-680 (1984).

25. K. Yuen, B. J. McParland and R. O. Kornelsen, "A differential method for inhomogeneity correction on dose in a photon beam," Med. Phys. **11**, 15-21 (1984).

26. S. Pistorius, "Convolution based, analytic models for broad beam kerma (abs)," Med. Phys. **20**, 905 (1993)

27. M. K. Woo and J. R. Cunningham, "The validity of the density scaling method in primary electron transport for photon and electron beams," Med. Phys. **17**, 187-194 (1990).

28. M. K. Woo, "Analysis of photon beam exit dose using photon point kernels," Phys. Med. Biol. **39**, 687-702 (1994).

29. G. D. Lambert, W. E. Liversage, A. M. Hirst, and D. Doughty, "Exit dose studies in megavoltage photon therapy," B.J.R. **56**, 329-334 (1983).

30. D. A. Jaffray, J. J. Battista, A. Fenster, and P. Munro, "X-ray scatter in megavoltage transmission radiography: Physical characteristics and influence on image quality," Med. Phys. **21**, 45-60 (1994).

31. B. Wowk, T. Radcliffe, K. W. Leszczynski, S. Shalev, and R. Rajapakshe, "Optimization of metal/phosphor screens for on-line portal imaging," Med. Phys. **21**, 227-235 (1994).

32. T. Radcliffe, G. Barnea, B. Wowk, R. Rajapakshe, and S. Shalev, "Monte Carlo optimization of metal/phosphor screens at megavoltage energies," Med. Phys. **20**, 1161-1169 (1993).

33. W. R. Nelson, H. Hirayama, and D. W. O. Rogers, "The EGS4 Code System," Stanford Linear Accelerator Centre Report SLAC-265 UC-32, National technical Information Services, U.S. Dept. of Commerce, 5285 Port Royal Road, Springfield, Virg-22161 (1985).

34. D. W. O. Rogers, "Fluence to dose equivalent conversion factors calculated with EGS3 for electrons from 100 keV to 20 GeV and photons from 11 keV to 20 GeV," Health Physics **46**, 891-914 (1984).

35. D. W. O. Rogers, "Low energy electron transport with EGS", Nuclear Instruments and Methods **A227**, 535-548 (1984).

36. British Journal of Radiology, Central Axis Depth Dose Data for Use in Radiotherapy, B.J.R. Supplement No. **17**, 115-119 (1983).

37. B. L. Werner, I. J. Das, F. M. Khan and A. L. Meigooni, "Dose perturbations at interfaces in photon beams," Med. Phys. **14**, 585-595 (1987).

38. I. J. Das and F. M. Khan, "Backscatter dose perturbation at high atomic number interfaces in megavoltage photon beams," Med. Phys. **16**, 367-375 (1989).

39. I. J. Das, K. R. Kase, A. S. Meigooni, F. M. Khan, B. L. Werner, "Validity of transition-zone dosimetry at high atomic number interfaces in megavoltage photon beams," Med. Phys. **17**, 10-16 (1990).

40. B. L. Werner, I. J. Das and W. N. Salk, "Dose perturbations at interfaces in photon beams: Secondary electron transport," Med. Phys. **17**, 212-226 (1990).

41. O. A. Sauer, "Calculation of dose distributions in the vicinity of high-Z interfaces for photon beams," Med. Phys. **22**, 1685-1690 (1995).

42. H. E. Johns and J. R. Cunningham, The Physics of Radiology, Fourth edition (Charles C. Thomas, Publisher, 1983), 734.

43. F. H. Attix, Introduction to Radiological Physics and Radiation Dosimetry (J. Wiley and Sons, Inc., 1986), 570.

Energy (MeV)	PED due to the Primary (%)		
	Monte Carlo	Analytical	Discrepancy(%)
1.25	24.75 ± 0.45	23.13	6.6
2	31.87 ± 0.48	30.72	3.6
5	60.57 ± 1.43	65.39	-8.0

Table 4-1. The percentage exit dose (PED) in the limit of 0 x 0 cm^2 field size. The geometry consist of a 20-cm thick phantom and 30-cm air gap. Data generated with the Monte Carlo method is compared with that obtained analytically. The analytic calculations consider only primary attenuation, neglect interface effects that arose from the presence of the copper-phosphor interface and assume the presence of electronic equilibrium.

Energy (MeV)	PED_{ob} (%)		
	Monte Carlo	Analytical	Discrepancy(%)
1.25	89.60 ± 0.15	82.02	8.5
2	85.95 ± 0.11	82.52	4.0
5	112.42 ± 0.10	119.86	-6.6

Table 4-2. The percentage exit doses for zero phantom thickness and 0 x 0 cm^2 field size (i.e. PED_{ob}) calculated analytically are compared with Monte Carlo data. The analytical calculations only consider the attenuation of the primary photons, neglect interface effects and assume the presence of electronic equilibrium in the phosphor.

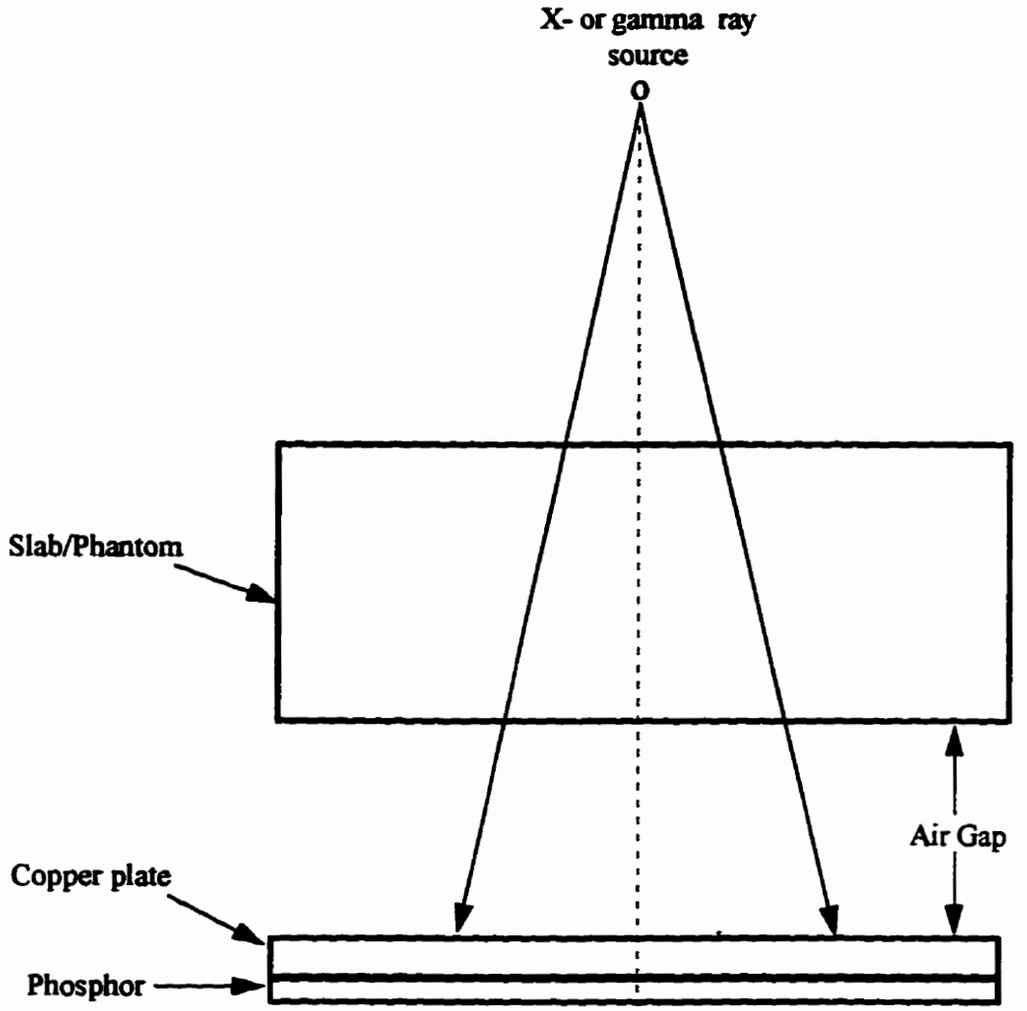

Figure 4-1. Schematic diagram of the diverging beam geometry associated with the parallel beam geometry of figure 3-1. A monoenergetic beam of photons from a point source was allowed to fall on a slab water phantom at a specified field radius. On emerging from the phantom, the beam is detected with a Cu-Gd_2O_2S phosphor, located at a specified distance from the exit surface of the phantom.

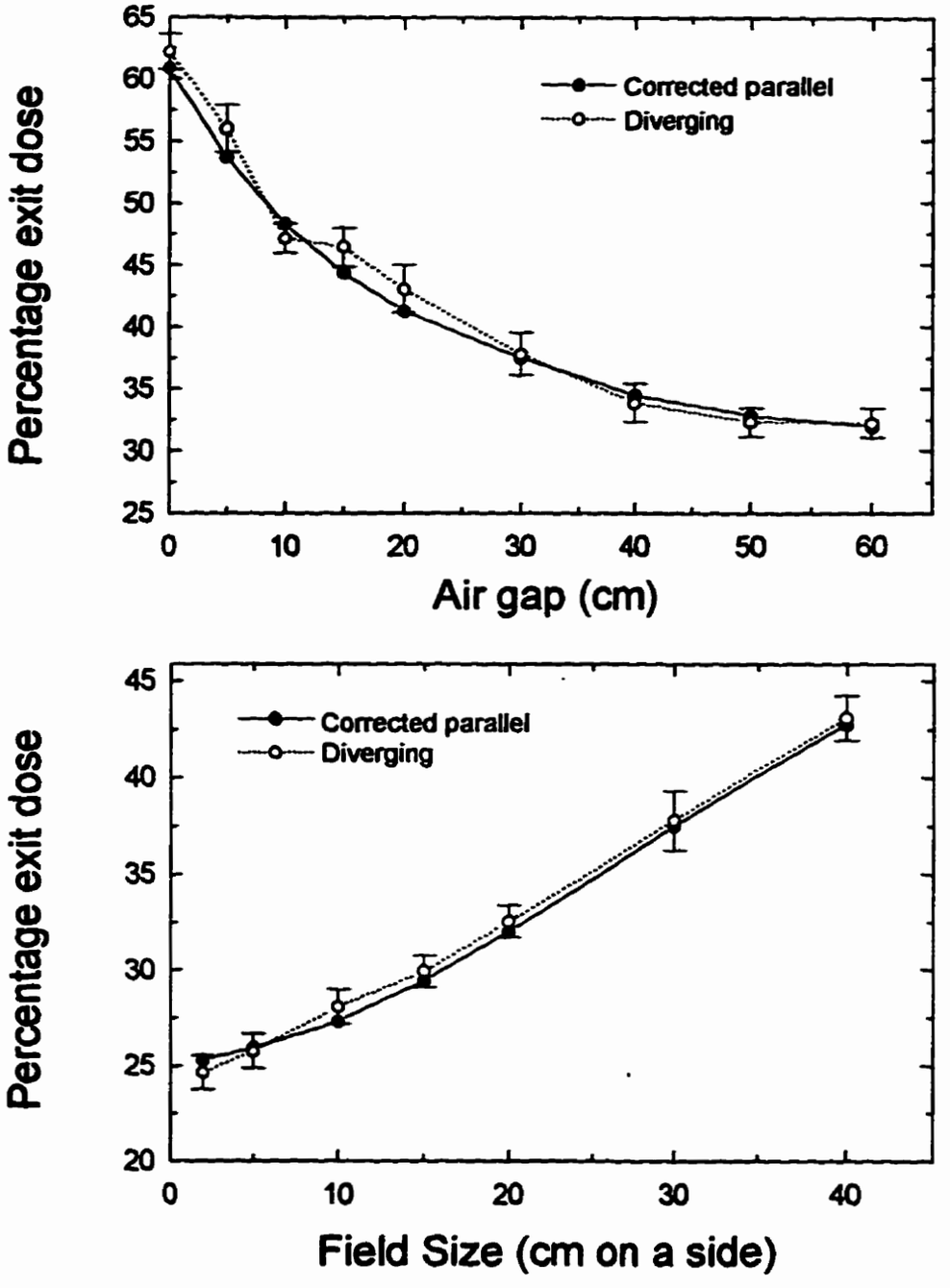

Figure 4-2. The reciprocity theorem was applied to a parallel beam geometry and the resulting data converted from infinite to finite SSD (solid circles joined by solid lines). These data are compared with PEDs obtained directly with a diverging beam geometry (open circles connected with dotted lines) for 1.25-MeV incident beams. The error bars associated with the diverging beam data indicate one standard deviation. No errors are shown for the corrected parallel beam data as such errors are less than the size of the data points. (a) PED as a function of air gap for 20-cm thick phantom and 30 x 30 cm^2 field size. (b) PED as a function of field size for 20-cm thick phantom and 30-cm air gap.

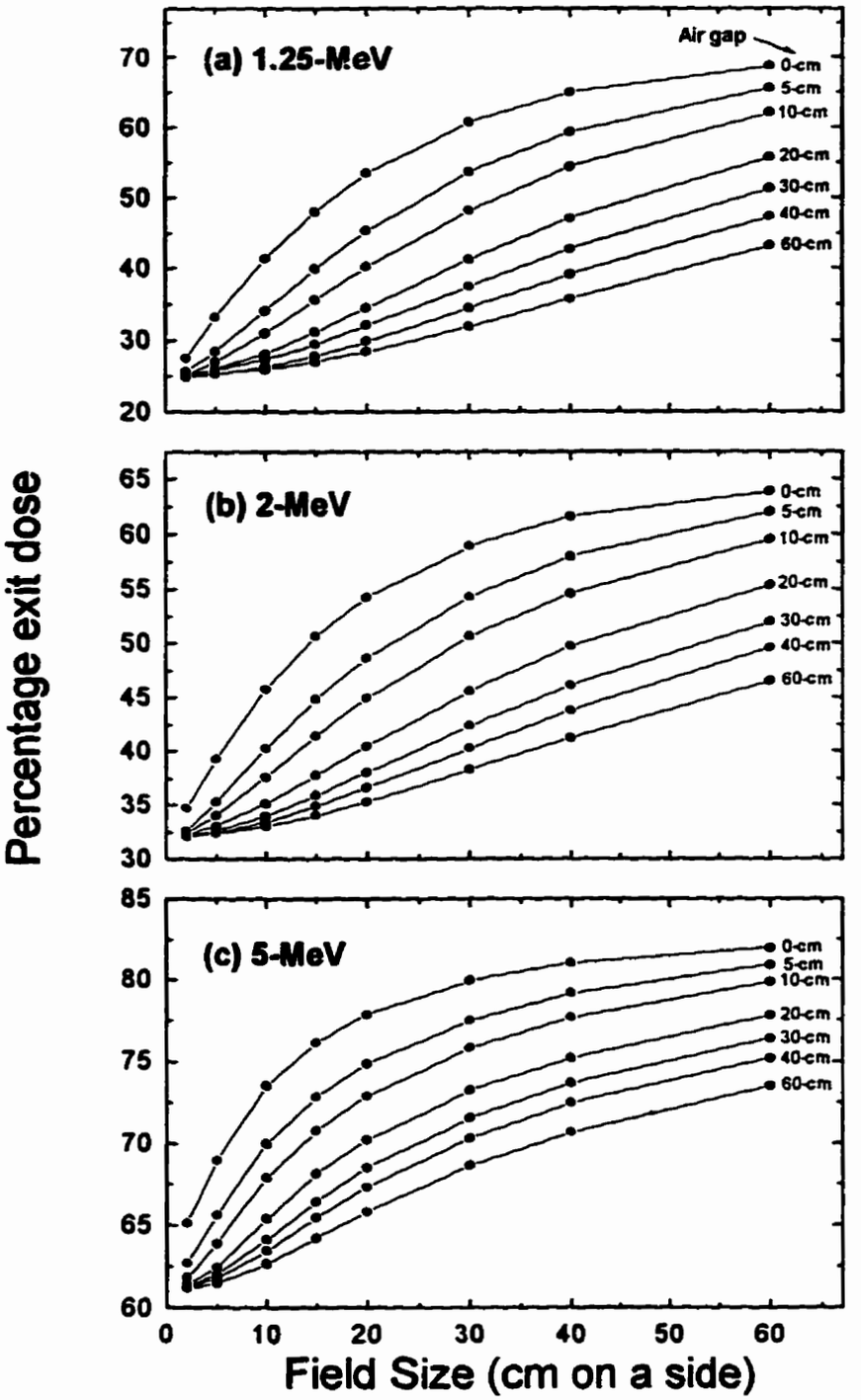

Figure 4-3. The dependence of PED on field size (length of side for square field) for (a) 1.25-, (b) 2-, and (c) 5-MeV incident beams. Geometry: 20-cm thick phantom, 0, 5, 10, 20, 30, 40, and 60 cm air gaps.

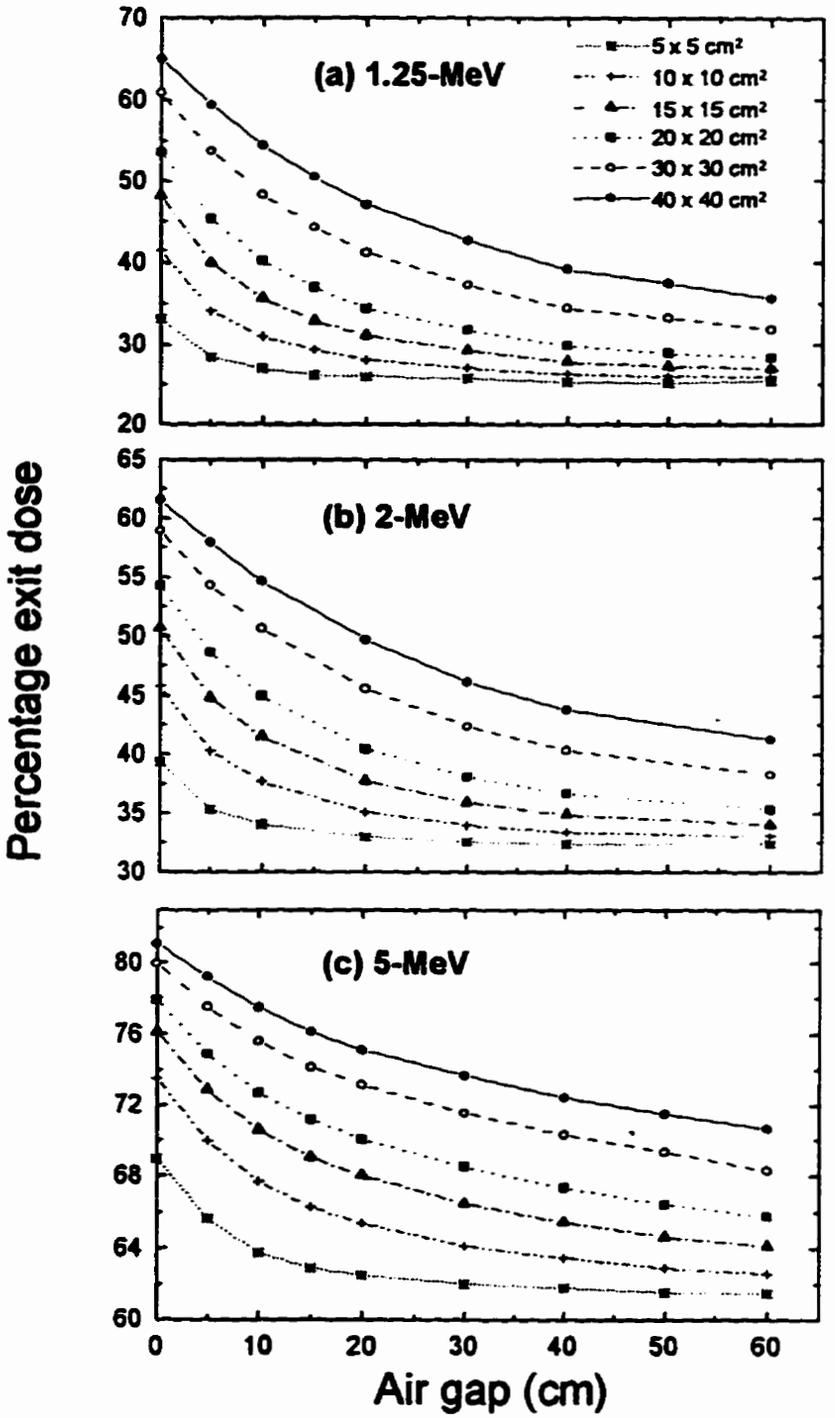

Figure 4-4. The PED as a function of air gap for (a) 1.25-, (b) 2-, and (c) 5-MeV incident beams. Geometry: 20-cm thick phantom, 5 x 5, 10 x 10, 15 x 15, 20 x 20, 30 x 30, and 40 x 40 cm^2 field sizes.

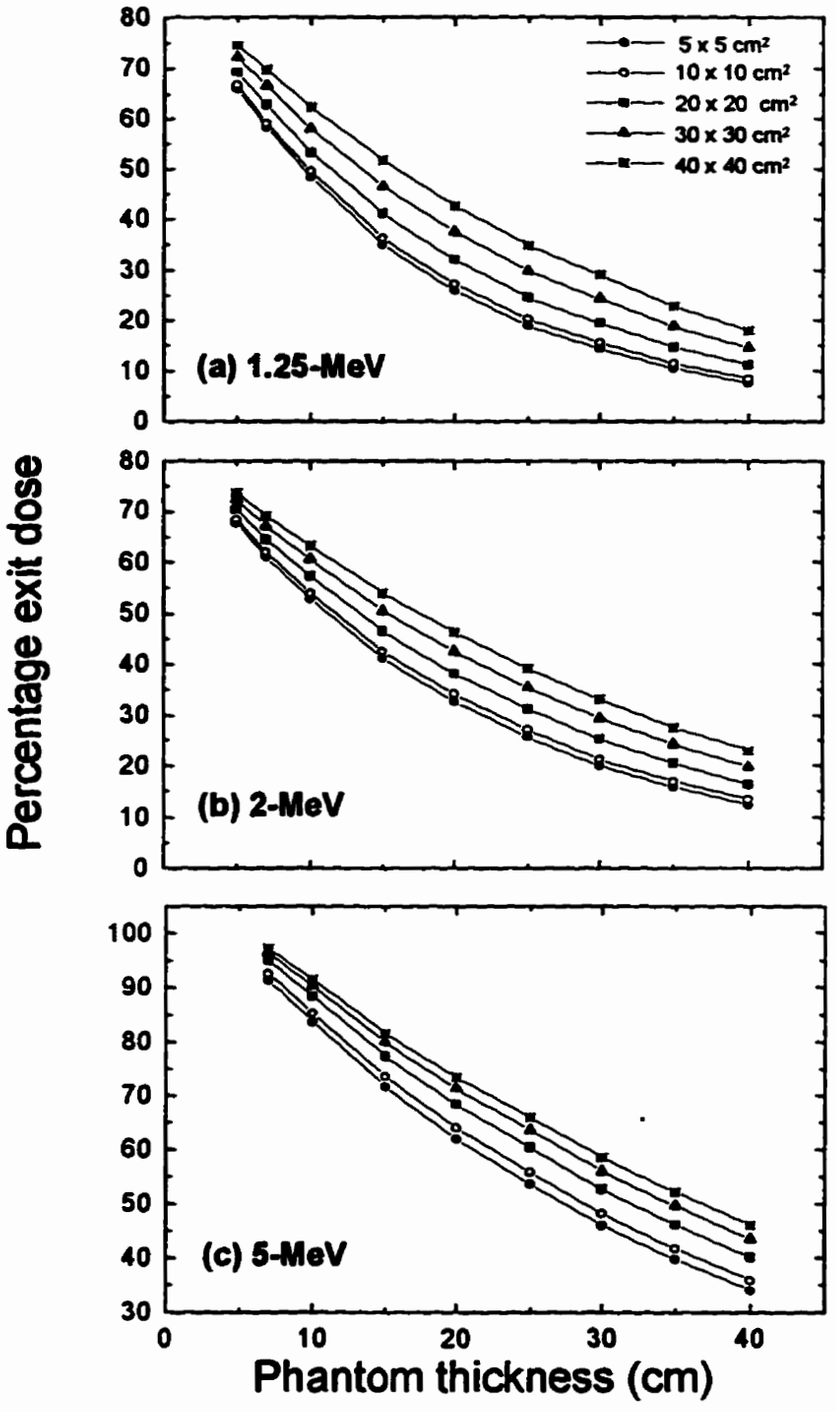

Figure 4-5. The dependence of PED on phantom thickness for (a) 1.25-MeV, (b) 2-MeV, and (c) 5-MeV incident beams. Geometry: 30-cm air gap, 5 x 5, 10 x 10, 20 x 20, 30 x 30, and 40 x 40 cm^2 field sizes.

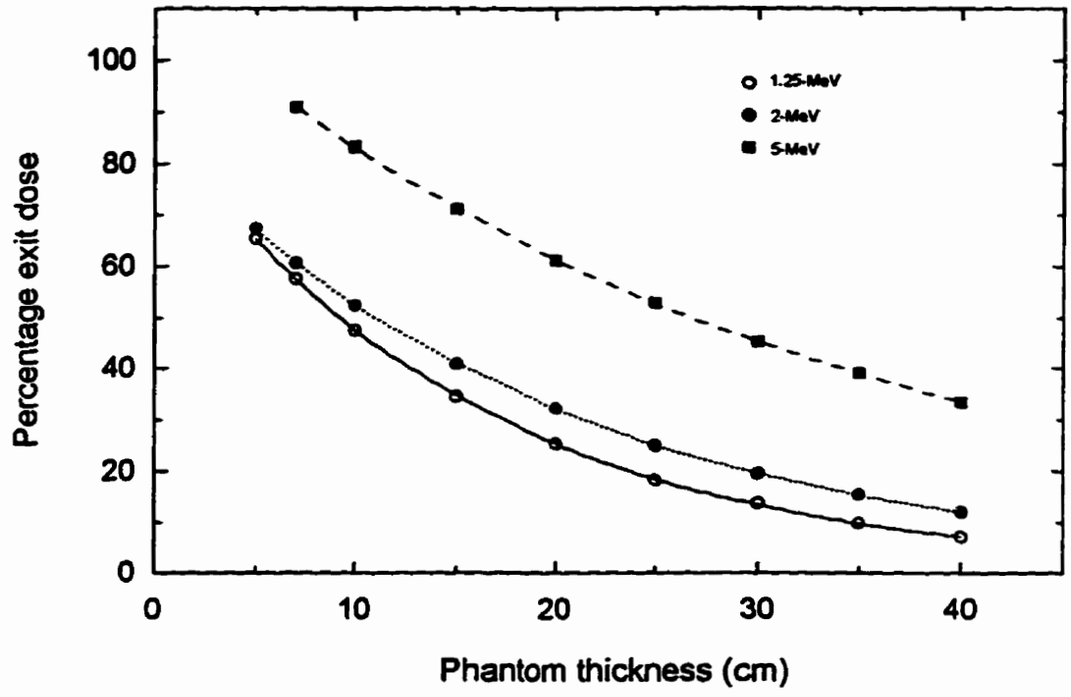

Figure 4-6. The PED under open beam conditions (i.e. in the absence of phantom) for 1.25, 2, and 5 MeV incident beams were determined from this figure, which shows the dependence of PED on phantom thickness for 2 x 2 cm^2 field size and 30-cm air gap. The data points are the Monte Carlo results. The curves are the fit to the Monte Carlo data generated with equation (4-4).

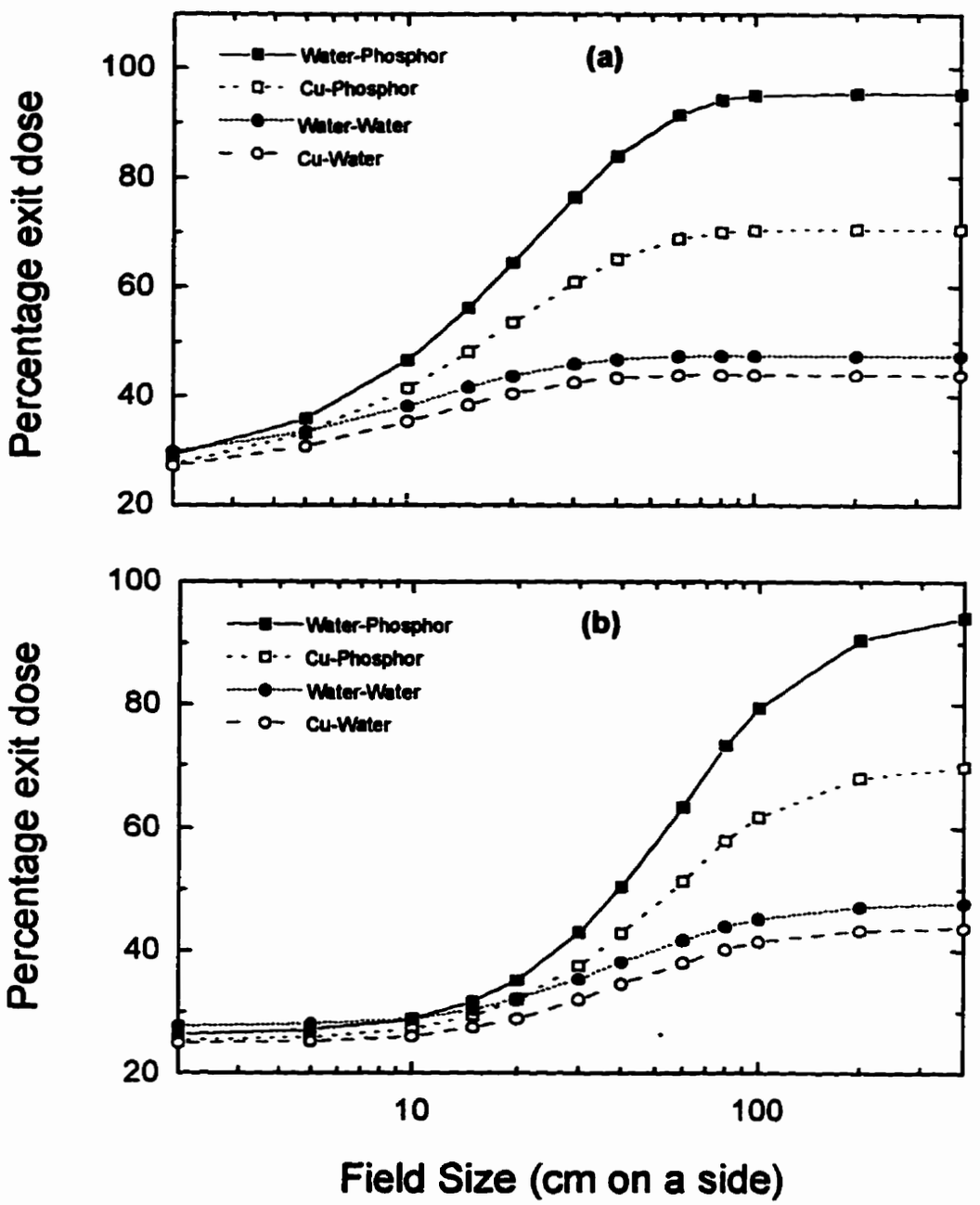

Figure 4-7. The PED in various detector media (water-phosphor, Cu-phosphor, water-water, and Cu-water) as a function of field size for 1.25-MeV incident beams. Geometry: (a) 0-cm air gap, 20-cm thick phantom; (b) 30-cm air gap, 20-cm thick phantom.

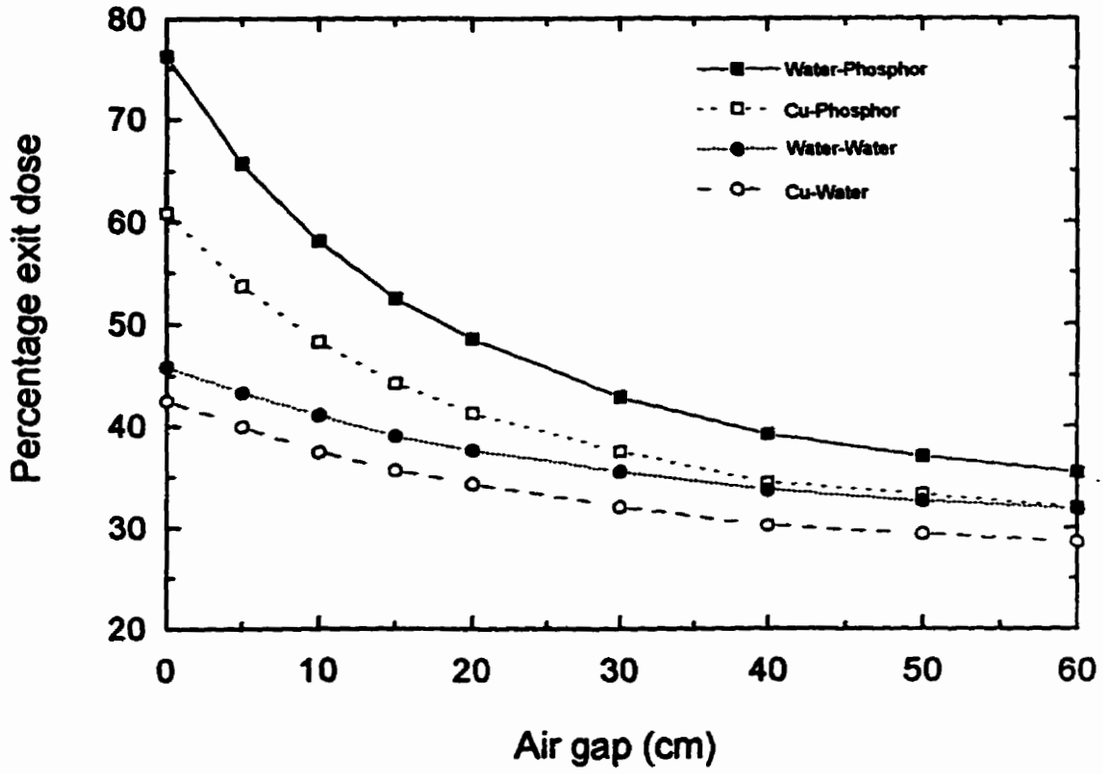

Figure 4-8. The PED in various detector media (water-phosphor, Cu-phosphor, water-water, and Cu-water) as a function of air gap for 1.25-MeV incident beams. Geometry: 20-cm thick phantom, 30 x 30 cm^2 field size.

Chapter 5

An equivalent field size technique for modeling an air gap

5.1 Introduction

In megavoltage portal imaging, there is often a large and variable air gap between the distal surface of the patient and the portal imaging detector. In an attempt to predict the portal dose image (i.e. the dose distribution in the detector plane) using conventional techniques, one would have to treat the air gap as an inhomogeneity, in which case the existing techniques for calculating dose in heterogeneous media are assumed to be applicable. One of these techniques is the density scaling method,[1-4] which scales the thickness of the inhomogeneity in proportion to its relative electron density. This technique, or some form of it, is generally employed by some of the dose calculation algorithms currently in use clinically,[2-5] and by the more advanced convolution models[7-10] (which are under investigation in the laboratory) to handle inhomogeneities.

To correct for an inhomogeneity, the path between the scattering volume element and the calculation point is scaled by an effective density. This step is an approximation which may tend to break down for extreme situations, such as air gaps, and even the more advanced convolution models have been shown to overestimate dose in the region following an air gap.[10,11] The reason for the overestimation is that the density scaling method assumes that the secondary electrons and scattered photons resulting from first

interactions of primary photons travel in straight-lines, whereas the electrons/photons that enter the air gap are actually traveling in various directions and continue to spread further in the air gap. Therefore, for the same water equivalent path-length, the electrons/photons will spread more in the presence of an intervening gap than with no gap. Thus, the calculated dose includes those electrons/photons which in reality have traveled away from the points of calculation on the central axis in the medium after the gap. It has been shown that, in general, the region immediately below an air gap would be the most inaccurate case for the density scaling calculation, with the error increasing with larger air gaps and smaller field sizes.[11] Due to this air gap problem, the density scaling technique employed by the convolution/superposition methodology may lead to inaccurate dose calculations in metal/phosphor portal imaging detectors, which are generally fairly thin.

Analysis of the spectral characteristics of exit photon beams reaching the portal imaging detector carried out in chapter 3, and of exit doses in chapter 4 revealed that the effects of air gap and field size are roughly complementary. It follows therefore that it may be possible to use an equivalent field size technique to model the air gap, thereby allowing us to use conventional dose calculation algorithms with only minor changes. The focus of the current chapter is to study the feasibility of using such an approach for quantifying the air gap effect on exit doses.

5.2 Materials and methods

5.2.1 Development of the equivalent field size technique by Monte Carlo modeling

For a given patient/detector geometry involving a patient or phantom thickness d, an air gap of magnitude t and a circular field of radius r (i.e. the clinical geometry), there exists a corresponding geometry with the same source-to-surface distance, same phantom thickness, but which does not include an air gap (i.e. the reference geometry). A field radius r_{eq} in a reference geometry is said to be equivalent to a field radius r in a corresponding clinical geometry if both of these field sizes result in the same exit dose (after correcting for inverse square effect arising from changing source-to-detector distance). The relationship between the equivalent field radius r_{eq} and the clinical/actual field radius r is the empirical model we seek. Unless otherwise specified, all field sizes or radii are defined at 100-cm from the source. It must also be emphasized that the inverse square effect does not need to be considered since the quantity being studied is the ratio of doses at the same distance.

For contact imaging (i.e. under zero air gap conditions), $r_{eq} = r$ by definition of the equivalent field size. As the air gap becomes infinitely large, the exit dose approaches the primary value since all scattered photons originating from the phantom escape the detector under this condition (see section 4.3.3). It follows therefore that r_{eq} approaches zero for infinite air gaps. Based on the foregoing considerations and on our understanding of

energy spectra and exit doses developed in chapters 3 and 4, we hypothesize a relationship of form

$$r_{eq} = r / [1 + (\alpha / \beta) \ln(1 + \beta \cdot t)] \qquad (5\text{-}1),$$

between the equivalent field radius, r_{eq}, and the actual/clinical field radius, r. In eqn. (5-1), t represents the air gap, α and β are parameters which might be functions of phantom thickness d and incident beam quality. In addition, α is expected to depend on the relative response of the detector to scattered photons. To confirm this, consider an ideal detector which responds only to the monoenergetic primary photons (i.e. a detector whose response is a delta-function). The exit dose that would be deposited in such a detector will be equal to the primary dose and will remain constant (after correcting for inverse square) regardless of the magnitude of the air gap and the actual/clinical field radius. For this ideal detector, no scaling of the actual/clinical field radius will be required since the exit dose is not affected by the air gap. It follows that $r_{eq} = r$ in eqn. (5-1) for all values of t and r, and hence $\alpha = 0$ under these conditions.

If the detector's relative response is independent of energy, then this detector will respond equally well to both the scattered and the primary photons. Since scatter dose decreases with increasing air gap (see section 4.3.3),[12] the exit dose deposited in the detector will likewise decrease. Consequently, for this detector, a non-zero field radius r employed in a clinical geometry (involving a non-zero air gap) will be greater than the equivalent field radius r_{eq} in the corresponding reference geometry. It follows from eqn. (5-1) that α must

be greater than zero in this case. We therefore anticipate that α will increase with the relative sensitivity of detector to scattered photons.

To study the equivalent field size expression, eqn. (5-1), the well known scatter-radius function[13] given by eqn. (5-2) was chosen to represent the Monte Carlo simulated data:

$$S(r) = S_{\infty}[1 - exp(-\lambda r) - \mu\lambda r\, exp(-\lambda r)] \qquad (5\text{-}2),$$

where S(r) = central-axis scatter in field of radius r;

S_{∞} = central-axis scatter in field of infinite radius;

λ is a scale parameter of dimension length^{-1};

μ is a dimensionless shape parameter lying between 0 and 1.

As the name implies, this scatter-radius function is applicable to central-axis scatter dose. Since the quantity being dealt with in this section is the percentage exit dose (PED), an analogous expression was used:

$$PED(r_{eq}) = PED_0 + (PED_{\infty} - PED_0)[1 - exp(-\lambda r_{eq}) - \mu\lambda r_{eq}\, exp(-\lambda r_{eq})] \qquad (5\text{-}3),$$

where $PED(r_{eq})$ = percentage exit dose in equivalent field of radius r_{eq};

PED_0 = percentage exit dose in equivalent field of zero radius; and

PED_{∞} = percentage exit dose in equivalent field of infinite radius.

Notice that eqn (5-3) has the equivalent field size expression, eqn. (5-1), built into it through the use of r_{eq}. Therefore by fitting eqn. (5-3) to the Monte Carlo calculated PED

data and analyzing the resulting information, we were able to study the proposed equivalent field size expression. It must be emphasized that eqn. (5-3) is not used with the intent to model exit doses but it is used merely as a means to facilitate the development and analysis of the equivalent field size model.

5.2.2 Experimental validation of the Monte Carlo modeling

Experimental confirmation of the Monte Carlo results was carried out using a Cobalt-60 teletherapy unit (Theratron 780C). The geometry, depicted in figure 5-1, comprises of a Lucite slab phantom and a detector, consisting of a farmer-type ionization chamber (Capintec) with a 1.6 cm diameter Polysterene buildup cap at the center of a 2.4-cm thick slab of Lucite (i.e. ion chamber-in-slab detector). The detector was designed in this manner to attempt to imitate the metal/phosphor detector used in the Monte Carlo simulations. The distance from the radiation source to the exit surface of the Lucite phantom was held fixed at 100-cm and the phantom thickness was varied by adding new material to the side of the phantom closest to the source. To change the air gap, the source-to-detector distance was varied. Using this geometry, measurements were made at a number of air gaps (0-60 cm) and for a range of field sizes (5 x 5 to 35 x 35 cm^2) and phantom thicknesses (5.5, 20 and 32.6 cm) with the ion chamber connected to an electrometer (CNMC K616, CNMC Company, Nashville, TN). Following this the detector was modified by replacing the ion chamber-in-a-slab detector with an ion chamber with a build-up cap (i.e. ion chamber-in-air detector), and a new set of measurements were made. The measured data were analyzed to verify the feasibility of

the equivalent field size concept and the validity of eqn (5-1). Unless otherwise specified, the inverse square factor that arose from changing air gaps (or equivalently, varying source-to-detector distances) was removed from the data.

5.3 Results and discussion

5.3.1 The equivalent field size technique

The least squares fit of eqn. (5-3) to the Monte Carlo calculated PEDs is shown in figures 5-2 and 5-3 for 1.25- and 5-MeV incident beams, respectively. In this section, we have chosen to discuss a 20-cm thick phantom since the fits for different thicknesses have similar features. The data points in the figures are the Monte Carlo data while the surfaces are the least squares fit to these data generated with eqn. 5-3. The error bars indicate the 95% prediction intervals (which are measured at a given field radius and air gap) and consist of the PED range associated with a 95% probability for the PED value in an experiment. Note that all the Monte Carlo data lie within the 95% prediction intervals. For 1.25-MeV beams the root-mean-square difference between eqn. 5-3 and the Monte Carlo data (i.e. standard error of fit) is 0.660. The corresponding value for 5-MeV beams is 0.374. There is therefore good agreement between eqn. (5-3), into which the equivalent field size expression (eqn. (5-1)) is incorporated, and the Monte Carlo data. This suggests that the proposed equivalent field size concept is feasible and that eqn. (5-1) is an appropriate model for the equivalent field radius.

In figure 5-4, the dependence of β (see eqn. (5-1)) on phantom thickness is shown. The error bars associated with the data points represent the 95% confidence limits. For both 1.25- and 5-MeV beams β is independent of phantom thickness within the limits of uncertainties. The average values of β, weighted by the inverse-squared errors, are given by $\beta = 0.022 \pm 0.002$ cm^{-1} and 0.024 ± 0.004 cm^{-1} for 1.25- and 5-MeV incident beams, respectively, where the errors represent two standard deviations. Therefore, in addition to being independent of phantom thickness, β is independent of incident energy within the limits of our uncertainties. Unless otherwise specified, all errors represent two standard deviations.

Unlike β, α is a function of phantom thickness, detector response, and incident beam quality. For a copper/phosphor detector, α was found to be inversely proportional to phantom thickness d for the two incident energies studied (i.e. 1.25- and 5-MeV):

$$\alpha = \alpha_0 / d \qquad (5\text{-}4),$$

where α_0 is a dimensionless parameter which depends on incident beam quality; for 1.25- and 5-MeV beams $\alpha_0 = 2.15 \pm 0.04$ and 2.58 ± 0.10, respectively.

Using eqn. (5-4), the equivalent field size expression, eqn. (5-1), was verified independently by scaling the actual/clinical field radius r associated with each data point of figure 5-2 (and of figure 5-3) with the expression in question to yield the corresponding equivalent field radius r_{eq} at zero air gap. After scaling the actual field radii, the PED

which was originally associated with a given air gap, t_1 say, and field radius $r = r_1$, for example, would be associated with zero air gap ($t = 0$) and the equivalent field radius corresponding to r_1. Thus, after scaling the actual field radii r with eqn. (5-1), the PED surfaces of figures 5-2 and 5-3 should collapse into a single curve (figures 5-5 and 5-6, respectively), which coincides with the original PED curve for a zero air gap. Such curves have been shown for a variety of phantom thicknesses in figures 5-7 and 5-8. In these figures, the fitted surfaces are shown merely to make it easier to visualize the data points. For the same reason, the number of data points has been cut down. For a specified phantom thickness all the data points fall on a single curve.

5.3.2 Experimental validation of the equivalent field size model

To verify the equivalent field size expression, eqn. (5-1), experimentally, the actual/clinical field radius r was held fixed and the dose measured by an "ion chamber-in-a-slab detector" for this field radius r was measured for various air gaps. The equivalent field radius r_{eq} at zero air gap that resulted in the same dose as that observed with the clinical field radius r for each air gap was determined. In figures 5-9 and 5-10, the ratio of r to r_{eq}, r/r_{eq}, is shown as a function of air gap for a 20-cm thick phantom and r values of 13.8 and 19.2 cm, respectively (corresponding to 25 x 25 and 35 x 35 cm^2 square fields). The data points are the experimental data, the solid line is the least squares fit to the experimental data generated using the equivalent field size expression, eqn. (5-1), while the dashed lines represent the 95% prediction limits. For r = 13.8 cm, the root-mean-square difference between eqn. (5-1) and the experimental data is 0.044, while for r = 19.2 cm the root-

mean-square difference is 0.021. The goodness of fit in both cases confirms that eqn. (5-1) is an appropriate model for representing the experimental data. Similarly acceptable results were obtained for phantom thicknesses of 5.5 and 32.6 cm (see figures 5-11 and 5-12). As shown in figures 5-13 and 5-14, no significant difference was seen when the "ion chamber-in-slab" detector was replaced with an "ion chamber-in-air" detector.

In figure 5-15, the values of β observed experimentally are compared to values determined from Monte Carlo modeling. The errors bars shown indicate the 95% confidence intervals. One notes that the experimental and Monte Carlo values of β, 0.024 ± 0.002 and 0.023 ± 0.002 cm^{-1}, respectively, agree well within the limits of experimental and statistical uncertainties. The values of α (which is detector dependent) determined by Monte Carlo modeling are higher than the corresponding experimental values (see figure 5-16). This is expected since the copper/phosphor detector used for the Monte Carlo simulations has a higher relative response to scattered photons than the ion chamber used for the experimental measurements.[12]

To provide additional confirmation of the equivalent field size expression, eqn. (5-1), we ascertained whether or not the measured dose, as a function of field radii, for a specified air gap (curve **B**, figure 5-17a) duplicates measurements made at zero air gap (curve **A**, figure 5-17a) after scaling the clinical field radii. To do this, the ratio r/r_{eq} was determined from eqn. (5-1) for the air gap thickness in question using the experimental values of α and β. This ratio was then used to scale all the actual/clinical field radii r corresponding to the measured doses for the specified air gap under consideration (curve **B**). While this

scaling of the field sizes changes each clinical field radius r to the corresponding equivalent field radius, it does not affect the magnitude of the associated measured dose. As shown in figure 5-17b, measurements made at a specified air gap, 30 cm say, duplicate measurements obtained at zero air gap after scaling the clinical field sizes. This not only supports the proposed equivalent field size concept, but also verifies eqn. (5-1) as an appropriate expression for computing the equivalent field radius.

5.4 Summary and Conclusions

The feasibility of using an equivalent field size technique for quantifying the effect of the large and variable air gap (between the distal surface of the patient and the portal imaging detector) on exit doses has been investigated. A patient/detector geometry involving an air gap was referred to as the clinical geometry. The corresponding geometry with the same SSD, same phantom thickness but for which the detector is in contact with the phantom was designated the reference geometry. A field size in a reference geometry was said to be equivalent to a field size in the corresponding clinical geometry if both of these field sizes resulted in the same exit dose. We have proposed a numerical expression, eqn. (5-1), based on Monte Carlo modeling, for computing the equivalent field size. This expression implicitly states that the PED/exit dose that will be deposited in a portal imaging detector by a field radius r in a clinical geometry involving an air gap t and phantom thickness d, is the same as the PED/exit dose that will be deposited in the detector by an equivalent field of radius r_{eq}, when the detector is in contact with the phantom.

Experimental results have been presented, which not only confirm the equivalent field size concept, but also the proposed numerical expression, eqn. (5-1), for computing the equivalent field size. In this expression, β was observed to be a constant, independent of phantom thickness, detector response, and incident beam quality. The β value determined by Monte Carlo modeling, 0.023 ± 0.002 cm^{-1}, agrees well with the experimentally observed value of 0.024 ± 0.002 cm^{-1}. Unlike β, α was found to be a function of all the afore-mentioned variables. For a copper/Gd_2O_2S-phosphor detector, α is inversely proportional to phantom thickness d for the energies studied (see eqn. (5-4)). The α values determined by Monte Carlo modeling were higher than the corresponding experimental values. This is as anticipated since the copper/phosphor detector used for the Monte Carlo simulations has a higher relative response to scattered photons than the ion chamber employed in the experiments.

Since the equivalent field size technique developed in the current study relates the exit dose at zero air gap to the exit dose at a specified air gap, it is proposed as an approach for modeling the air gap. This technique is essentially a method for converting the PED/exit dose from one air gap to another. In other words, if PED/exit doses are known as a function of field size at one detector position, then the PED/exit dose at all other detector positions can be determined using the proposed equivalent field size method. An advantage of this technique is that it can be used with minimal modifications to the existing dose calculation algorithms and does not require the development of a new algorithm.

References

1. J. E. O'Connor, "The density scaling theorem applied to lateral electronic equilibrium," Med. Phys. 11, 678-680 (1984).

2. J. R. Cunningham, "Tissue inhomogeneity corrections in photon-beam treatment planning," *in Progress in Modern Radiation Physics*, edited by C. G. Orton (Plenum Press, New York, 1985), 103-131.

3. J. W. Wong and J. A. Purdy, "Review of methods of inhomogeneity corrections," in Medical Physics monograph No. 19, edited by J. A. Purdy (American Institute of Physics, Inc., 1992), 887-899.

4. M. R. Sontag and J. R. Cunningham, "The equivalent tissue-air ratio method for making absorbed dose calculations in a heterogeneous medium," Radiology **129**, 787-798 (1978).

5. K. Yuen, B. J. McParland and R. O. Kornelsen, "A differential method for inhomogeneity correction on dose in a photon beam," Med. Phys. **11**, 15-21 (1984).

6. M. E. J. Young and R. O. Kornelsen, "Dose corrections for low-density tissue inhomogeneities and air channels for 10-MV x rays," Med. Phys. 10, 450-455 (1983).

7. T. R. Mackie, J. W. Shrimger and J. J. Battista, "A convolution method of calculating dose for 15 MV X-rays," Med. Phys. **12**, 188-196 (1985).

8. A. Ahnesjō, P. Andreo, and A. Brahme, "Calculation and application of point spread functions for treatment planning with high energy photon beams," Acta. Oncol. **26**, 49-56 (1987).

9. A. Ahnesjō, "Collapsed cone convolution of radiant energy for photon dose calculations in heterogeneous media," Med. Phys. **16**, 577-592 (1989).

10. R. Mohan and C. Chui, "Differential pencil beam dose computational model for photons," Med. Phys. **13**, 64-73 (1986).

11. M. K. Woo and J. R. Cunningham, "The validity of the density scaling method in primary electron transport for photon and electron beams," Med. Phys. **17**, 187-194 (1990).

12. D. A. Jaffray, J. J. Battista, A. Fenster, and P. Munro, "X-ray scatter in megavoltage transmission radiography: Physical characteristics and influence on image quality," Med. Phys. **21**, 45-60 (1994).

13. British Journal of Radiology, Central Axis Depth Dose Data for Use in Radiotherapy, B.J.R. Supplement No. **17**, 105-113 (1983).

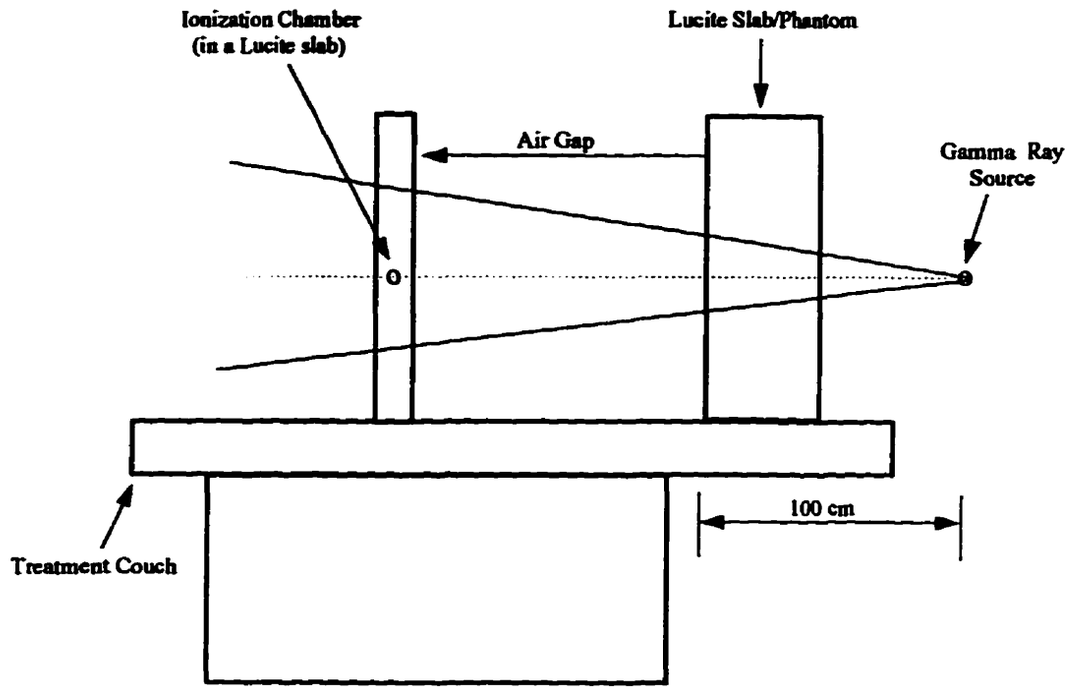

Figure 5-1. Schematic diagram of the experimental set-up. It consists of a Lucite slab phantom, whose exit surface is at a distance of 100 cm from the source, and a detector made up of an ion chamber and a thin slab of Lucite. The gantry was positioned at 90° in order to reduce backscatter.

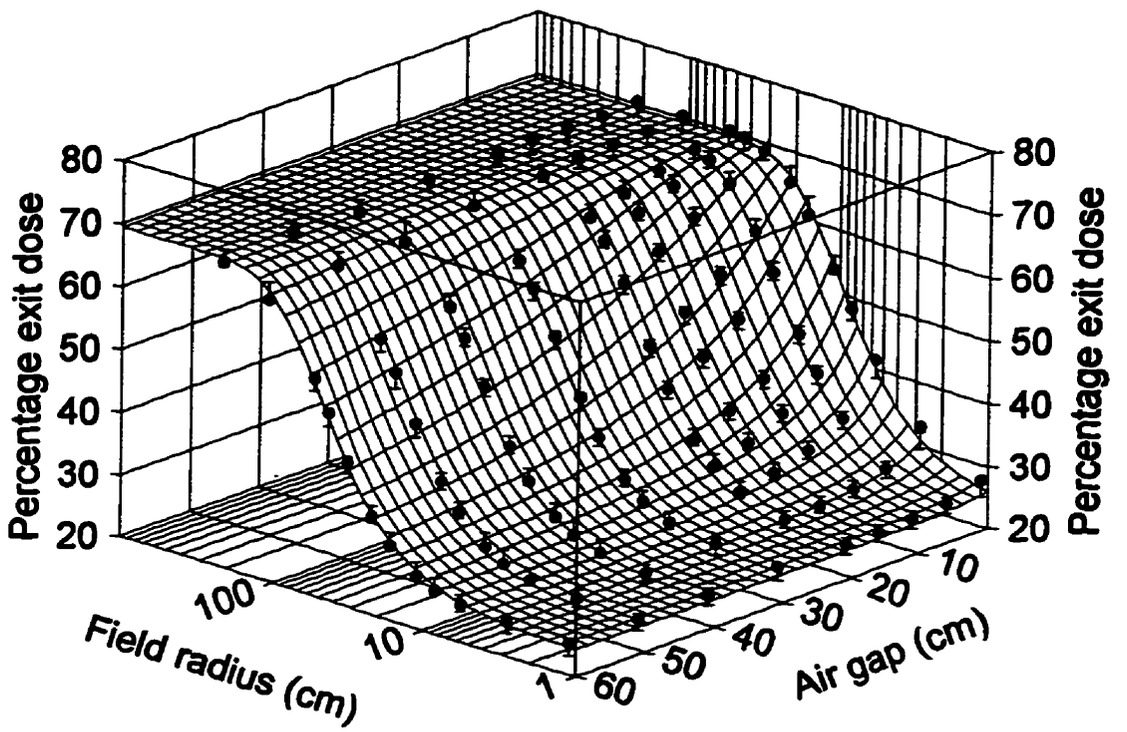

Figure 5-2. Percentage exit dose as function of field radius and air gap for a 20 cm thick phantom and 1.25-MeV incident beams. The data points represent the Monte Carlo calculated data while the surface is the least squares fit of eqn. (5-3) to these data. The error bars indicate the 95% prediction intervals.

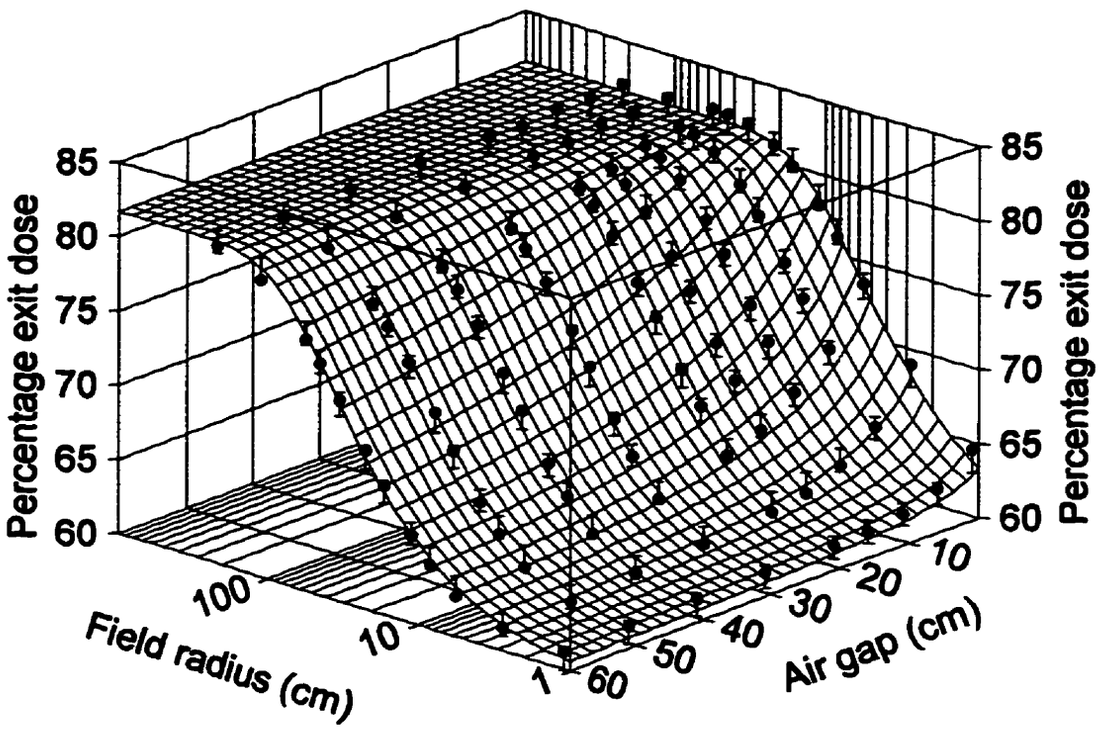

Figure 5-3. Percentage exit dose as function of field radius and air gap for a 20 cm thick phantom and 5-MeV incident beams. The data points represent the Monte Carlo calculated data while the surface is the least squares fit of eqn. (5-3) to these data. The error bars indicate the 95% prediction intervals.

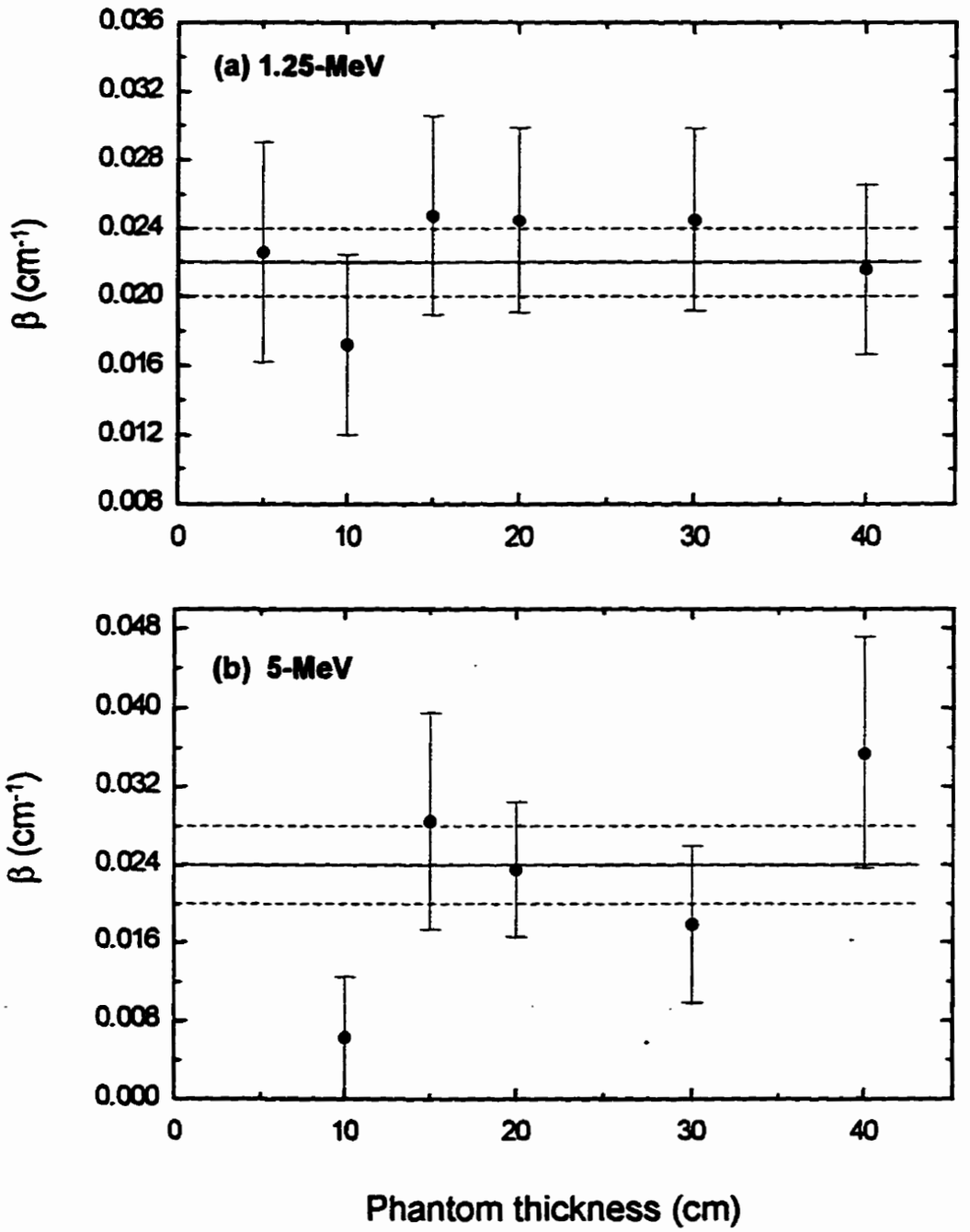

Figure 5-4. The dependence of β on phantom thickness derived from Monte Carlo modeling. The error bars represent the 95% confidence intervals associated with the individual data points, the solid line indicates the weighted mean value of β, while the dashed lines define the 95% confidence limits of the weighted mean value. (a) 1.25-MeV incident beams. (b) 5-MeV incident beams.

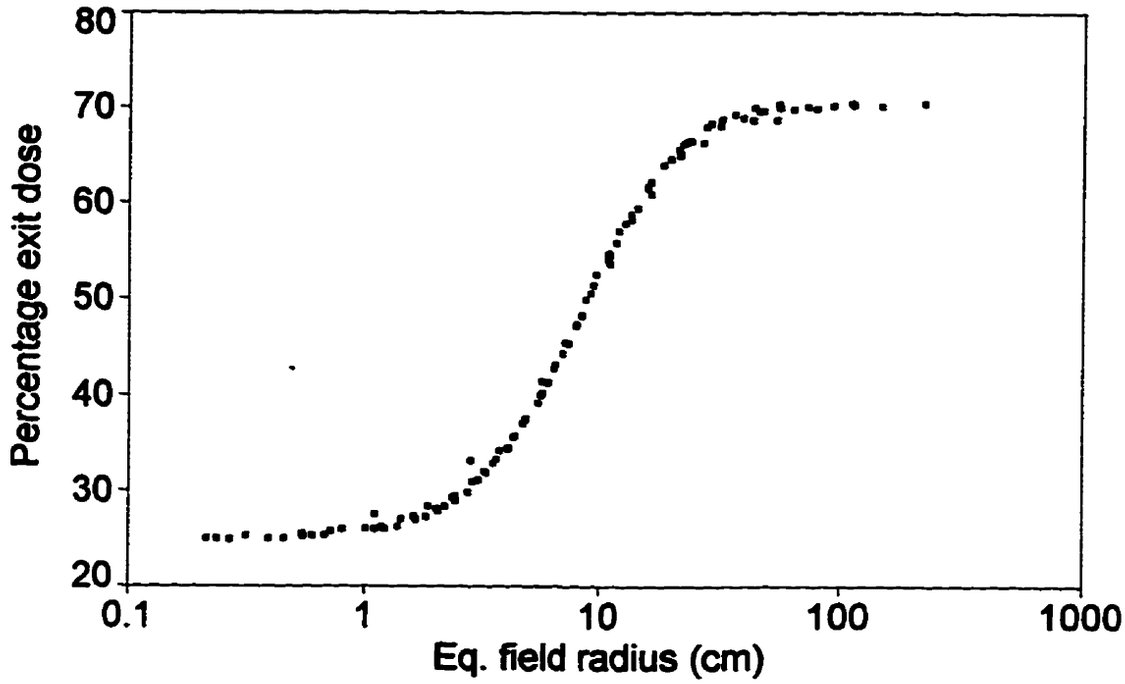

Figure 5-5. The percentage exit dose as a function of equivalent field radius for a 20 cm thick phantom and 1.25-MeV beams. This figure is the end result of applying the equivalent field size expression, eqn. (5-1), to the clinical field sizes of figure 5-2.

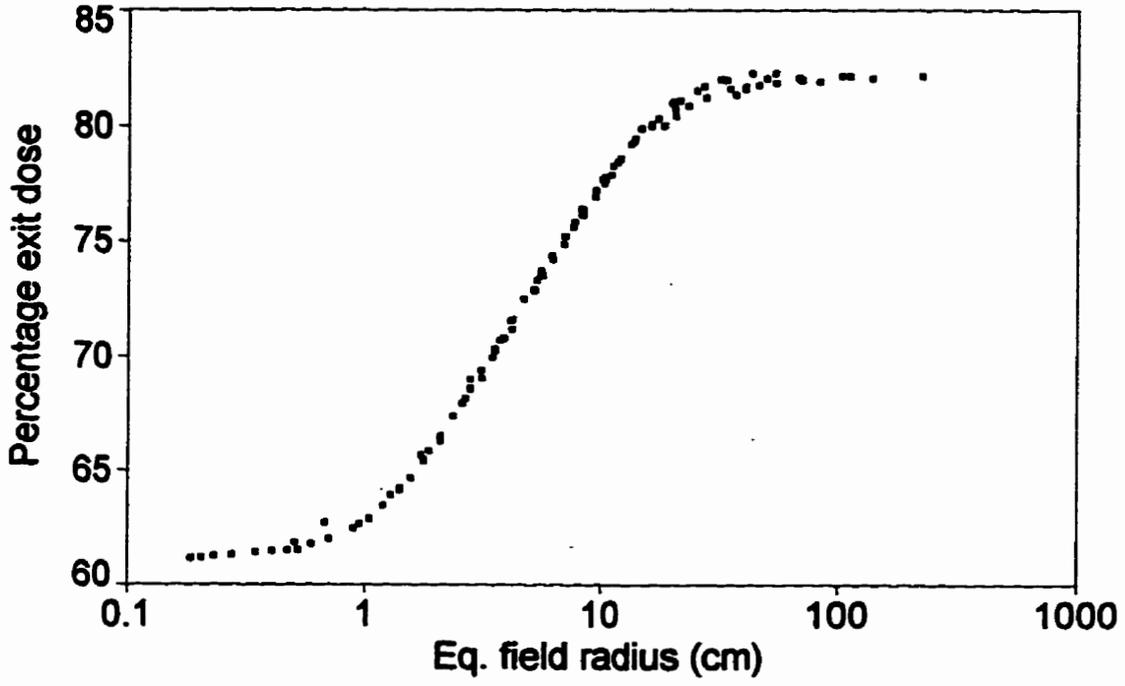

Figure 5-6. The percentage exit dose as a function of equivalent field radius for a 20 cm thick phantom and 5-MeV beams. This figure is the end result of applying the equivalent field size expression, eqn. (5-1), to the clinical field sizes of figure 5-3.

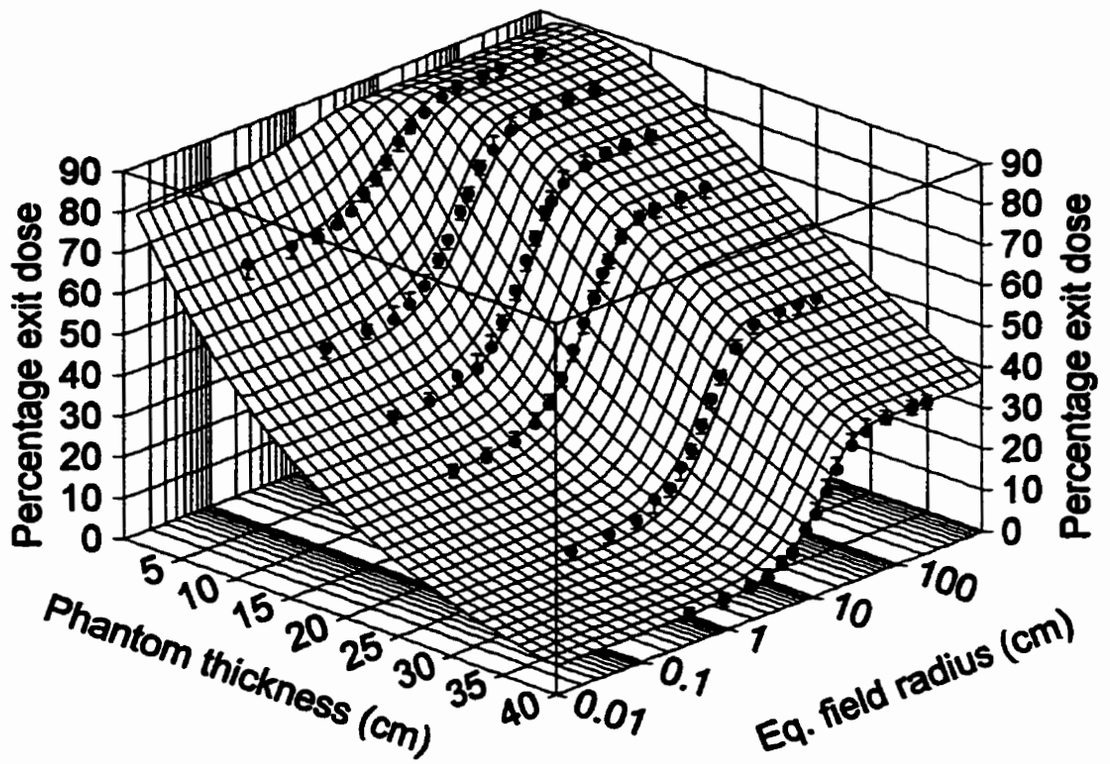

Figure 5-7. The percentage exit dose as a function of equivalent field radius and phantom thickness for 1.25-MeV beams. The data, for a given phantom thickness, is the collapsed data that results from the application of the equivalent field size expression, eqn. (5-1), to the clinical field sizes corresponding to PED surface (such as in figure 5-2) for the phantom thickness in question.

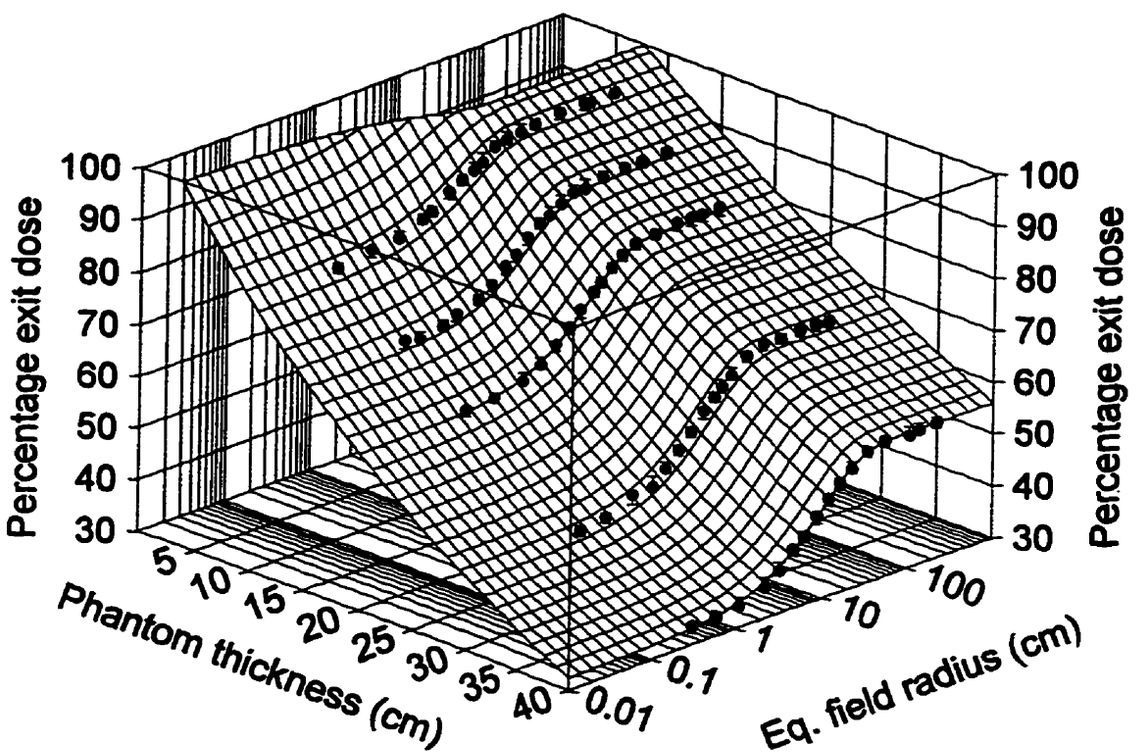

Figure 5-8. The percentage exit dose as a function of equivalent field radius and phantom thickness for 5-MeV beams. The data, for a given phantom thickness, is the collapsed data that results from the application of the equivalent field size expression, eqn. (5-1), to the clinical field sizes corresponding to PED surface (such as in figure 5-3) for the phantom thickness in question.

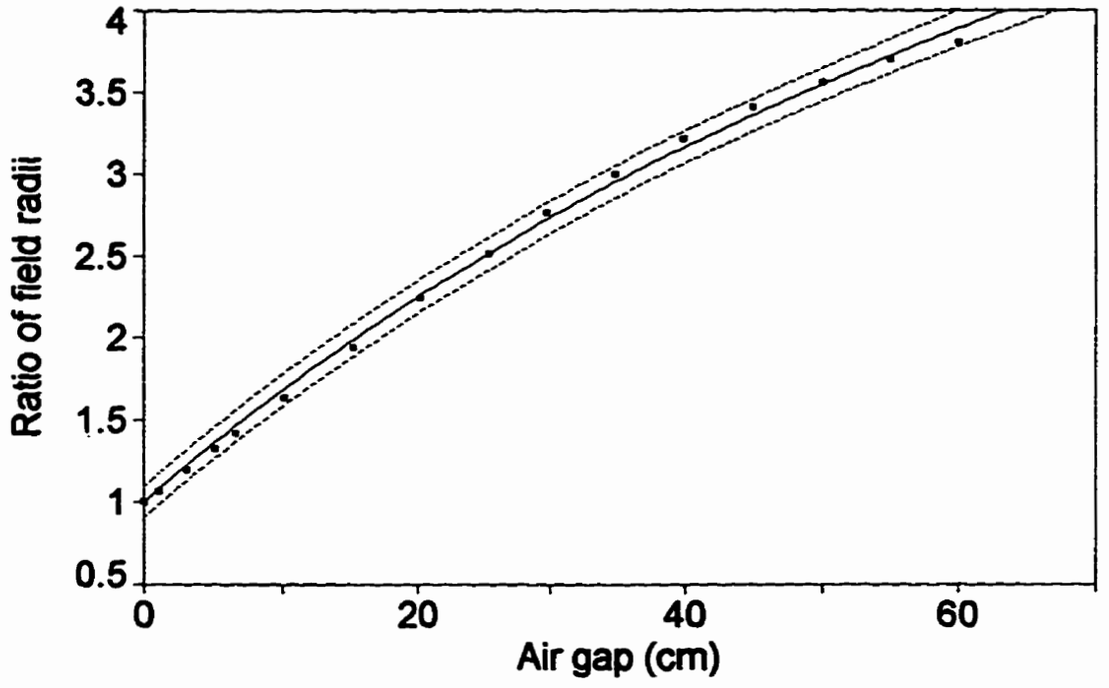

Figure 5-9. The ratio of the clinical field radius to the equivalent field radius, r/r_{eq}, as a function of air gap for r = 13.8 cm (corresponding to 25 x 25 cm^2 square field). This is derived from experimental measurements on a 20 cm thick phantom using a Cobalt-60 teletherapy unit. The points represent the measured data, the solid curve is the least squares fit of eqn. (5-1) to the data, while the dotted lines indicate the 95% prediction limits.

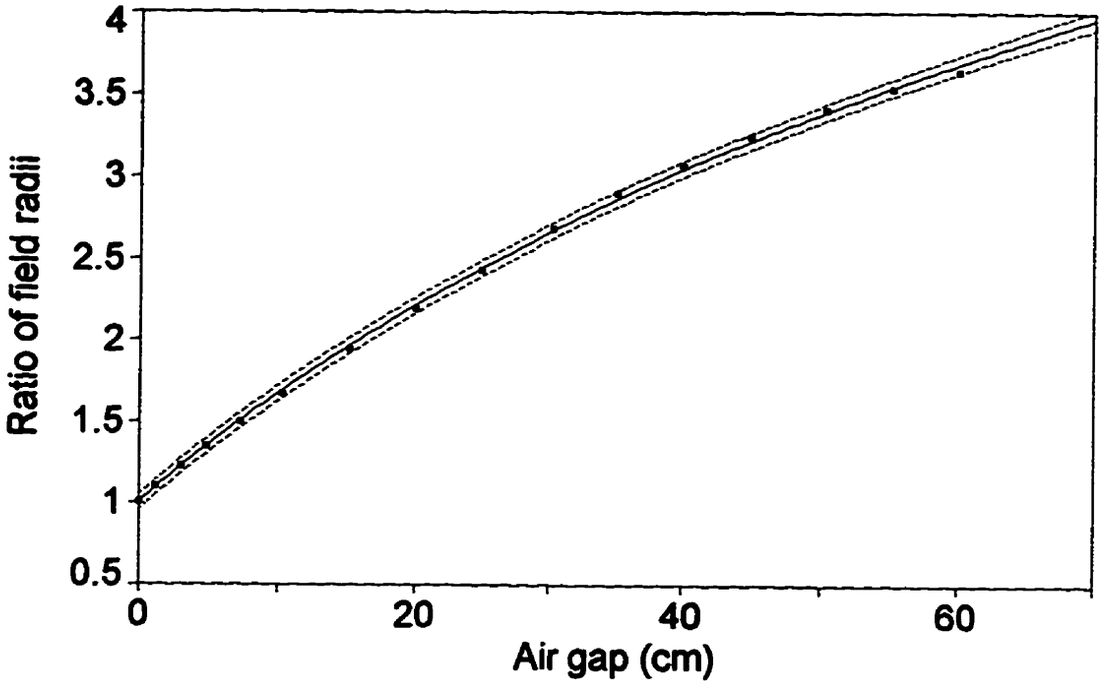

Figure 5-10. The ratio of the clinical field radius to the equivalent field radius, r/r_{eq}, as a function of air gap for r = 19.2 cm (corresponding to 35 x 35 cm^2 square field). This is derived from experimental measurements on a 20 cm thick phantom using a Cobalt-60 teletherapy unit. The points represent the measured data, the solid curve is the least squares fit of eqn. (5-1) to the data, while the dotted lines indicate the 95% prediction limits.

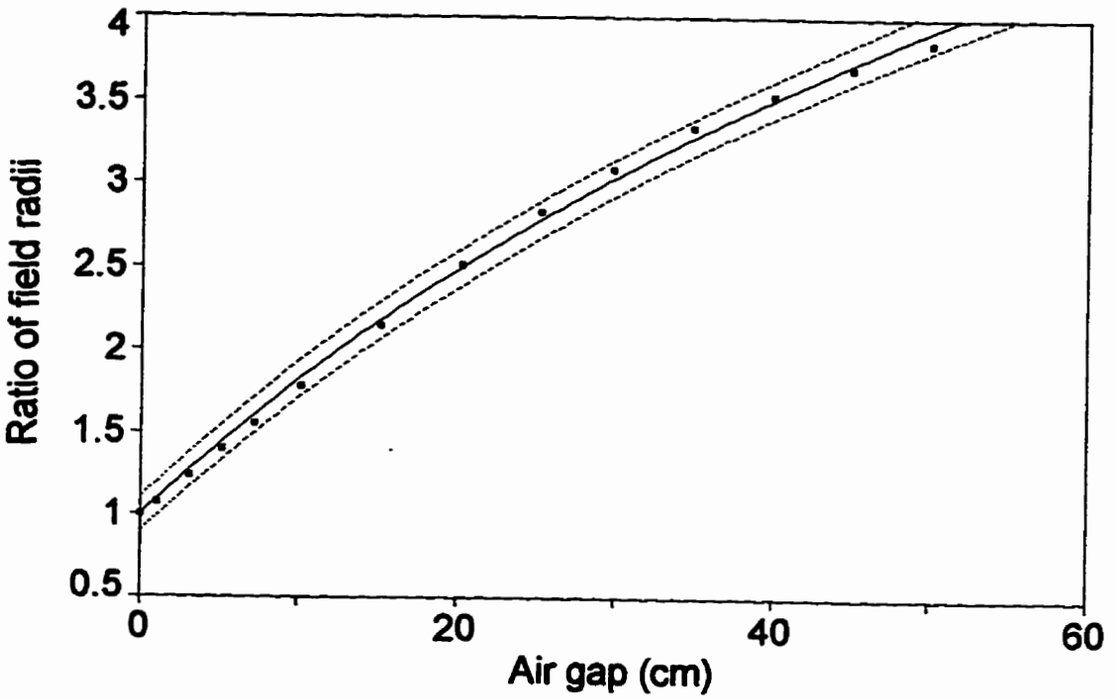

Figure 5-11. The ratio of the clinical field radius to the equivalent field radius, r/r_{eq}, as a function of air gap for r = 13.8 cm (corresponding to 25 x 25 cm^2 square field). The data shown are for a 5.5 cm thick phantom.

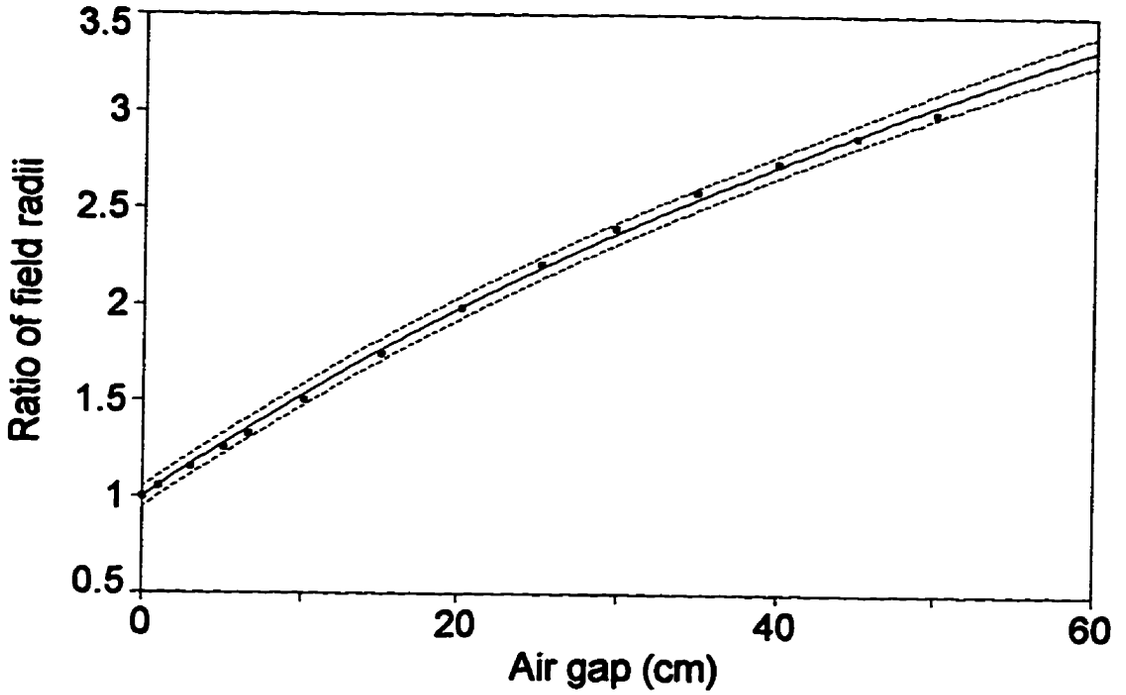

Figure 5-12. The ratio of the clinical field radius to the equivalent field radius, r/r_{eq}, as a function of air gap for r = 13.8 cm (corresponding to 25 x 25 cm^2 square field). The data shown are for a 32.6 cm thick phantom.

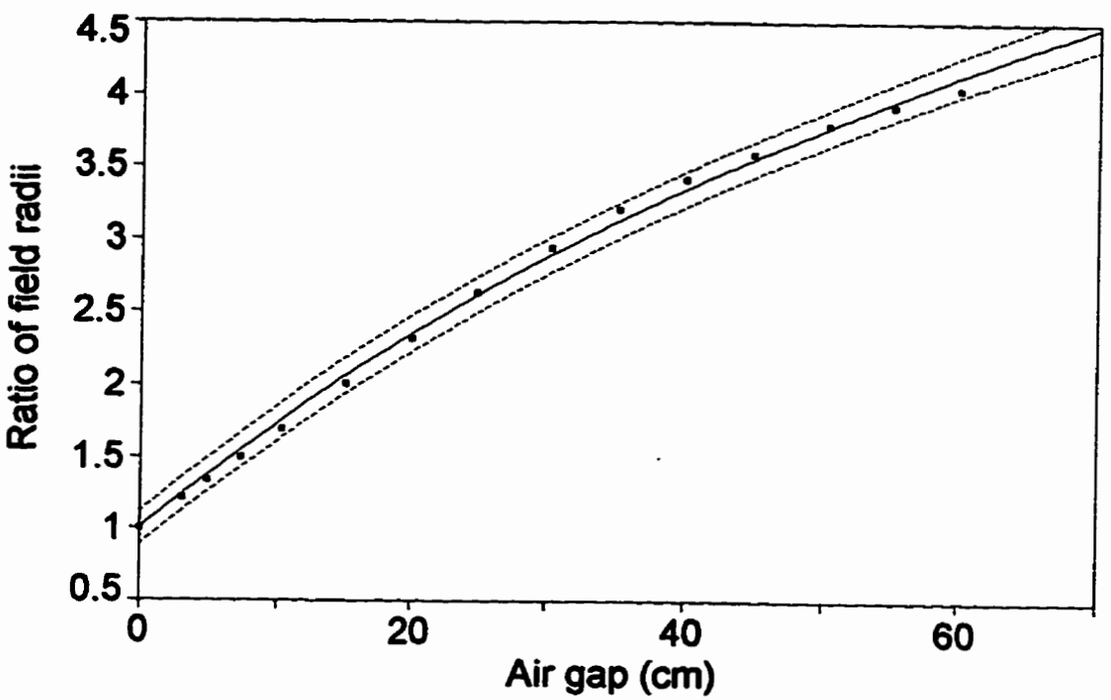

Figure 5-13. The ratio of the clinical field radius to the equivalent field radius, r/r_{eq}, as a function of air gap for r = 13.8 cm (corresponding to 25 x 25 cm^2 square field). These data were obtained with an "ion chamber-in-air" detector for a 20-cm thick phantom.

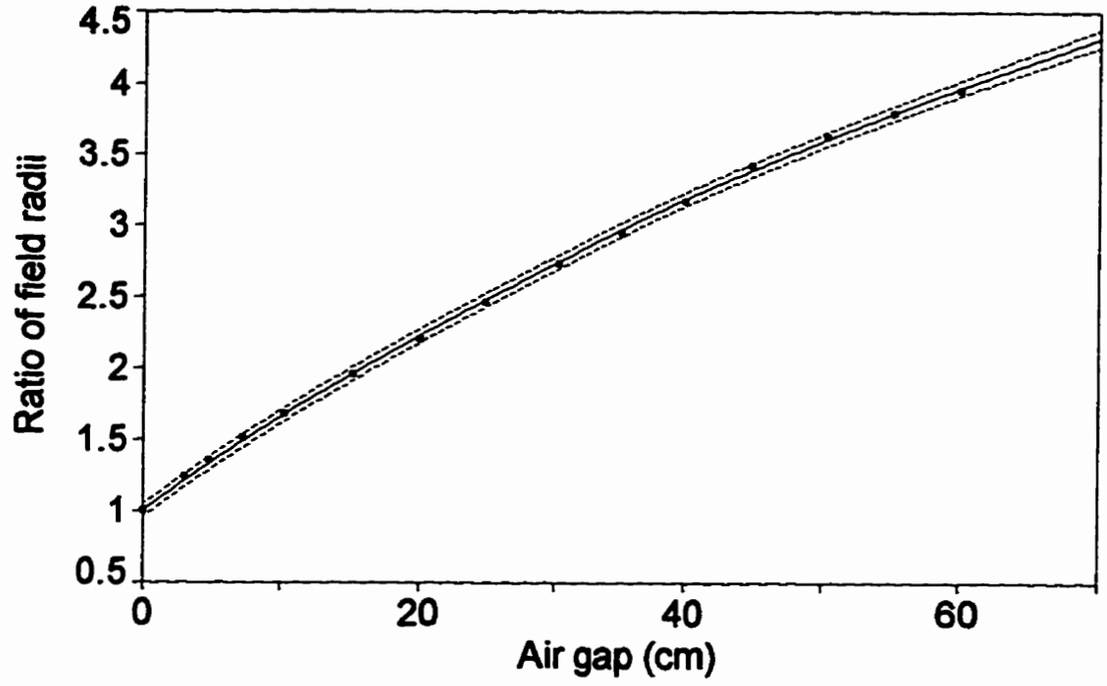

Figure 5-14. The ratio of the clinical field radius to the equivalent field radius, r/r_{eq}, as a function of air gap for r = 19.2 cm (corresponding to 35 x 35 cm^2 square field). These data were obtained with an "ion chamber-in-air" detector for a 20-cm thick phantom.

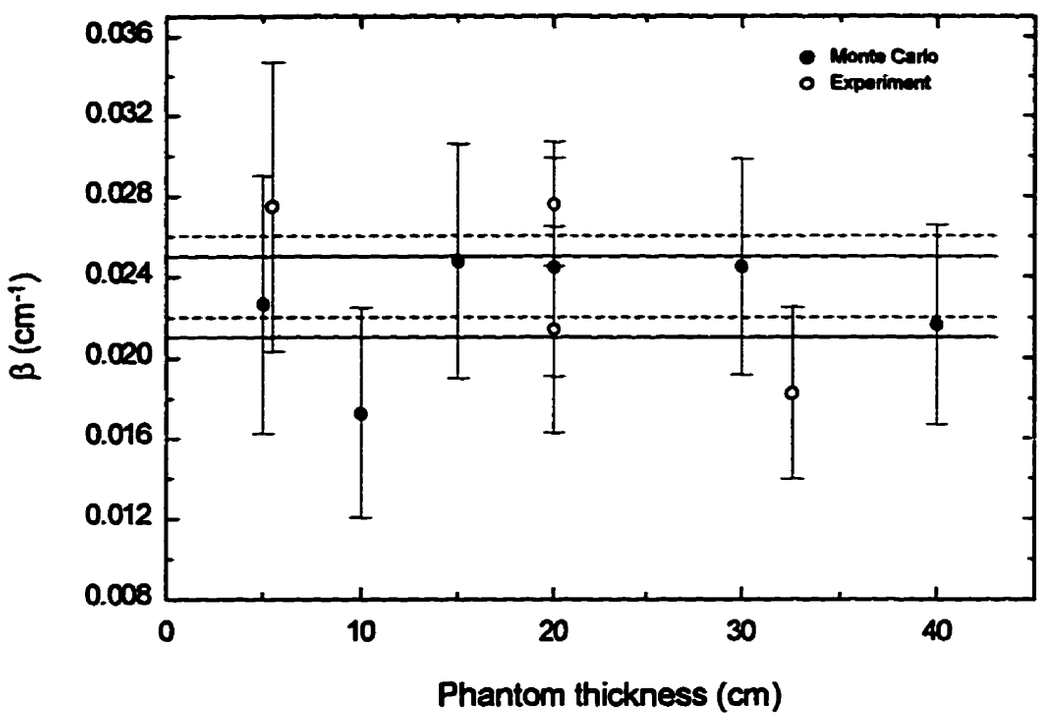

Figure 5-15. The dependence of β on phantom thickness. The values observed experimentally (open circles and dashed lines) are compared to those derived from Monte Carlo modeling (solid circles and solid lines), for 1.25-MeV beams. Each pair of lines represent the 95% confidence interval of the final value of β observed in that specific case.

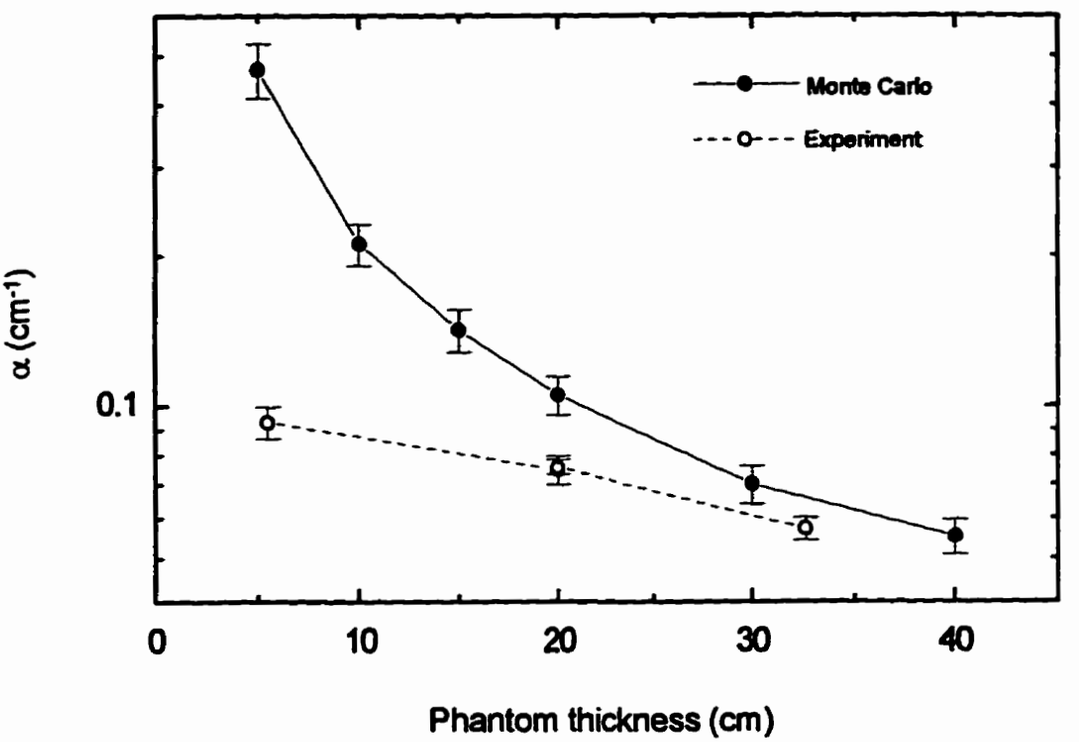

Figure 5-16. The dependence of α on phantom thickness. The values observed experimentally (open circles and dashed line) with an ion chamber-in-slab detector are compared to those derived from Monte Carlo modeling (solid circles and solid line) using a Copper/Phosphor detector for 1.25-MeV beams.

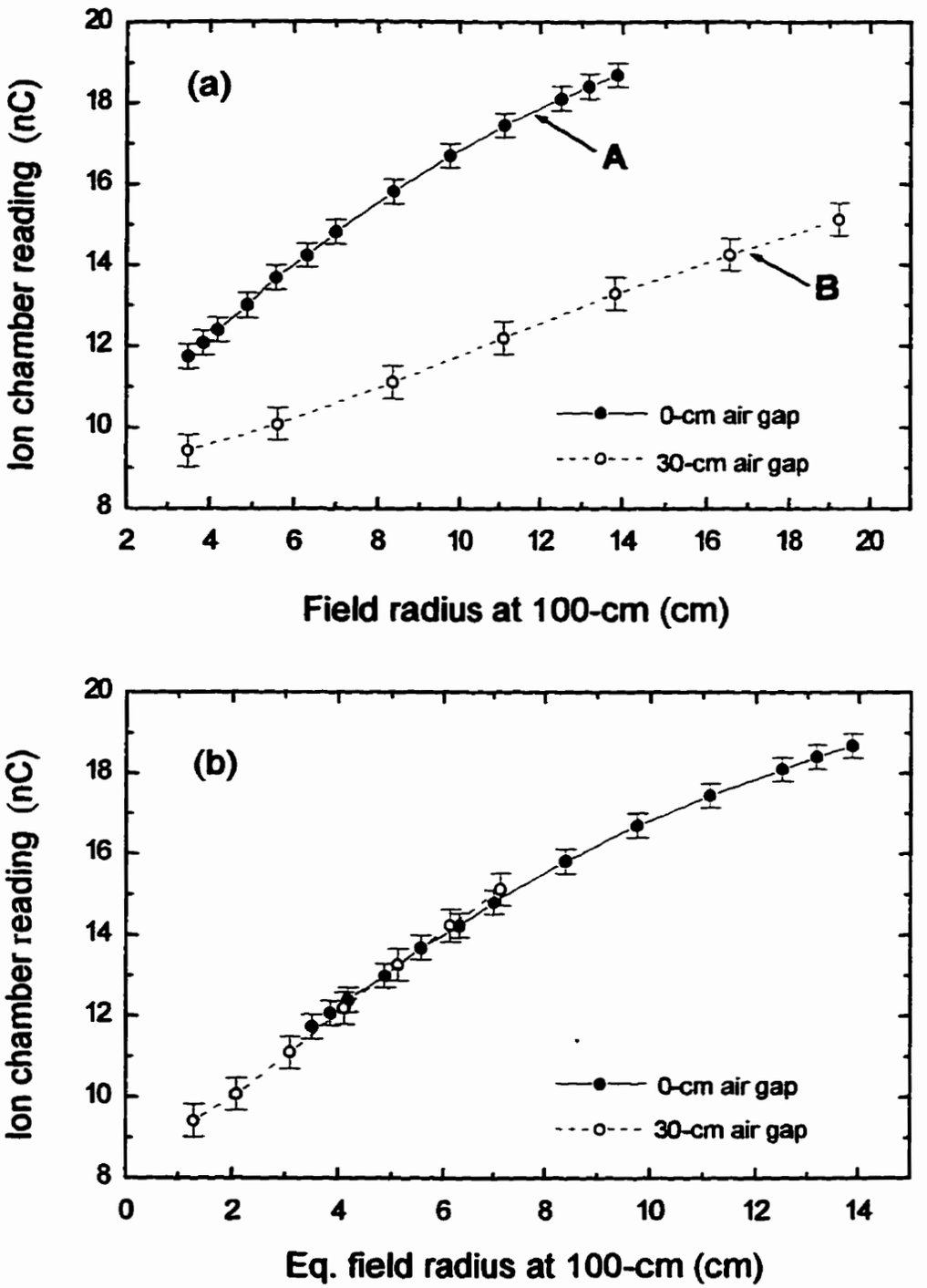

Figure 5-17. The dependence of ion chamber reading (or equivalently exit dose) on (a) actual/clinical field radius and (b) equivalent field radius for a 20 cm thick phantom. After scaling the actual field radii in the top figure with eqn. (5-1), the bottom figure results.

Chapter 6

Summary

6.1 Discussion

The goal of radiotherapy is to deliver a tumourcidal dose of radiation to the tumour while ensuring that the dose and volume irradiated of surrounding normal tissues is as low as possible. The characteristics of dose-response curves for tumour control and normal tissue complication observed clinically have led to the recommendation that the tolerance level on accuracy in dose delivery be 3% relative standard deviation in the delivered target dose. However, the action level, at which it is recommended to work seriously to improve the accuracy in dose delivery, is 5% relative standard deviation. It is unclear whether or not this level of accuracy is achieved or even achievable in normal clinical practice since numerous reports have shown that each and every step in the treatment process is often subject to these orders of uncertainty. In order to ensure that the precisely planned treatment is delivered to the patient, treatment verification needs to be carried out to detect, quantify, and correct these errors at the beginning and during the course of treatment.

The conventional method for verifying patient setup errors is geometric verification, during which a transmission image of the patient is acquired prior to or during treatment using portal films or electronic portal imaging techniques, and is compared with images

taken during treatment simulation. As the use of electronic portal imaging devices (EPIDs) increases, the emphasis is shifting to quantitative dosimetric verification or portal exit dosimetry. In this approach, a portal dose image measured with an EPID during treatment is compared with that calculated during treatment planning. The success of this approach will ultimately depend on a proper understanding of the factors that influence the measurement and calculation of dose distributions in the detector plane. The main objective of this work was to identify and analyze such factors using Monte Carlo methods.

To understand the influence of the patient/detector geometry on the spectral distribution of photon beams reaching the detector plane, the spectral characteristics of exit photon beams were studied. It was found that the intensity, energy spectrum, mean and effective energies of the beams are significantly affected by variations in the patient/detector geometry. These translated into changes in the exit dose/PED to a metal-phosphor detector. Comparison of the spectra at the copper surface entrance to those at the copper-phosphor interface of the detector, and also of the relative response of various detector materials showed that the spectral distribution and exit dose are affected by the detector design. The phosphor-based detectors exhibited a high response compared to the water-based detectors in those situations where the intensity of the scattered photons reaching the detector was large (e.g. large field size and small air gap). In cases of limited scatter at the detector (e.g. small field sizes and/or large air gaps), the relative response of water was found to be slightly higher than that of phosphor. These show that the exit dose is significantly affected by the atomic composition or atomic number of the materials used in

a particular detector. This effect needs to be considered in order to be able to accurately calculate the dose deposited in the high atomic number metal-phosphor detector. It is proposed that the existing dose calculation algorithms, which do not account for dose perturbations due to changes in atomic numbers, be improved if they are to be used to accurately predict the exit dose measured by a metal phosphor detector.

Furthermore, analysis of the spectral characteristics and exit dose revealed that the effects of an increasing air gap and an increasing field size, and vice versa, are roughly complementary. This suggests the use of "equivalent field sizes" to account for intensity and spectral changes arising from air gap variations. The feasibility of using an equivalent field size technique for modeling the air gap was therefore investigated. A patient/detector geometry involving an air gap was referred to as the clinical geometry, whereas the corresponding geometry with the same SSD, same phantom thickness but for which the detector is in contact with the phantom was designated the reference geometry. A field size in a reference geometry was said to be equivalent to a field size in the corresponding clinical geometry if both of these field sizes resulted in the same exit dose. Based on Monte Carlo modeling, a numerical expression (eqn. (5-1)) for computing the equivalent field size has been proposed. The equivalent field size concept and the proposed expression for computing the equivalent field size has been confirmed experimentally. In this expression (eqn. (5-1)), β was observed to be a constant, independent of phantom thickness, detector response, and incident beam quality, and its values determined experimentally (0.024 ± 0.002 cm^{-1}) and by Monte Carlo modeling (0.023 ± 0.002 cm^{-1}) agree well within the limits of experimental and statistical uncertainties. In contrast, α was

observed to depend on all the afore-mentioned variables. For a copper/phosphor detector, α is inversely proportional to phantom thickness d for the energies studied (see eqn. (5-4)), where the constant of proportionality is given by $\alpha_0 = 2.15 \pm 0.04$ and $\alpha_0 = 2.58 \pm 0.10$ for 1.25 and 5 MeV monoenergetic incident beams, respectively. The α values determined by Monte Carlo modeling were higher than the corresponding experimental values since the copper/phosphor detector used for the Monte Carlo simulations has a higher relative response to scattered photons than the ion chamber employed in the experiments. The equivalent field size technique developed in the current study is proposed as an approach for modeling the air gap. An advantage of this technique is that it can be incorporated with minimal modifications in the existing dose calculation algorithms.

6.2 Future work required

In the current study, the Monte Carlo simulations modeled a copper-phosphor portal imaging detector, which consisted of a specific thickness of GD_2O_2S phosphor (500 mg/cm^2) on a copper plate of a specific thickness (2.25 mm). Although the equivalent field size concept introduced in this work will apply to any detector, the various parameters (namely α and β) in the equivalent field size model are detector dependent. Therefore, it may be useful to extend the investigation to include other detectors. For instance, Monte Carlo data for a water equivalent detector could be generated and compared directly to experimental measurements made in water or water-equivalent medium. This will serve as a more rigorous test of the equivalent field size model. The

next phase will be to extend the investigation to other incident energies and/or use clinically realistic incident spectra. Following this, the slab geometry will have to be replaced with a non-slab geometry that more closely approximates that found under normal clinical conditions. At each stage of the investigations the equivalent field size model may have to be modified or improved, if necessary. Finally, the equivalent field size concept will be extended to off-axis points.

To compare portal dose images measured by a metal-phosphor portal imaging detector during patient irradiation to those calculated during treatment planning, it will be necessary to develop a model that can be used to account for dose perturbations due to changes in atomic composition.